Fall 2023

Assessment of Atmospheric Correction Algorithms for the Remote Sensing of Water Quality in Southeastern U.S. Estuaries

Jerome Reimers

ASSESSMENT OF ATMOSPHERIC CORRECTION ALGORITHMS FOR THE REMOTE SENSING OF WATER QUALITY IN SOUTHEASTERN U.S. ESTUARIES

by

JEROME REIMERS

(Under the Direction of Christine Hladik)

ABSTRACT

Water quality is a key indicator in understanding and representing an environment's overall health. Through developments in remote sensing, we can utilize satellite imagery to measure water parameters in each aquatic system. When accurate atmospheric correction is performed, remote sensing can account for atmospheric attenuation and scattering effects to better measure the reflectance and estimate optically active constituents (OAC) present in upper water columns. Atmospheric Correction for OLI lite (ACOLITE) is an atmospheric correction algorithm designed specifically for robust atmospheric correction of water surfaces, in comparison to algorithms designed more for land surfaces such as the European Space Agency's (ESA) Sen2Cor. An evaluation of atmospheric correction methods for coastal water quality for Georgia, USA, where contributions from pigments, inorganic matter, and organic matter are quite variable, has not been performed. This project analyzes the application and accuracy of atmospheric correction methods for several Georgia estuaries with spatially and temporally variable concentrations of water quality constituents using satellite imagery, in situ close-range spectral reflectance remote sensing match-up data, and field and laboratory analysis of water variables. The objectives of this study are: (1) Characterize study sites and individual water samples based on their concentrations of chlorophyll-a pigments, inorganic matter, and color-

dissolved organic matter based on hyperspectral close-range reflectance, multispectral Sentinel-2 MultiSpectral Instrument (MSI) reflectance, and analysis bulk water samples and; (2) Evaluate and compare the accuracy of spectral reflectance data with no atmospheric correction, and ACOLITE and Sen2Cor atmospheric correction algorithms. It was found that hierarchical clustering had inconclusive results at characterizing optical water types, and some variation in optical water types were even seen within study sites. Further, ACOLITE and Sen2Cor atmospheric correction algorithms performed comparably at each specific wavelength in these environments (ACOLITE R^2=0.215 (band 5) to 0.33 (band 2), Sen2cor R^2=0.061 (band 5) to 0.299 (band 3)), and further validation would be required for a deeper understanding of their performance on more than a band-to-band comparison.

INDEX WORDS: Remote Sensing, Atmospheric Correction, Estuary, Water Quality

ASSESSMENT OF ATMOSPHERIC CORRECTION ALGORITHMS FOR THE REMOTE SENSING OF WATER QUALITY IN SOUTHEASTERN U.S. ESTUARIES

by

JEROME REIMERS

B.S., Graceland University, 2020

A Thesis Submitted to the Graduate Faculty of Georgia Southern University in Partial Fulfillment of the Requirements for the Degree

MASTERS OF APPLIED GEOGRAPHY

STATESBORO, GEORGIA

ASSESSMENT OF ATMOSPHERIC CORRECTION ALGORITHMS FOR THE REMOTE SENSING OF WATER QUALITY IN SOUTHEASTERN U.S. ESTUARIES

by

JEROME REIMERS

Major Professor:	Christine Hladik
Committee:	John Schalles
	Munshi Rahman
	Risa Cohen

Electronic Version Approved:
December 2023

ACKNOWLEDGMENTS

The completion of this thesis project and my graduate journey at Georgia Southern University would not have been possible without the advice and support from so many different people. I cannot understate my gratitude for my thesis advisor, Dr. Christine Hladik. Her mentorship, patience, and commitment to helping me has been continuous and unwavering, even when I did not believe in myself, and I would not have completed this project without her. I also would like to thank my thesis committee, Dr. Risa Cohen, Dr. Munshi Rahman, and Dr. John Schalles for their guidance and encouragement. To everyone who helped collect field data, including my fellow Georgia Southern students, Harrison Currin, and Tommy Pudil, your time commitment made collecting the stations that we did possible. I would also like to reiterate my thanks to Dr. John Schalles for his guidance in providing me with the skills and lab materials needed to complete this project. Finally, I would like to thank my wife, Chelsea Reimers for everything that you have done in making sure this project was completed, including helping with field sampling, providing support in the lab, and sharing your skills and knowledge in writing this report.

TABLE OF CONTENTS

LIST OF FIGURES

LIST OF TABLES

CHAPTER 1

INTRODUCTION

1.0 Introduction

Water quality consists of all biological, chemical, and physical characteristics required to meet the needs of various water usages including drinking, irrigation, and recreation (Chawla et al., 2020). Water is considered polluted when impurities are severe enough to restrict the use of and may or may not be the result of human interaction (Lillesand et al., 2015**)**. Access to clean water and sanitation remains the sixth sustainable development goal of the 2030 Agenda for Sustainable Development committed to by the United Nations (Sustainable Development Summit, 2023). With approximately one-third of the global population lacking access to clean drinking water, constant innovation is necessary to manage global waterways that are not only accessible but also clean and sanitary (WHO, 2019). The management strategies used to maintain water constituent sources and fate are crucial. Poor water management practices have direct consequences for our economy and society. Considering the combined effects of global warming and socioeconomic conditions, Koutroulis et al. (2019) suggested that as many as four billion people could be placed under freshwater resource stress with a 4-degree Celsius global temperature increase. This increase would potentially affect the water cycle through an increase in evaporation, intensifying extreme weather events (including flooding, droughts, and cyclones), which place additional strain on water demand and resources (Chawla et al., 2020).

1.1 The Georgia Coastline

The Georgia coastline, where this study was conducted, represents a unique environment compared to its neighboring northern and southern state neighbors. In the 1970s, the Coastal

Marshland Protection Act (CMPA), and the Shore Protection Act, were passed to give policy makers the ability to regulate activities that affect the coastal marshlands of the state in the interest of the public, aimed to balance economic development with conservation by establishing protection zones to restrict construction and vegetation removal (Georgia Rules & Regulations, n.d.). The implementation of this kind of policy was ahead of its time and has resulted in the relatively undeveloped coastline present across the state today in contrast to that of Florida and North and South Carolina. This undeveloped coastline in combination with strong tidal action allows for strong tidal magnitudes to pull out water contaminants and constituents into the ocean, and flush in saline Atlantic Ocean water, less laden with nutrients optimal for algal propagation (Sanford et al., 1992).

The Georgia Department of Natural Resources Coastal Resources Division releases an annual report card for the Georgia Coastline, which provides information on the current health and condition (CRD, 2022). For 2022 the Georgia coastline was given a moderately good score "B" score of 74% based on several indicators including fecal coliform, enterococcus, dissolved oxygen, and various fauna. Notably, dissolved oxygen fell in 2022 from 2021 to 75%. This score is a function of Georgia's ability to maintain its healthy coastal and estuarine systems. NOAA provides data detailing the economy connected to coastal regions of the United States. Most of the economic activity in coastal Georgia fell into the category of Manufacturing, with a GPD total of over $4,500,000,000 in 2020 (NOAA, 2021). Financial activities were the next biggest category, followed by education and health services, and professional and business services. Natural resources and mining only accounted for slightly over $108,800,000 of the $30,162,000,000 GPD total in 2020. Only 620 employees fell into the natural resources category,

while manufacturing accounted for almost 22,200 people. Coastal economic activity because primary industry is limited within the region (NOAA, 2021).

1.2 Water Quality Threats

Eutrophication describes a natural aging process of a body of water that results from the accumulation of dissolved nutrients over time (Chislock et al., 2013). This process is often accelerated unnaturally by nutrient nitrogen and phosphorous loading caused by pollution and sediment accumulation (Lillesand et al., 2015). An imbalance of nutrients through eutrophication often propagates algal growth, and more phytoplankton productivity can produce turbid waters. Over longer time periods nutrient overloading can cause water bodies to become hypereutrophic, where nutrients and minerals such as clay loading becomes extreme (Li & Li., 2004). Additionally, a large biomass of phytoplankton produces an algal bloom, which has the potential to be categorized as a harmful algal bloom (HAB). A HAB causes harm through the production of toxins, or the alteration of food web dynamics through the proliferation of a particularly harmful species of algae (Anderson, 2009). Algal blooms can dominate an aquatic environment's access to sunlight, denying access to all other species below the water's surface (Lillesand et al., 2015; Richardson, 1996). During bloom decay, algal matter sinks and decomposes, consuming dissolved oxygen, and leading to hypoxia and major mortality in other aquatic species (Anderson, 2009). The range and frequency of algal blooms are expected to increase in response to climate change, as temperature largely determines the potential for HABs to form and has already contributed to the growth of specific species (Gobler et al., 2017).

Algal growth is determined by a combination of multiple factors, where even the alteration of food web dynamics through practices such as overfishing can contribute to algal

bloom propagation, and even the nutrient composition of nutrient loading plays a role in determining the algal species that benefit (Heisler et al., 2008). Nutrient loading is exacerbated by climate change, which can boost algal growth (Rodgers, 2021). Along the lines of climate change, the global warming of water surface temperature specifically is recognized as a cause of algal growth (Paerl and Huisman, 2008). Combined, higher amounts of nutrients in warmer water temperatures create conditions for cyanobacteria, or blue-green algae, to thrive (Nazari-Sharabian et al., 2018). He et al. (2017) studied other factors affecting phytoplankton density within the Three Gorges Reservoir in China. Building on existing literature, the authors used principal component analysis (PCA) to demonstrate that ammoniacal nitrogen, nitrate, as well as phosphate, total phosphorus, and total nitrogen all influence phytoplankton density. These compounds are often introduced to water bodies through anthropogenic products and practices such as the use of mineral fertilizers, septic systems, and animal manure runoff. Nitrate specifically acts as a substantial water contaminant and is highly correlated to anthropogenic activities (Widory et al., 2005**)**. He et al. (2017) also observed that light attenuation decreased with an increase in flow, as suspended matter increased in the surface layer of water. This decrease in light attenuation can compensate for depths and limit algal growth. Flow and adsorption also have the potential to reduce the amount of nutrients available for algal growth. Total suspended solids (TSS) or turbidity has also been connected to the transportation of bound nutrients throughout a body of water, which could expand the area in which algal blooms have the right conditions for growth, or simply create a problem elsewhere (Lillesand et al., 2015**)**.

Another major contributing factor to the decline of the health of a body of water is urban development. Urbanization and increases in population density can generate the need for river impoundments along with an increase in anthropogenic practices, like increases in primary

industry land use, which has been researched as the driving force behind wider ecosystem change (Takagi et al., 2017). Wang et al. (2001) found that urban development creating connected impervious surfaces is a significant metric for determining urbanization's effect on water quality, with measurements as low as 12% connected imperviousness demonstrating a strong influence on surrounding water quality through anthropogenic runoff sources. Correlated to development density, increases in nitrogen and phosphorus use and runoff within surrounding watersheds, connect human practices with impacts on surrounding water bodies (Carle et al., 2007).

1.3 Remote Sensing Approach

The remote sensing approach provides a methodology to broadly inform water quality management decisions. Ability to see and respond to space and time patterns can greatly improve assessments of water resource and local, regional, and global scales, with significant advantages to *in situ* and water sampling using traditional station-based-point collections. In some cases, buoyant gas vesicles suspend algae just below the surface making them detectable through remote sensing (Richardson, 1996). Hydrometeorological monitoring through *in situ* methods is challenging due to the outdated and disproportionately distributed existing monitoring network as well as the inability to conduct large-scale spatiotemporal analysis with a time-sensitive approach (Mishra and Coulibaly, 2007, Richardson, 1996). Remote sensing from satellite-based sensors with accurate atmospheric correction provides a quantitative measure of reflected light from the Earth's surface, potentially allowing for cost-effective studies of larger spatial extents and higher temporal resolution of an aquatic ecosystem's water quality (Sagan et al., 2020, Li and Li, 2004). Through the combination of large-spatial scale multi-temporal imagery, an *in situ*

spectroradiometer instrument, and laboratory-analyzed bulk water samples, an interdisciplinary approach can be incorporated to calibrate entire satellite scenes (Caballero et al., 2020).

1.4 Remote Sensing of Water Quality

Broad water quality assessments can be made using remote sensing by measuring the combined effects of Optically Active Constituents (OACs) on water reflectance. These water quality parameters include chlorophyll-*a* (Chl-a) pigment, inorganic matter (seston, total suspended solids (TSS), turbidity), and colored dissolved organic matter (CDOM). Chl-a is an indicator demonstrating the presence of littoral-zone macrophytes, eukaryotic algae, and cyanobacteria. TSS represents all organic and inorganic suspended solids in the entire water column. CDOM comprises decomposing organic plant and bacterial matter and is the largest component of dissolved natural organic matter found in water bodies (Brezonik et al., 2015). These water quality parameters are of particular importance for measuring overall water quality as they are OACs, and estimations of OACs can be derived across large a spatial scale, as total light reflected is a function of the inherent optical properties (IOPs) of these constituents at respective wavelengths of light (Chawla et al., 2020; Gordon, 1978*;* Lillesand, 2015). Knowing which OACs, and their IOPs, are in the water that is tested may allow researchers to make appropriate adjustments to accurately calibrate and validate water constituent algorithms for testing water quality on a larger scale and with greater accuracy.

Optical remote sensing is simply an observation of backscattered light from surface water, features of the water column, and potentially in extremely shallow and clearer waters, benthic substrates. Photons of light can transmit, scatter, or backscatter (change their direction of travel), or absorb, and when light undergoes either scattering or absorption, it is said to have

attenuated or undergone attenuation (Dekker and Peters 1993). Total absorption can be expressed in terms of the sum of absorption from the water itself, the absorption of CDOM (aCDOM), phytoplankton, and TSS. Total backscattering can be expressed by the sum of backscattering from water, phytoplankton, and TSS (Giardino, 2019). This will be discussed in more detail for each of the water constituents involved in section 1.5 Optically Active Constituents.

When calculating the reflectance of a body of water (or any surface), reflectance is proportional to backscattered photons, and absorption is inversely proportional to reflectance. This means that as backscattering increases, so does the upwelling water radiance, and as absorption increases, upwelling water radiance decreases.

Remote sensing reflectance is calculated as a ratio of upwelling water radiance and hemispherical downwelling irradiance,

$$(1)\ r_{rs}(\lambda) = \frac{L_w(\lambda)}{E_d(\lambda)}$$

where $r_{rs}(\lambda)$ is reflectance, $L_w(\lambda)$ is upwelling water radiance, which is measured by a sensor from the water, in response to $E_u(\lambda)$, downwelling irradiance, which is hemispherical downwelling radiance (Giardino, 2019; Lillesand et al., 2015).

For close-range reflectance measurements, taking measurements above- and below-water has been an ongoing debate within the remote sensing community. Both approaches bring with them unique advantages and disadvantages, however Bhatti et al. (2009) settled on measurements being taken just below the water's surface. This conclusion was reached as the above surface reflectance is affected by waves and sun glint, which determined to be too impactful when collecting above-water measurements.

Approaching water quality from the context of remote sensing allows for the estimation of OACs that backscatter light; any uniquely detectable parameter that has an overall effect on water leaving radiance of reflected water. Commonly used OACs included in this project include TSS, Chl-*a*, and CDOM, which in combination dominate overall effects on reflectance curves in Case II waters (Caballero et al., 2020; Brezonik et al., 2015). Evaluating constituents unmeasurable by satellites including total nitrogen and phosphorus, dissolved oxygen, and other microorganisms are only possible through close-range hyperspectral data or other *in situ* methodologies; however, OACs, themselves, can provide major insights into the overall water quality of a given body of water (Anderson, 2009; Brezonik et al., 2015; Palmer et al., 2015; Sagan et al., 2020).

The reflectance of water is very dependent on the presence or absence of OACs, however pure water absorbs weakly in the blue and into green regions of the electromagnetic spectrum (400-550 nm), before, in higher wavelengths in the red and near-infrared, absorption increases very strongly (Dekker and Peters, 1993; Lillesand 2015). It is for this reason water appears blue. Dekker and Peters (1993) attribute bands 1-4 (450-900 nm) of the Thematic Mapper onboard Landsat 4 and Landsat 5 as being the spectral range where light backscatters off water to make determinations about water quality, however, 850 nm is around the region in which absorption increases more rapidly within water.

GLORIA, the GLObal Reflectance community (Lehmann et al., 2023), provides a library of over 7,500 close-range hyperspectral curves at 1 nm intervals between the wavelengths of 350 and 900 nm. At least one water quality measure is also associated with these curves, and this dataset provides the primary database of *in situ* coastal and inland aquatic optical diversity. Included in this database are 17 different approaches to obtaining close-range reflectance,

including the below water reflectance method used in this study, by which a pole suspends the tip of a fiber optics cable connected to a spectrometer below the surface of the water. Thirteen optical water types are defined in this dataset, and data is readily available to expand and compare a close-range reflectance dataset from a study to a larger sample size.

1.5 Water Quality and Ocean Color Satellite Systems

Multiple studies have been conducted utilizing ocean color satellite systems, like Sea-viewing Wide Field-of-view Sensor (SeaWiFS) and MODerate resolution imaging spectrometer (MODIS) (Dall'Olmo et al., 2005), MERIS (Gilerson et al., 2010), and Ocean and Land Color Instrument (OLCI) (Smith et al., 2016), for the retrieval of Chl-*a* and other OACs. These systems are designed with water reflectance characteristics in mind and leverage key regions of electromagnetic reflectance. They also focus on spectral resolution within the visible and near-infrared region of the electromagnetic spectrum, at the sacrifice of spatial resolution, specifically pixel size, as the focus of these systems is a large open-water area. This ultimately allows for a greater signal-to-noise ratio when compared with a typical earth-observation system such as Sentinel-2 or Landsat-8 or 9, which becomes important considering the small signal value emitted from aquatic surfaces (Cabellero et al., 2020).

Frouin et al. (2019), identified current generation ocean color sensors including the MODIS, Visible Infrared Radiometer Suite (VIIRS), OLCI, Geostationary Ocean Color Imager (GOCI), and the Second-Generation GLobal Imager (SGLI), as limited within their spectral resolution for modern water quality analysis. The Ocean Color Instrument (OCI) on board the Plankton, Aerosol, Cloud, ocean Ecosystem (PACE) satellite, which is scheduled to be launched in January of 2024, is the upcoming proposed solution, with 5 nm spectral resolution from 350 to

885 nm and a swath width of 1,500 km (Frouin et al., 2020). This higher spectral resolution comes with trade-offs as later discussed in section 1.7 Challenges of Water Quality Remote Sensing. For example, with a pixel size of 125 meters OCI is designed specifically for ocean water quality remote sensing but becomes challenging to use in estuaries, narrow inland waterways, and coastal and nearshore environments, where the large pixels mix with the reflectance from adjacent terrestrial surfaces. Nearshore remote sensing requires a smaller pixel size, not incorporated in the traditional ocean-color satellite systems (Cabellero et al., 2020; Lang et al., 2022).

A potential alternative product for coastal and inland environments is that of systems like the Vegetation and Environment monitoring on a New MicroSatellite (VENµS), which carries a single sensor, the VENµS SuperSpectral Camera (VSSC) (CNES, 2015). VENµS has a potential 2-day revisit time, with spatial resolution of up to 4-meters per pixel from a 13 km swath width, and 12 spectral bands from central wavelengths of 420 - 910 nm (Herrmann et al., 2010). Although primarily designed for land applications, VENµS also has the temporal resolution, spatial resolution, and spectral bands to complete successful coastal ocean color research, however the use of satellite missions such as these requires much effort for their use to calibrate for atmospheric correction (Dick et al., 2022).

1.6 Optically Active Constituents

Reflectance curves derived from surface water can have a diverse range of shapes and features based on the makeup of optically active constituents (OACs). Figure 1.1a-e contains a few sample reflectance curves inspired from curves collected in Schalles (2006), from different

sites in response to varying quantities of OACs, to demonstrate the variability possible within water quality remote sensing.

1.6.1 Chlorophyll-a (Chl-a)

Phytoplankton, and by proxy its main pigment of Chl-*a, is* optically active and allows for the determination of the presence of algal matter in a water body. Spectrally, Chl-*a* (as well as other accessory pigments) absorbs and scatters light in very specific regions to conduct its function of photosynthesis and reflects other light to avoid damaging photosynthetic cells (Richardson, 1993).

Absorption peaks because of Chl-*a,* carotenoids, and accessory pigments are visible in the blue (440 nm) wavelengths in addition to the red and near-infrared (680 nm) region of the electromagnetic spectrum. Backscattering within the 560 nm region is high, giving Chl-*a* its green color (Chawla et al. 2020; Richardson, 1996; Kutser 2004). In response to absorption peaks from algal pigment and troughs from scattering of light, researchers have devised many different models to quantify Chl-*a* content in μg/L, which can reach values as high as over 100 ug/L in coastal estuary systems, as when concentrations are higher, absorption characteristics intensify (Schalles, 2006; Chawla, 2020; Monobet, 1992). Reflectance algorithms are discussed in more detail in section 1.6 Retrieval Algorithms. Figure 1.1a-e contains a typical reflectance curve in response to extreme chl-*a* concentration, with extreme peaks and troughs caused by chlorophyll pigment absorption and reflection.

While distinct in optical activity, interference with other constituents including CDOM and TSS complicates water leaving reflectance curves across visible wavelengths (Dekker and Peters, 1993). It is also important to note that most light that enters the water is absorbed in the

upper water column, Chl-*a* has little to no effect on a reflectance curve at depths below two meters (Lillesand, 2015; Richardson, 1996).

1.6.2 Total Suspended Sediment (TSS)

TSS is particulate matter that is suspended within the water, including organic and inorganic matter. The dominant effect of TSS on water quality reflectance is limiting light's ability to transmit further into water, resulting in scattering, however in blue wavelengths, TSS absorbs some incoming light which can complicate algorithm development in this region with its combined effect with CDOM (Chawla, 2020; Dekker and Peters, 1993; He et al., 2017). Turbidity is directly linked to TSS, and an increase in turbidity is a result of more suspended particles, meaning turbidity can be used as a measure of TSS (Chawla, 2020; Davies-Colley and Smith, 2001; Wass et al., 1997). TSS present in water bodies also alters nutrient concentrations and reduces dissolved oxygen, having a greater effect on water quality and the overall health of the wider ecosystem (He et al., 2017). Figure 1.1d contains a sample reflectance curve that may be expected in response to higher TSS concentrations.

Caballero et al. (2020) determined that Chl-*a* retrieval algorithms may overestimate Chl-*a* concentrations due to an increase in light being scattered within the red and near-infrared regions of the electromagnetic spectrum in response to TSS or turbid waters, resulting in a stronger Chl-*a* reflectance peak where a trough is usually expected in a typical reflectance curve dominated by Chl-*a*. This peak is also partly the result of a shift in Chl-*a* reflectance peaks in green wavelengths (560 nm) to longer wavelengths closer to the red (591 nm), and an increase in reflectance can be seen in all visible wavelengths, as well as the near-infrared (Schalles, 2001). This area of the electromagnetic spectrum, specifically in the red and near-infrared region, is

used in many Chl-*a* algorithms (Gitelson, 1992; Gitelson et al., 2008; Gurlin et al., 2011; Yacobi et al., 2011), as TSS is an OAC within water, Pahlevan et al. (2017), were able to utilize Sentinel-2 in mapping turbidity across moderately turbid coastal waters. This was achieved by leveraging the red-to-near infrared, single-band algorithm designed by Nechad et al. (2010) that can be applied to any ocean color sensor.

1.6.3 Colored Dissolved Organic Matter (CDOM)

CDOM is the major component of dissolved organic matter within a body of water, specifically comprised of aromatic, carboxylic, fulvic, and humic acids obtained from decomposed plant matter, bacterial growth, algal growth, and sediment loading (Brezonik et al., 2015; Chawla et al., 2020). CDOM loading alters physical, chemical, and biological properties within the water, and attenuates the penetration of light into water, creating an environment suitable to promote algal growth near the surface of a body of water (Osburn and Stedmon, 2011). Brezonik et al., (2005) found that CDOM is strongly correlated to the other OACs, and absorption is strongest at 440 nm, which coincides with a Chl-*a* absorption region (Richardson, 1993). Using remote sensing systems, calculating aCDOM is a challenge, as CDOM absorbs light, but does not cause scattering, and has no specific reflectance peaks or troughs, instead following an exponential decrease in absorption with an increase in wavelength (Brezonik et al., 2015). The relationship between aCDOM and Chl-*a* concentration is a challenge, and the presence of suspended solids also complicates calculating total aCDOM. When calculating aCDOM, Brezonik et al. (2015), found that the natural log of aCDOM at given wavelengths between 450 - 750 nm could be calculated using stepwise regression, by using the natural log of a wavelength's reflectance with reasonable accuracy (r^2=0.856 for simulated Sentinel-2 MSI

bands for *in situ* measurements). Figure 1.1b contains a reflectance curve typical of high CDOM absorption.

The OACs mentioned above when combined create a difficult-to-predict cocktail effect on a resulting reflectance curve, affecting the resulting total reflectance value at each bandwidth. Constituents present in a specific location of a body of water can also disperse depending on water movement through flow or tide in a short amount of time. Palmer (2015) described that OACs do not necessarily co-vary across an entire study site, and ephemeral and quickly changing water conditions disperse constituents if *in situ* data is not collected within a limited time and area relative to the satellite flyover. Many studies with flow or intertidal effects limit *in situ* data collection to a three-hour window before or after satellite flyover as OAC at stations may not remain constant or even comparable to satellite-acquired reflectance data, yielding inaccurate results (Martins et al., 2017; Warren et al., 2019).

1.7 Retrieval Algorithms

Retrieval algorithms are a fundamental approach within remote sensing literature to derive the concentration of an OAC present in a body of water. This is accomplished by creating a model with statistical calibration in an empirical approach or reviewing the interaction of physical light in a semi-analytical model (Sagan et al., 2020). Sagan et al. (2020), in their review of inland retrieval algorithms, discuss how approaches have diversified in formula, range, and use, and many algorithms are still being developed and refined for characterizing OACs today. Spectral methods mentioned include simple band ratios, in which a ratio is created between the reflectance of multiple bands; spectral shape algorithms, where absorption and reflectance properties- including slope or peak differences- of the OAC are isolated and determined by

fitting available bands of a given sensor; empirical estimation, which leverages a regression-based approach between OACs and spectral reflectance (requiring *in situ* measurements to establish); and bio-optical estimation focusing on the radiative transfer equation for OACs from the water leaving radiance, which requires spectral information of AOCs within a region.

Retrieval algorithms estimate concentrations of OACs, by incorporating a mathematical formula of one or more spectral bands. Dekker and Peters (1993) explored the use of multiple band ratios as an approach for monitoring the presence and quantity of Chl-*a* in turbid inland waters, setting a precedence for band ratio use. Detection of Chl-*a* has seen much earlier and wider success in case I waters, where green and blue spectral regions remain clear of absorption from TSS or CDOM, which allows for band ratios within these regions. This spectral blue-green region is optically complex in case II waters, meaning Chl-*a* retrieval algorithms are dependent on the more challenging red-NIR region of the electromagnetic spectrum. (Gons, 1999; Giardino et al., 2019; Gitelson et al., 1993).

Gitelson (1992) made note of the 700 nm reflectance peak in the near-infrared region of the electromagnetic spectrum for inland and coastal waters as a potential site for further exploration, as within water the peak occurring in this region was found to be strongly correlated with Chl-*a*. For case II waters, early work utilizing the 700 nm region of interest for Chl-*a* allowed Gons (1999) to explore the relationship between the 704 nm reflectance peak, and the 672 nm reflectance trough, in a simple semi-analytical method to estimate this OAC. The basis of this and most other algorithms for Chl-*a* is the absorption-reflectance characteristics of phytoplankton at these wavelengths, and this work is novel in evaluating Chl-*a* in optically complex waters.

Mishra and Mishra (2012) provide a brief review of the current literature to categorize spectral indices as an approach to determining Chl-*a* concentrations, classifying empirical modeling into three groups, specifically, two-band empirical, four-band empirical, and three-band semi-analytical models. Further, Mishra and Mishra (2012) developed an index leveraging the 655 to 708 nm regions referred to as normalized difference chlorophyll index (NDCI), an approach with some success in turbid waters where *in situ* data may be unavailable (R^2=0.95 in Chl-*a* ranges between 1-60 mg m^{-3}). Other work around this time also identified a return to this region of interest in Chl-*a* estimation (Gurlin et al., 2011).

TSS and CDOM algorithms have also been proposed, including a linear regression TSS model for Landsat-7 using band 4 in the red region of the electromagnetic spectrum (Hicks et al., 2013), a non-linear regression approach for Landsat missions also using red-centered bands (Lobo et al., 2015), and multiple hyperspectral predictive models for CDOM based on *in situ* data those described in including Brezonik et al. (2005), Brezonik et al. (2015), Kutser et al. (2005), all of which focus on the relationship between multiple bands. While only using one variable, Brezonik (2015) utilized a hierarchical cluster to achieve this, separating their study sites from high to low CDOM absorption.

1.8 Challenges of Water Quality Remote Sensing

Remote sensing offers multiple benefits in water quality-based monitoring and studies including the ability to conduct large-scale spatiotemporal analysis with a more time-sensitive approach. Beyond the contrasting and overlapping effects of OAC in which one constituent may mask or enhance the presence of another (Giardino et al., 2019), additional challenges are presented within remote sensing-based approaches and will be discussed in this section. These

challenges include limited infrastructure, and limitations of satellites and sensors themselves, sun glint, and adjacency effects.

The immediate concern within the inland and coastal aquatic remote sensing community is the limitations presented by sensor design. Remote Sensing sensor design is challenging, as trade-offs are often made between spatial, spectral, radiometric, and temporal resolution when designing a sensor (Lillesand, et al., 2015**).** A sensor typically cannot simultaneously possess a good spatial resolution (small pixel size and large swath width, which translates to the area covered), while also having good spectral resolution (small bandwidths, giving more information from the object detected) (Lillesand et al., 2015). As inland and coastal remote sensing requires fidelity in a smaller pixel size, spectral information is limited in typical multispectral instruments (Cabellero et al., 2020; Palmer et al., 2015)

Mouw et al. (2015) assessed that modern radiometers are created with the purpose of measuring global ocean or land surfaces, which makes it challenging to explore coastal and inland aquatic environments with this technology. Giardino (2019) noted the low signal-to-noise ratio of Landsat 8's Operational Land Imager, and Sentinel 2's MultiSpectral Instrument (MSI) - often used in these case II environments - in contrast to offshore remote sensing systems. The low reflectance of water surfaces requires a greater signal-to-noise ratio for accurate quantification of water reflectance. Water reflectance values are minimal, typically less than 2% reflectance across all wavelengths in clear water, and 0% reflectance beyond 900 nm. When comparing this to terrestrial-based pixels, reflectance is typically much greater at all wavelengths of interest. In the case of bare soil, 2% reflectance is only present around 400 to around 430 nm wavelengths, and all other wavelengths greater than that average greater than 15% reflectance (Lillesand et al., 2015). This trend of higher reflectance at other wavelengths is also present

when evaluating urban environments, vegetation, sand, snow, and clouds (Lillesand et al., 2015). Further, ocean color instruments typically used for Chl-*a* content retrieval become difficult to use nearshore, due to the need for high spatial resolution within inland and coastal waters so as to not combine water-based pixels with the shoreline (Kuhn et al., 2019). Pahlevan et al. (2017) outline the importance of aggregating Sentinel-2 MSI pixels from 10 m to 20 meters to increase the signal-to-noise ratio. This is possible as visible bands 2 (497 nm), 3 (560 nm), and 4 (664 nm) on the MSI have a spatial resolution of 10 meters, and near-infrared bands 5 (704 nm), and 6 (760 nm) (Table 1.1) already have a spatial resolution of 20 meters, meaning the resulting size of produced pixels can be uniform at a 20-meter pixel size. Further, improvements in sensor design hold potential for new insights in inland and coastal remote sensing, particularly through increasing the signal of sensors when compared to the noise detected at each bandwidth.

In contrast, the Landsat Thematic Mapper (TM) sensor onboard Landsat 4 (USGS, 2023) and 5 (USGS, 2023b), along with the Enhanced Thematic Mapper Plus (EMT+) onboard Landsat 7 (USGS, 2023c) offer seven bands (and a panchromatic band on the EMT+) for remote sensing analysis at 30-meter spatial resolution (the thermal band which is not relevant to OAC related water quality studies is 120 meters in the Thematic mapper, and 60 meters in the Enhanced Thematic Mapper). These sensors are whiskbroom systems, which results in a lower signal-to-noise ratio, and data is prone to stripping without perfect calibration.

Landsats 8 (USGS, 2023d) and 9 (USGS, 2023e) utilize the Operational Land Imager (OLI/OLI2) sensors, which have 9 spectral bands, including a blue (band 2), green (band 3), red (band 4), and one singular near-infrared band (band 5) useful in water remote sensing. Pahlevan et al. (2017b) found these OLI bands have a signal-to-ratio ranging from 45 to 321, which when

compared to Sentinel-2 MSI visible bands (bands 2, 3, and 4) meaning that OLI performs two to three times better than Sentinel-2 MSI. With that being said, Pahlevah et al. (2017b) found Sentinel-2 MSI performs 40% better in terms of signal-to-noise in the aerosol band (band 1 of both systems) and ultimately determined both systems are comparable in their signal-to-noise ratio, as this ratio is proportional to pixel size, and Sentinel-2 has smaller, 10 m, visible bands (bands 2, 3, and 4) (Table 1.1).

When comparing OLI to the EMT+, there are improvements in the signal-to-noise ratio, as OLI to a push broom system, which increases the signal-to-noise ratio. Additionally, a band (band 1) for cirrus cloud detection, and another for detecting aerosols were added in the short-wave infrared, and the narrow blue regions of the electromagnetic spectrum respectively.

The major advantage of Landsat mission satellites over Sentinel-2 is that of continuity. Landsat 1 was first launched in 1972 and has been collecting data since. In addition to Sentinel-2 A and B satellites having a higher revisit time than the eight days provided by Landsat 8 and 9 used in tandem, Sentinel-2 provides greater spatial resolution than the 30 meters provided by OLI, and the additional bands including 5 (704 nm) and 6 (740 nm) on board MSI sensors allow for greater water quality analysis (Table 1.1).

One further challenge to water remote sensing is an external factor: sun glint. Depending on the study site's longitude and time of scan, sun glint may corrupt specific pixels or regions within a scene, rendering them unusable. Sun glint damaged pixels can be masked out of the scene; however, this results in a loss of pixels with spectral information (Caballero., 2020; Drusch, 2012; Pahlevan 2017). Sun glint may provide additional issues using the MSI sensor on

board Sentinel-2 satellites, as the equatorial crossing time is 30 minutes later than that of the OLI sensor onboard Landsat 8 (Drusch, 2012).

Due to limitations in the satellite sensor designs, infrastructure, and mechanisms coupled with high upfront costs and limited funding of satellite missions, there becomes a dependency on *in situ* data. This means that resources need to be dedicated to monitoring in the field with both substantial frequency and range (Caballero et al., 2020; Palmer, 2015, Sagan et al., 2020). This dependency comes at an additional cost, particularly when algal bloom identification is of interest to determine if there is a potentially harmful algal bloom, as bloom species identification cannot be conducted through satellite remote sensing, particularly considering other limitations mentioned (Caballero et al., 2020).

1.9 Atmospheric Correction

From space, determining water reflectance becomes a challenge, as in a cloudy sky, scattering caused by cloud droplets makes seeing the surface potentially impossible. Even in clear sky conditions, gaseous absorption, molecular scattering and absorption, and water surface reflection make removing their effects a necessity in a process called atmospheric correction (Frouin, 2019, Gao et al., 2009) Atmospheric correction is the most important step in the remote sensing process to accurately measure water quality and quantify parameters. In most conditions, 90% of the light reaching a satellite over water is derived from the atmosphere (IOCCG, 2010). As a result, when measuring reflectance from space, the largest source of potential residual error is from atmospheric correction (Mouw et al., 2015). To quantify the biogeochemical properties of water from surface reflectance, atmospheric correction must remove attenuation from active atmospheric constituents including water vapor, ozone, oxygen, and carbon dioxide, and is not

easy to achieve perfectly (Gao et al., 2009). These particle effects are particularly noticeable within the lower 400 nm blue wavelengths, where atmospheric is greatest, and therefore also the most important (Brezonik et al., 2015; Giardino., 2019; Kutser et al., 2005; Warren et al., 2019). In the case of Sentinel-2 and other multispectral satellites, ozone cannot be retrieved for every individual pixel, and as such climatological averages in what is called 'lookup tables' are leveraged to calculate whole-scene estimates (L2A products algorithm theoretical basis document).

Landsat has implemented a provisional aquatic reflectance product as a step to contributing to aquatic remote sensing in coastal and inland waters (USGS, 2023f). Aquatic reflectance is calculated to determine the water-leaving radiances for bands 1-5 (visible and near infrared bands), in a similar methodology to that of SeaWiFS. Although promising, the validity of this surface reflectance product is questionable. Maciel et al. (2023), finding high uncertainties that narrowly meet target accuracy, with as much as 110% uncertainty within coastal aerosol and blue bands (band 1 and 2).

Martins et al.'s (2017) study on atmospheric correction in the Amazon floodplain lakes highlights challenges surrounding the remote sensing approach. Many inland and coastal waters are home to a dynamic system, with complex OACs, making it difficult to often apply a one-size-fits-all approach to case II water atmospheric correction. Additionally, seasonal variability also creates challenges for how a given approach plays out within a single aquatic environment. Equatorial locations like the Amazon within Martins et al.'s (2017) study also are susceptible to high cloud cover and cirrus contamination, rendering sections of images unusable as atmospheric correction cannot overcome this interference effectively. Adjacency effects are also present, creating mixed pixels contaminated with reflectance from nearby terrestrial areas.

Frioun et al. (2019), provides a summary of atmospheric correction through history. The standard approach suggested by Gordon (1978), involves estimating surface reflectance around red and near-infrared regions where a body of water is theoretically absorbing all incoming light, before extrapolating this reflectance to shorter wavelengths of interest affected by aerosol effects. This approach has been expanded on over the following decades, and falls into the category of a two-step solution, however, may be difficult to implement into Case 1 waters. Alternatively, a single-step approach calculates the aerosols and water characteristics in the atmosphere at the same time. This is achieved through a model simulating how light would travel under these conditions before applying the model to the measured top-of-atmosphere reflectance recorded by the satellite and can be readily applied to both Case 1 and Case 2 waters. Another route used includes atmospheric correction through a Bayesian analysis approach. A relationship is determined by using the assumed relationship between the top-of-atmosphere reflectance, and the water on the earth's surface. An example of this would be Schroeder et al. (2007), where they used a neural network model with simulated data. The commonality among all these approaches outside of the first is assumptions are made about water reflectance and the atmospheric state outside the non-reflectance near-infrared assumption. These assumptions are not always representative of real-world conditions.

All these approaches rely on radiation transfer codes, which predict how light interacts with the earth through the use of lookup tables consisting of Rayleigh scattering and the effects of aerosol optical properties based on ozone concentration (Frioun et al., 2019). Within this project, image-based approaches are utilized, where atmospheric effects from the image are, before removing them from the top of the atmosphere signal. This is done with a semi-empirical algorithm with integrated look-up tables to remove atmospheric effects (Martins et al., 2017).

The Sentinel toolbox, Sentinel Application Platform (SNAP), provides the Sen2Cor processor for atmospheric correction. As a standard product, many researchers and product users may not even consider their atmospheric correction product, using Sen2Cor by proxy as it is applied by default. All L2A products downloaded from the European Space Agency leverage the atmospheric correction product by default (ESA, 2023). Prior to atmospheric correction, a pre-classification of the scene is needed. Next, aerosol optical thickness at 550 nm is calculated through the dark dense vegetation algorithm (Kaufman and Sendra, 1988), which uses Sentinel-2's band 12 (2,200 nm) to search for dark pixels, so a correlation of band 12 (2,200 nm), band 2 (497 nm) and band 4 (664 nm) can estimate visibility. Water vapor maps are also derived at this step by leveraging the water vapor algorithm, which employs band 8a (865 nm) and band 9 (945 nm) to calculate lookup tables. Sen2Cor uses two ancillary variables within this approach: the atmospheric look-up table from the libRadtran radiative transfer model to help determine atmospheric optical thickness, and the digital elevation model to calibrate a bottom-of atmospheric reflectance. A comprehensive explanation of the Sen2Cor atmospheric correction process can be found in Richer et al. (2012).

Atmospheric Correction for OLI lite (ACOLITE) was developed by the Royal Belgian Institute for Remote Sensing and is primarily leveraged for ocean and inland water studies. The ACOLITE code, built on Python, has been made open access online, and is readily available (Royal Belgian Institute of Natural Sciences, 2023). ACOLITE is completed in two steps: First, Rayleigh correction for scattering caused by air molecules is performed using a lookup table generated from the 6SV model (Vermote et al., 2016). Next, the dark spectrum fitting algorithm computes aerosol depth at 550 nm using multiple targets from within the scene. The dark spectrum fitting algorithm assumes that values in one band of the sensor are near-zero, and

atmospheric conditions have some level of homogeneity. Linear interpolation calculates the aerosol model using what is called a dark spectrum, built by calculating the lowest value recorded from every other band (Valdivieso-Ros et al., 2021). The process is fully described in depth along with the dark spectrum fitting algorithm in Vanhellemont and Ruddick (2018).

Sen2Cor and ACOLITE differ in a few main areas. For one, Sen2Cor is developed exclusively for the Sentinel-2 satellites, while ACOLITE was originally developed for MODIS and SeaWiFS sensors before being adapted for Landsat and Sentinel-2 sensors. Additionally, Unlike Sen2Cor, ACOLITE explicitly attempts to correct some adjacency effects through the incorporation of the dark spectrum fitting algorithm. Adjacency effects occur from water scattering off the surface of the water and being reflected to the water by either land or atmospheric effects (Frouin, 2019; Vanhellemont, 2019). The two methods, however, are similar in their overall methodology.

Studies have also been conducted comparing atmospheric correction products in different aquatic habitats. Mograne et al. (2017), compare Sen2Cor and ACOLITE by a band-to-band comparison with *in situ* close-range reflectance in Amazon floodplains, an area heavily susceptible to adjacency effects. The two algorithms in this study show similar root mean standard error (RMSE) values depending on the reflectance characteristics of the lake of interest, however, this study was performed using the ACOLITE-shortwave infrared (SWIR) approach, which has since been made obsolete by the dark spectrum fitting approach.

Kuhn et al. (2019), compared LaSRC, SeaDAS, and ACOLITE atmospheric correction products in their study in the Amazon, Columbia, and Mississippi Rivers. This study differed however, as algorithm performance was based on the ability to perform accurate Chl-*a*

estimation using the OC3 algorithm, which leverages blue and green bands, and red and near-infrared bands in turbid waters (Sun et al., 2014). ACOLITE outperformed other algorithms tested in Chl-*a* retrieval (Rt=0.7, RMSD=0.13).

Mograne et al. (2019), performed an evaluation of five atmospheric correction algorithms in optically complex waters in France using Sentinel-3. This study again leveraged close-range reflectance and compared atmospherically corrected reflectance from a satellite instrument using statistical analysis. Unlike previous studies mentioned, this study was able to provide a conclusive measurement that provided an overall best-performing atmospheric correction, through a complex scoring method incorporating slope, intercept, bias, RE, RMSE, and R2. No atmospheric correction performance study has been performed on the southeastern coast of the United States.

Although no atmospheric correction studies have been performed on the Georgia coastline, where the current study takes place, in these environments, other *in situ* remote sensing studies have been conducted along the coastline. Bhatti et al. (2009), used the Altamaha River as their study site to compare above-water and subsurface spectral reflectance products to determine the best practice for future studies. Reader and Miller (2013) utilized hyperspectral remote sensing reflectance in the Duplin River to calculate the photochemical rate, which is heavily influenced by CDOM concentration.

Hladik (2004) conducted a remote sensing-based studies of the Georgia Coastline to develop a bio-algorithm model for Chl-*a* retrieval in Apalachicola Bay, Florida; ACE Basin, South Carolina; and Sapelo Island, Georgia, which included the Duplin River (Doboy Sound), the Altamaha River, and the St. Marys River (r=0.72). Using these data, Schalles (2006)

incorporated reflectance from the southeastern coastline in a chapter exploring Chl-*a* estimation in varying CDOM and TSS environments including the Altamaha River, the Duplin River; the Ashepoo River; Apalachicola Bay; and St. Marys River.

1.10 Project Overview

The following section contains an overview of the scope of my thesis project. My objectives are outlined before connecting them to greater significance in reference to the remote sensing community, and water quality assessment.

1.10.1 Objective 1

My first objective is to characterize three study sites and individual stations along the Georgia coast into optical water types based on bulk water sample analysis of Chl-*a*, TSS, and CDOM and close-range remote sensing hyperspectral data. To do this, I collected and processed *in situ* close-range remote sensing data using an Ocean Optics spectroradiometer, along with bulk water samples for all sites in coastal Georgia near the Duplin River, Altamaha River, and St. Marys Rivers.

1.10.2 Objective 2

Next, an analysis of the accuracy of Sen2Cor and ACOLITE atmospheric correction processors compared to *in situ* data was conducted through statistical analysis.

1.10.3 Significance of Project

This project is of particular importance due to the relationship between humans and surrounding case II waters, along with the dependency and effect anthropogenic effects can have on the surrounding environment. A decrease in water quality through eutrophication and nutrient

loading has environmental and economic ramifications. Hoagland et al. (2002) conducted a study to assess the economic effects of harmful algal blooms, estimating around $50 million lost to sectors across the US, including public health, commercial industries, tourism, and recreation, along with monitoring and management. Of notable concern, the rate and range of algal blooms are expected to continue to increase in response to climate change, along with external anthropogenic effects like agricultural land use and urbanization, demonstrating a clear need for management and monitoring practices of water quality (Whitehead et al., 2009; He, et al., 2017). Improvements to atmospheric correction would allow for on-demand accurate monitoring of water quality across the Georgia coastline.

Similar research has been conducted (Martins et al., 2017; Warren et al., 2019), however, limited research has been conducted in connection to atmospheric correction on the Georgia coastline. This coastal area is of particular importance as it is largely undeveloped relative to surrounding areas of the Atlantic coast. This research gives way to advancements in cost-effective water quality management that in a timely manner can help decision-makers and stakeholders understand surrounding environments.

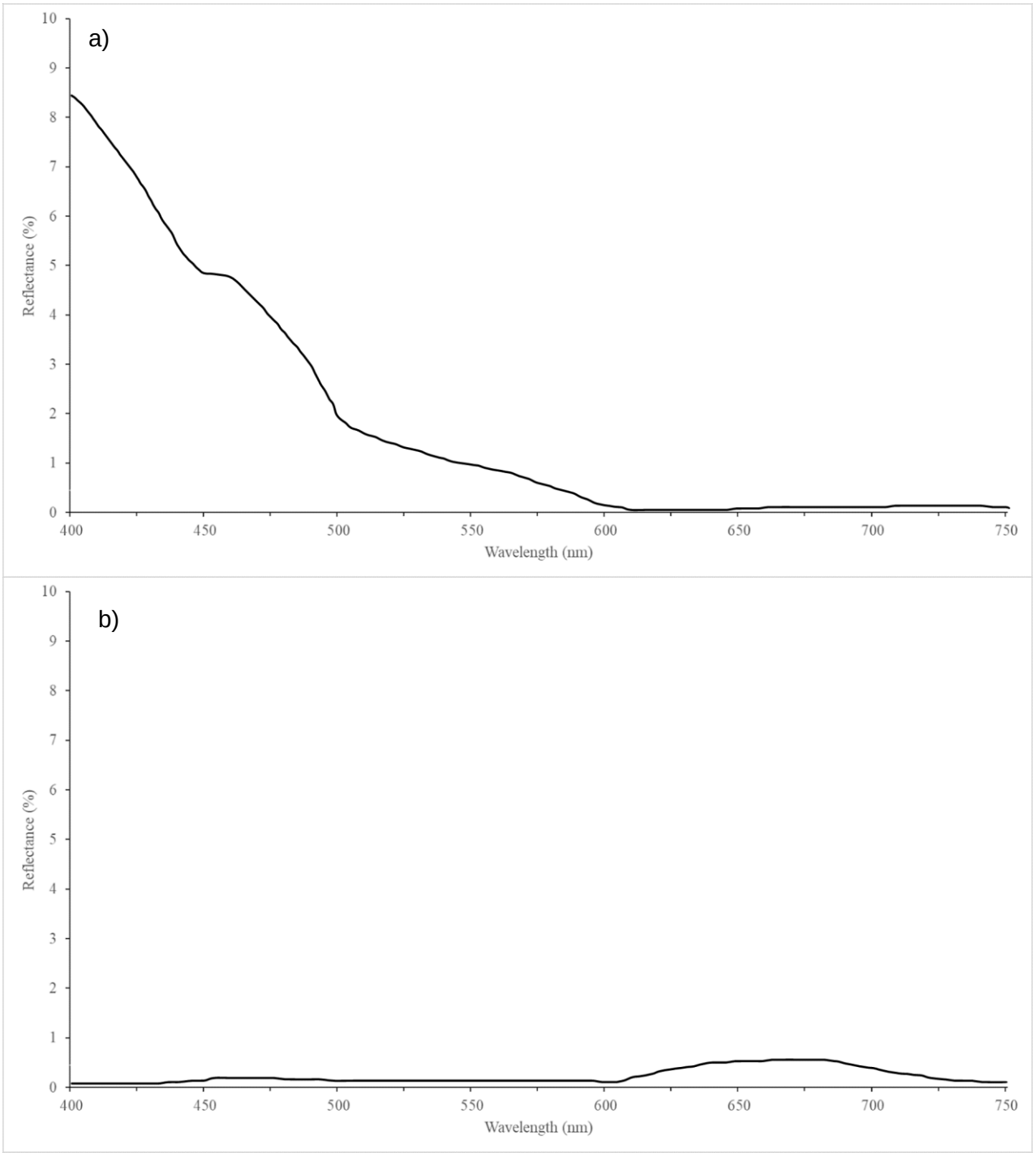
a)
Reflectance (%)
Wavelength (nm)
b)
Reflectance (%)
Wavelength (nm)

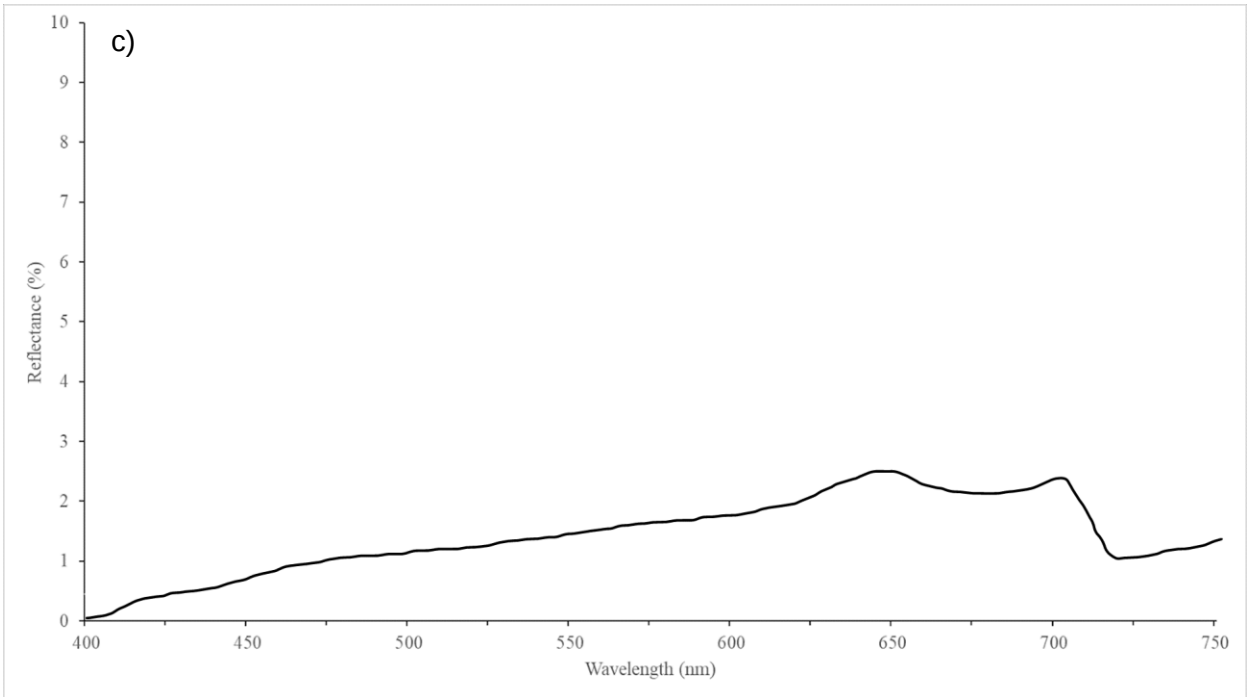
c)
Reflectance (%)
Wavelength (nm)
0
1
2
3
4
5
6
7
8
9
10
400
450
500
550
600
650
700
750

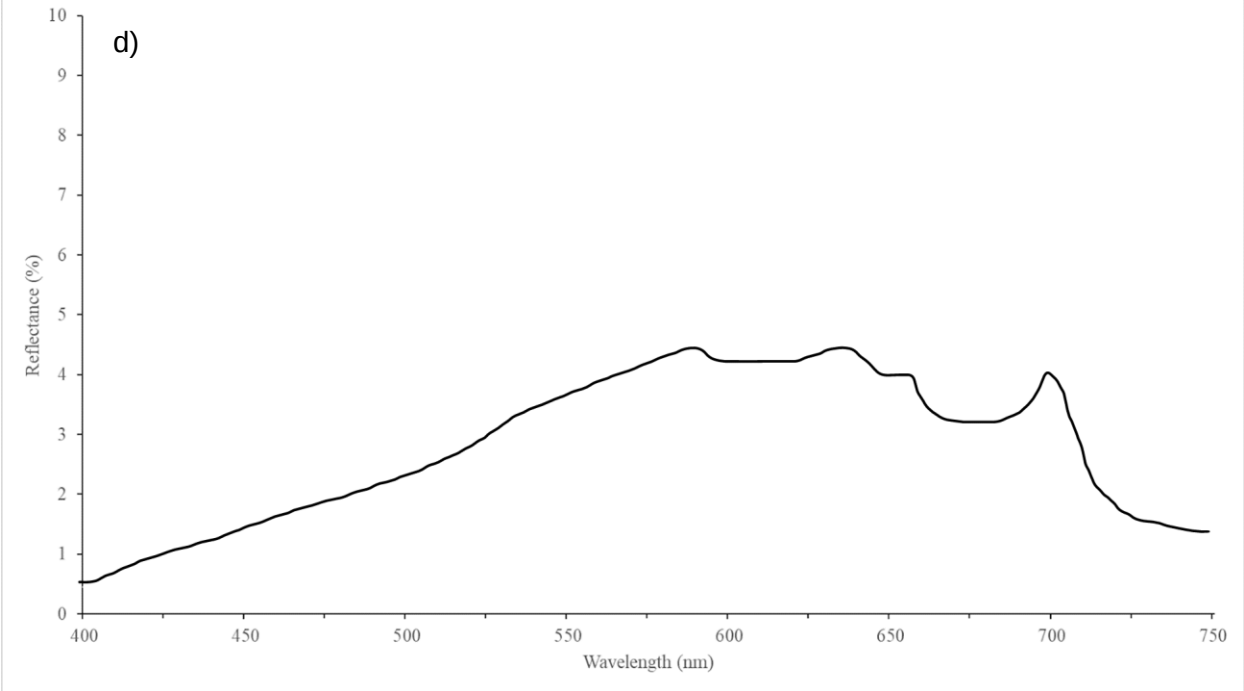
d)
Reflectance (%)
Wavelength (nm)
0
1
2
3
4
5
6
7
8
9
10
400
450
500
550
600
650
700
750

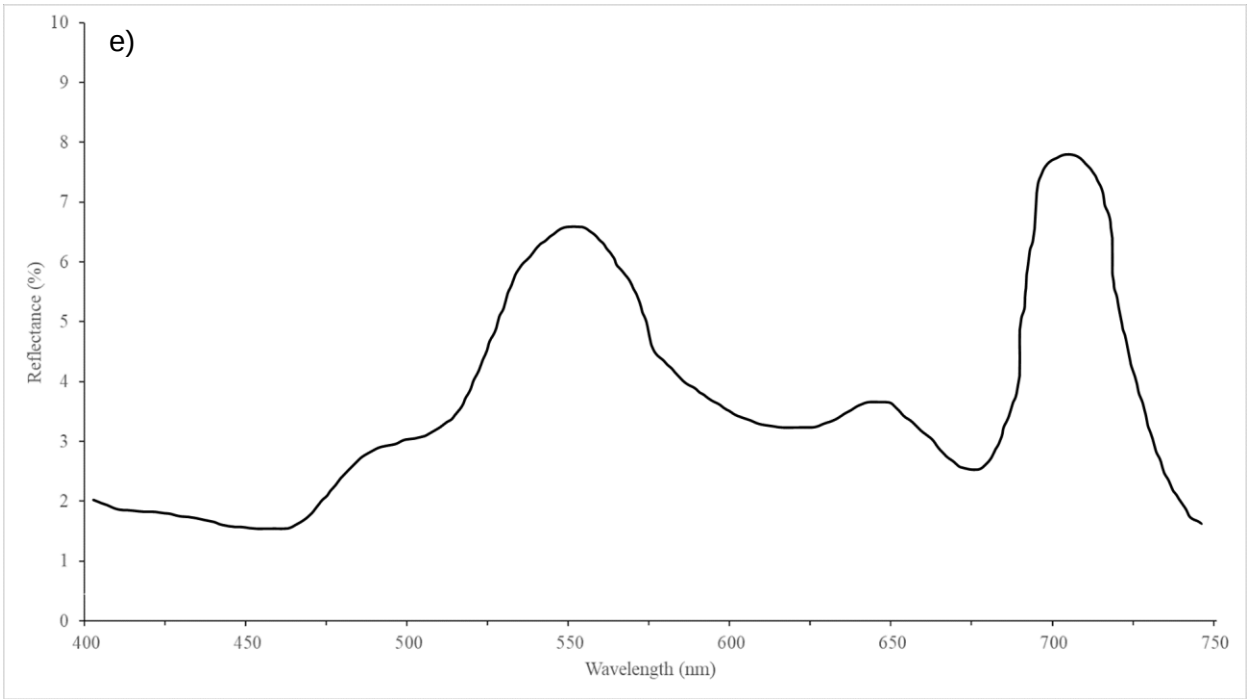

Figure 1.1a-e: Sample reflectance curves inspired from actual stations collected in Schalles (2006), demonstrating different reflectance curves in response to optically active constituent concentrations, including low chl-a, TSS and CDOM (a), high CDOM absorption (b), high TSS and CDOM absorption (c), average chl-a and TSS (d), and high chl-a (e).

Table 1.1: Sentinel 2A band wavelengths and resolutions. λ denotes the central wavelength, B is the bandwidth, Res. is the pixel size (spatial resolution), and SNR is the signal to noise ratio as calculated in (Pahlevan et al. (2017)

Band	**1**	**2**	**3**	**4**	**5**	**6**	**7**	**8**	**8a**	**11**	**12**
λ (nm)	444	497	560	664	704	740	783	843	865	1,613	2,200
B (nm)	20	55	35	30	15	15	15	115	20	90	175
Spatial Res. (m)	60	10	10	10	20	20	20	10	20	20	20
SNR	439	102	79	45	45	34	26	20	16	2.8	2.2

CHAPTER 2

METHODS

2.0 Introduction

This project includes analyses of bulk water sample data, close-range hyperspectral reflectance, and the atmospheric correction of water quality remote sensing imagery. A flow diagram detailing the methods for this project is represented in Figure 2.1 Station sites were determined before field sampling was conducted collecting bulk water samples for laboratory water quality analysis. Results from water quality analysis could then be used to characterize stations and sites into optical water types (objective 1). Additionally, close-range reflectance was used to determine both site and station optical water type. Sentinel-2 imagery was also downloaded and processed to evaluate atmospheric correction performance by comparing results to close-range reflectance values collected from *in situ* field sampling in line with objective 2.

2.1 Study Sites

The estuaries of three coastal Georgia rivers are included in this study (Figure 2.2a). Sampling locations were selected to capture a large dynamic range of water characteristics within a study site on a given day. Preliminary transects were selected along the river from the mouth in the upstream direction, approximately 1,000 or more meters apart to capture gradation within physical, chemical, and biological characteristics along the estuaries. Sampling site locations were then slightly adjusted when needed in the field to account for characteristics such as shallow or difficult-to-navigate waterways.

Tidal movement and weather conditions are considered when selecting sampling days because these factors can affect the number of stations that can be completed within a day. Tides

along the Georgia coast are classified as semi-diurnal, and an extreme tidal influence can reach up to three meters (NPS, 2021). Selecting sampling days with limited to no cloud cover that coincides with satellite flyover was critical, so comparisons could be made between the satellite imagery and ground data. 5-11 stations were completed in a full day, however, station ALA7 (3:15 pm), fell slightly outside of the ±3-hour time window (Figure 2.2a, Table 3.1). ALB 5, 6, 7, and 8 all are missing a Secchi depth measurement due to the instrument breaking in the field (Table 3.2).

2.1.1 Duplin River

The Duplin River located near Sapelo Island, Georgia, represents a region containing higher TSS content and lower CDOM values compared to the other sampling locations, which has led to higher reflectance in blue and green wavelengths in other studies (Schalles, 2006). Schalles (2006) reported a station mean TSS of 38.2mg/l at this site. The habitat surrounding the Duplin River is largely undeveloped salt marsh, with a small local community at Hog Hammock Historic District near the Duplin River (Schalles, 2013). The Duplin River feeds into Doboy Sound, where ten stations were collected over two days (Figure 2.2b). The region is heavily tidally influenced, and due to its location near the Altamaha River, is affected by discharge from the river. Residence times are two days on average, however, they can peak to as much as two or in extreme cases even three weeks (McKnight, 2016).

Of the Schalles (2006) reflectance and lab results, the Duplin River was characterized by average Chl-*a* (26.5 ug/L), average to high TSS (38.2 mg/L) and aCDOM at 440 nm (1.1 m^{-1}). The resulting Duplin River reflectance demonstrated an absorption trough of around 680 nm, and a reflectance peak at 580 nm of around 5.5%.

Sampling days include TRA (Test Run A, sampled on December 4, 2020) and TRB (sampled on October 31, 2020) (Figure 2.2b, Table 2.1). Field conditions on these days were not conducive to collecting cloud-free satellite imagery (Table 3.2*)*. For TRA stations, discharge from the Altamaha River was 123.5 m^3 sec^{-1} the previous day, and the average discharge rate for the 30 days leading up to sampling was 155.2 m^3 sec^{-1} (Table 3.1). For TRB stations, discharge the previous day was 249.5 m^3 sec^{-1}, and the 30 days leading up to sampling was 542.7 m^3 sec^{-1} (Table 3.1). Precipitation totaled 119 mm in the 30 days leading up to TRA stations being sampled, and 96 mm leading up to TRB stations being sampled (Table 3.1). Sampling for TRA stations (Figure 2.2b) was completed on a falling tide from a high of 2.1 meters above low tide. TRB stations were surveyed mostly on a rising tide, suggesting strong constituent mixing occurred (Table 3.1). These days were beneficial in establishing practical field research methods, testing and learning the equipment as well and collecting some preliminary data.

2.1.2 Altamaha River

The Altamaha River has the greatest discharge on the Georgia coast and is the third largest contributor of freshwater to the Atlantic Ocean from North America (Schafer and Alber, 2007). It is characterized as turbid with high concentrations of clay and low concentrations of dissolved organic carbon (Hladik, 2004; Alber, 2000). Daily mean discharge of the Altamaha River for 2020 was 602 m^3 s^{-1}, and prior-to-sampling discharge was recorded by the Doctortown stream gauge 40 miles upstream (USGS, 2021) (Table 3.1). Residence time averages a few days but can reach several weeks within some parts of the estuary system (Sheldon and Alber, 2002)

The Altamaha watershed is the largest of nine river basins in Georgia. It is fed from the Ocmulgee, Little Ocmulgee, Oconee, and Ohoopee watersheds, receiving water from Atlanta,

Macon, and Athens before draining into Altamaha Sound. The lower watershed contains the study site, receiving much of its water from groundwater sources and tidal flow, decreasing in its high clay content and turbidity with distance downstream and increasing in salinity towards the mouth, before arriving at the coastal plains where drainage is lower (EPD, 2004). Forestry and agricultural practices are a majority of the anthropogenic land use in the greater watershed, and contribute to a majority of non-point source pollution, however, the amount of pollution has not been quantified and is identified as a future need (Regional Water Plan Altamaha, 2023). In the Altamaha Water Basin, forest accounts for approximately half of the area's land use, and cropland accounts for just under a quarter of land use, but along the Altamaha River itself, this land use is closer to 32%, while impervious built-up area almost always accounts for less than 20%, however, most of this built-up area falls in the upper areas of the water basin (Georgia DNR, 2021; Takagi et al., 2017). Takagi et al. (2017) explored the nutrient dynamics across the Altamaha River Watershed over 2000-2012 found that the upper watersheds behave chemostactically, meaning the geochemical behavior of the discharge is affected by the within-system processes that affect the hydrochemistry of the water body. With this in mind, high nutrient concentrations can be attributed to anthropogenic factors.

Sampling days along the Altamaha River included ALA (Altamaha River route A, sampled on January 1, 2021), ALB (Altamaha River route B, sampled on January 23, 2021), and ALC (Altamaha River route C, sampled on April 8, 2021) (Figure 2.2c). Discharge the day prior to sampling was 549.3 m^3 sec^{-1} for ALA stations, 640 m^3 sec^{-} for ALB stations, and 453.1 m^3 sec^{-1} for ALC stations (Table 3.1). Average discharge for the 30 days leading up to sampling was 267.3 m^3 sec^{-1} for ALA, 538.6 m^3 sec^{-1} for ALB, and 447.3 m^3 sec^{-1} for ALC (Table 3.1). Precipitation leading up to sampling was 39 mm for ALA, 45 mm for ALB, and 223 mm for

ALC (Table 3.1). Tide varied 1.5 meters during ALA and ALB sampling days, and a little under 1 meter while ALC stations were sampled (Table 3.1). ALB fell from its high tide around two hours earlier in the day than ALA (Table 3.1). ALC was sampled under tidal conditions similar to TRB.

2.1.3 St. Marys River

The St. Marys River is a blackwater river on the Florida-Georgia border. The 130-mile-long river can be divided into three distinct sections; the Okefenokee Swamp headwaters, the Pinhook Swamp, and Cumberland Sound where tide influences marsh regions feeding in and out of the Atlantic (St. Marys River Management Plan, 2003). As water is sourced from the Okefenokee swamp, much of the biogeochemistry of the St. Marys River consists of low total suspended solids and high CDOM concentrations with a lower pH (Gates and Smith., 2008). Schalles (2006) recorded a station with CDOM absorption of 12.3 m^{-1} at 440 nm. Annual high tide discharge of the St. Marys River for 2020 is around 700 m^3 m s^{-1} (USGS., 2021). Human interaction with the St. Marys River is largely limited, with only 0.9% of basin land use being agricultural, however much of the surrounding economy derives from forestry with 48.5% of the basin classified as forest, which is dependent on the basin's health. Flow varies largely with rainfall and tidal influences, causing restrictions in fish productivity; however much of the river's classification is fishing use (EPD, 2014). No prior studies have been conducted detailing residence time for the St. Marys River.

The St. Marys River has been characterized by low Chl-*a* (0.93 ug/L), moderate TSS (5.18 mg/L), and extremely high aCDOM at 440 nm (12.3 m^{-1}) (Schalles, 2006). The resulting

St. Marys River reflectance has been recorded well below 1% for wavelengths between 400-800 nm (Schalles, 2006).

Sampling was conducted over one day at the St. Marys River, and St. Marys River route B (SMB) was utilized (Figure 2.2d). During the day and time of sampling, stations were recorded on a falling tide of 1.6 meters (Table 3.1). The mean discharge the day prior to sampling was 111 m^2 sec^{-1}, and the average discharge 30 days prior to sampling was 131 m^2 sec^{-1} (Table 3.1). Precipitation for the 30 days leading up to sampling was 165 mm.

2.2 Data Sources

Two primary sources of data were used in this study, including *in situ* data, and satellite imagery. Beyond these, some ancillary data was also collected, including discharge and tidal influence and times from the Altamaha River at the USGS station at Doctortown (USGS, 2023g) for Duplin River and Altamaha River sampling days, and discharge from the St. Marys River near Macclenny for its sampling day, along with tidal data from the USGS station Near Kingsland (USGS, 2023g) (Table 3.1). Precipitation 30 days prior to sampling was also collected at the UGAMI weather station (GCE LTER, 2023) for Duplin River and Altamaha River sampling days, and for the St Marys River sampling day, this same precipitation data was collected from the NOAA weather station at St. Marys (NOAA, 2018).

2.2.1 In Situ *Data*

During sampling, stations were navigated to with the use of a handheld Garmin GPS, and in addition to hyperspectral close-range reflectance discussed below, field measurements of depth, salinity on a gradient, and pH were collected by a YSI sonde (YSI, 2023). A 30cm Secchi disk was also used to record Secchi depth at each station as a visual measurement of turbidity.

2.2.1.1 Close-range Ocean Optics

For objectives 1 and 2 close-range hyperspectral reflectance data are used. Following the methods described in Schalles (2006) and Hladik (2004), spectral reflectance was obtained with the use of a pair of Ocean Optics USB 2000 spectrometers (Ocean Optics, Inc., Dunedin, Fl), one affixed to collected 180^{o} hemispherical solar downwelling irradiance (E_d) with the other collecting upwelling irradiance (L_w) from approximately 0.3 centimeters below the water's surface (Figure 2.3). It is important to note that below-water spectra and above-water spectra are different from each other, with above-water reflectance being susceptible to sun glint and surface waves (Bhatti et al., 2009). Approximately 2000 bands were collected from a spectral range of 350 to 1050 nm using a bandwidth channel of approximately 1.5 nm. Light was collected and filtered to the spectrometers through shielded fiber optics cables with an effective field of view of 23^{o}. To calibrate transfer functions, the upwelling radiance of a white Spectralon (Labshere, North Sutton, NH) reflectance standard was recorded simultaneously with incident irradiance prior to data collection. Upwelling radiance was recorded as an average of seven scans and was collected from each site in order to account for subtle variability.

Spectrometer data was fed to a digital converter card (Quatech QSP-100, Figure 4) from which computer-processed ratioed signals from the two fibers, creating a fractional percent spectral reflectance value, as calculated by equation 1. This was achieved using custom software titled "CALMIT Data Acquisition Program" (CDAP, which was written by Brian Leavitt at the Center for Advanced Land Management Technologies (CALMIT), Lincoln, NE). CDAP next converted reflectance data into a text format before it was imported into Microsoft Excel for further computation. A smoothing macro (written by Giorgio Dall'Olmo at CALMIT) next resampled data to one nm intervals across a 400 to 900 nm range, which simplified data analysis

by reducing 2000 wavelengths to a magnitude of 500. Spectra greater than three standard deviations from most of the curves were eliminated, as this is indicative of upwelling irradiance being recorded above the water's surface when the fiber optics cable is lifted above the surface of the water in response to wave action. Resampled spectra were next matched to Sentinel-2's MSI spectral bands by averaging the below-water reflectance across the wavelengths used by MSI for each band.

2.2.1.2 Laboratory water quality analysis

For each station, a bulk water sample of approximately four liters was taken for lab testing using cubitainers. For objective 1, following the methods of Schalles (2006) and Hladik (2004), water samples for each station were taken back to the lab, refrigerated, and analyzed within a day. Water samples were filtered through 47mm Gelman Type AE glass fiber filters (Figure 5) for Chl-*a* and TSS. Chl-*a* filters were first frozen overnight for the pigment to be preserved for extraction. Chl-*a* was then extracted from fiber filters in 10 ml of 90% acetone in a tissue grinder after being left in a freezer overnight in complete darkness. Filters were macerated using tissue grinders and then were centrifuged before the resulting extract was measured with a 10 cm quartz cuvette in a Spectronic Genesys II spectrophotometer (Spectronics, Inc). Total Chl-*a* in µg/L was then calculated with the trichromatic equation:

(3) $11.85 \times ABS(664\ nm) - 1.54 \times ABS(647\ nm) - 0.08 \times ABS(630\ nm)$ (American Public Health Association, 1989)

Chl-*a* measurements for each station were then recorded (Table 3.2).

To record TSS, water was processed through preweighed filters to record their "wet weight". Next, the preweighed filters were dried in an oven at 60^{o} for 24 hours. At this point,

filters were then reweighed, and any weight gain was in response to TSS dry weight added. The total mL of water processed through the filter was factored in using the following equation to determine TSS for each station sample in μg/L:

(4) $Dry\ weight - Tare \times 1000$

TSS measurements for each station were then recorded in Table 3.2.

CDOM absorption was measured from filtrate acquired from either the Chl-*a* or TSS process, using a 1 cm quartz cuvette, taking measurements at 40 nm intervals between 360 and 600 nm from the Genysis II spectrophotometer. CDOM is reported at absorption per meter at 440 nm.

2.2.2 Satellite Data

Satellite images were downloaded from the Copernicus Data and Information Access Service cloud environment (ESA, 2019) for sampling dates from the corresponding tile (Table 3.1). Satellite image analysis was completed with the use of ENVI software. Pixel values were extracted from a 3x3 pixel window centered at the observation station for greater analysis of spatial variability by taking the mean of all 9-pixel values.

2.2.2.1 Sentinel-2 MSI

For completion of objective 2, the satellite data was acquired from Sentinel-2A/B MSI. Sentinel-2 satellites A and B were launched on June 23, 2015, and March 7, 2017, respectively. MSI collects spectral information in 12 bands ranging from the visible to the SWIR and at three spatial resolutions (10, 20, 60 m) (Table 1.1). Six spectral bands of interest are relevant to water quality studies, and bands 2 (497 nm), 3 (560 nm), and 4 (664 nm) were resampled from 10-

meter to 20-meter spatial resolution (Table 1.1). Resampling pixels to a 20-meter spatial resolution allows for a uniform comparison between pixels and stations across all bands. With a 5-day revisit time, more field data at a slightly greater spatial resolution was collected in a shorter period than the use of Sentinel-2's closest counterparts from Landsat missions, and with a 185 km swath width, study sites are conveniently covered within the same tile to minimize the need to stitch multiple satellite tiles together (Drusch, et al., 2012).

2.2.2.2 Image Processing

Atmospherically uncorrected top-of-atmosphere imagery (L1C) was obtained to apply custom Sen2Cor and ACOLITE atmospheric correction methodologies. L1C imagery is radiometrically corrected and ortho-corrected to within less than 12 meters of absolute geolocation, and 5.5 meters of multitemporal region, meaning that a pixel is no further than 12 meters from the specific geolocation as recorded from the earth's surface, and that same pixel is no further than 5.5 meters from the same pixel sampled on a different date (95.5% confidence interval). L1C imagery once downloaded is processed following its respective atmospheric correction algorithm. For Sen2Cor correction, version 2.10.0 was implemented through the command line before preprocessing was conducted within the SNAP software. Tiles were spatially subset (N lat. 31.491, W Long. -81.747, S Lat. 30.663, and E Long. -81.158) and spectrally subset (bands 2-7, 8A, 11, and 12) (Table 1.1). All bands were resampled to 20 m spatial resolution.

2.2.2.3 Atmospheric Correction algorithms

The performance of an uncorrected product, and three satellite atmospherically corrected images were evaluated in this study (1) Sentinel-2 MSI level L1C top-at-atmosphere reflectance

that is not atmospherically corrected (ESAa); (2) Sentinel-2 MSI level L2A surface reflectance standard product generated by the ESA (ESAb); (3) Sentinel-2 MSI imagery corrected to surface reflectance using the SNAP software and Sen2Cor atmospheric correction processor (ESAc); and (4) Sentinel-2 MSI imagery corrected to surface reflectance using the ACOLITE atmospheric correction processor (RBINS, 2023). Differences between the L2A (2) and the SNAP product (3) expectedly were nonexistent, and as a result, the SNAP product was used for further analysis. A rural aerosol type was selected for the Sen2Cor correction product. No other settings were altered in either the ACOLITE or Sen2Cor correction as both products should automatically correct based on derived aerosol conditions. To assess the accuracy of these products (objective 2), they were compared to close-range hyperspectral reflectance data collected *in situ* (section 2.3.1 Close-range Hyperspectral Data).

2.3 Statistical Analysis

2.3.1 Close-range Hyperspectral Reflectance

The mean, standard deviation, and standard error were calculated for all laboratory analyses of Chl-*a*, TSS, and CDOM, grouped by site to determine site separability by optically active constituent (objective 1, Table 3.5). A nonparametric Kruskal-Wallis H test (one-way ANOVA on ranks) was performed to quantify the separability or similarity among all sites. If the site was significant, a post hoc Steel-Dwass nonparametric test for multiple comparisons was performed to evaluate site uniqueness between each of the sites. All statistical tests used an alpha value of 0.05, and p and z scores were recorded for each test as well as the N. All statistical tests were performed using JMP software (JMP 16, 2021).

2.3.2 Pearson Product-moment Correlation Matrix

A Pearson product-moment correlation matrix was also compiled to determine the relationship between the various optically active constituents in addition to Secchi depth. A Pearson product-moment correlation matrix was used in Kothari (2021), to identify the relationship between water quality parameters in drinking water. More like this study, Schalles and Hladik (2012) used a Pearson product-moment correlation matrix in case 2 coastal waters along the east and south US coastline, and Schalles (1998) has also used a Pearson product-moment correlation matrix for variables present within the water column of the estuarine mixing zone along coastal Georgia.

2.3.3 Hierarchical Clustering Dendrogram

To separate individual stations into optical water types (objective 1), water type classification was performed using hierarchical clustering based on bulk water analysis results of Chl-*a*, TSS, and CDOM as variables. JMP software was used to develop a hierarchical cluster dendrogram, capable of separating stations into groups with similar constituent concentrations. Hierarchical clustering merges all similar clusters from each individual sample- or in this case station- until they are all together in one cluster. This was achieved with Ward's clustering method, which agglomerates each group in a way that minimizes the within-group error. Essentially, the two groups combined are the two groups that are the most like each other. Utilizing a dendrogram can be difficult, as where to define clusters is somewhat arbitrary as this method is exploratory in nature, however best practice is to separate clusters at a point where there is a great distance for the next cluster to agglomerate (Nielson and Nielson, 2016). For this

project, clusters were defined primarily based on the distance between each cluster for the next agglomeration, a common method for separating clusters (Parlett, 2019).

With Hierarchical clusters created based on bulk water analysis of Chl-*a*, TSS, and CDOM, the Kruskal-Wallis H test and Steel-Dwass nonparametric tests were used to determine cluster uniqueness. Atmospheric correction performance was then evaluated based on the optical water type classified by the dendrogram (objective 2, Figure 2.1).

Following the same method of the hierarchical cluster dendrogram from bulk water analysis, a hierarchical cluster dendrogram was created from close-range hyperspectral reflectance for all wavelengths between 450 and 750 nm, and for close-range hyperspectral reflectance resampled wavelengths aligning with Sentinel-2's MSI bands (objective 1). From these hierarchical clusters, additional Kruskal-Wallis and Steel-Dwass nonparametric tests were performed to determine site uniqueness based on spectral reflectance. Additionally, the hierarchical cluster dendrograms created from both the bulk water sample and close-range reflectance were also compared to determine their differences using the same statistical methods.

2.3.4 Atmospheric Correction Performance

To assess the performance of atmospheric correction (objective 2), in line with existing literature (Mograne et al., 2019; Martins et al., 2017; Page et al., 2019), a simple statistical intercomparison between atmospheric processors and *in situ* close-range ocean optics reflectance (resampled to Sentinel-2 MSI bands) was conducted. This intercomparison is completed with the use of Pearson's product correlation (equation 4), root mean square difference (RMSD), (equation 5), mean absolute percent difference (MAPD) (equation 6), to provide comparative statistics indicating atmospheric correction effectiveness at each band for each processor at each

station, or optical water type classification. A smaller RMSD and MAPD value means the atmospheric correction product is performing better within that bandwidth according to the close-range hyperspectral reflectance.

(4) $R^2 = \frac{(\Sigma(xi-x)\ (yi-y)}{\sqrt{\Sigma(xi-x)\Sigma(yi-y)^2}}$

(5) $RMSD = \sqrt{\frac{1}{N} \times \sum_{i=1}^{N}(xi - xe)^2}$

(6) $MADP = \frac{\Sigma|(xi-xe)|}{xi} \times 100$

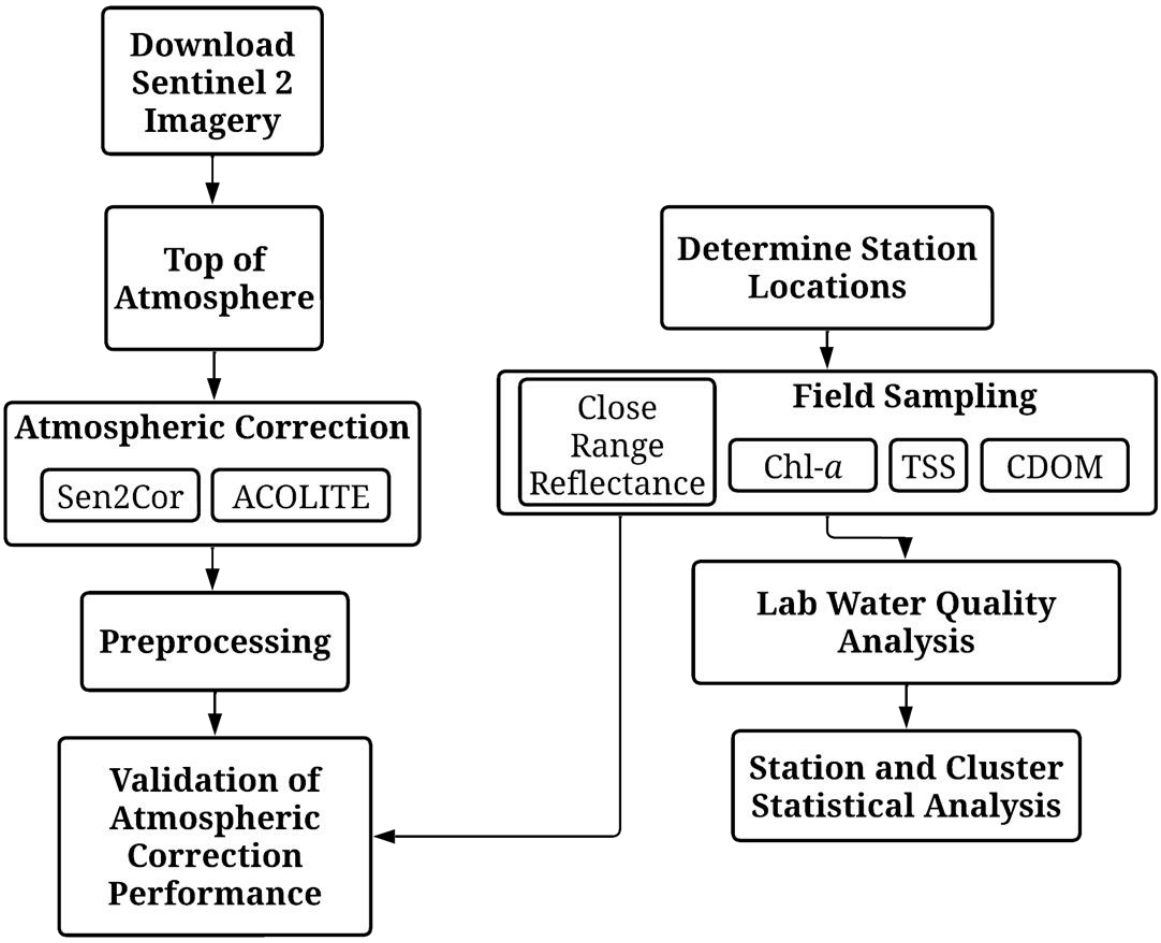

Figure 2.1: Workflow Diagram detailing the steps taken for the methods of this project. The left side of the figure follows the steps for objective 2, while the right side shows the steps for objective 1.

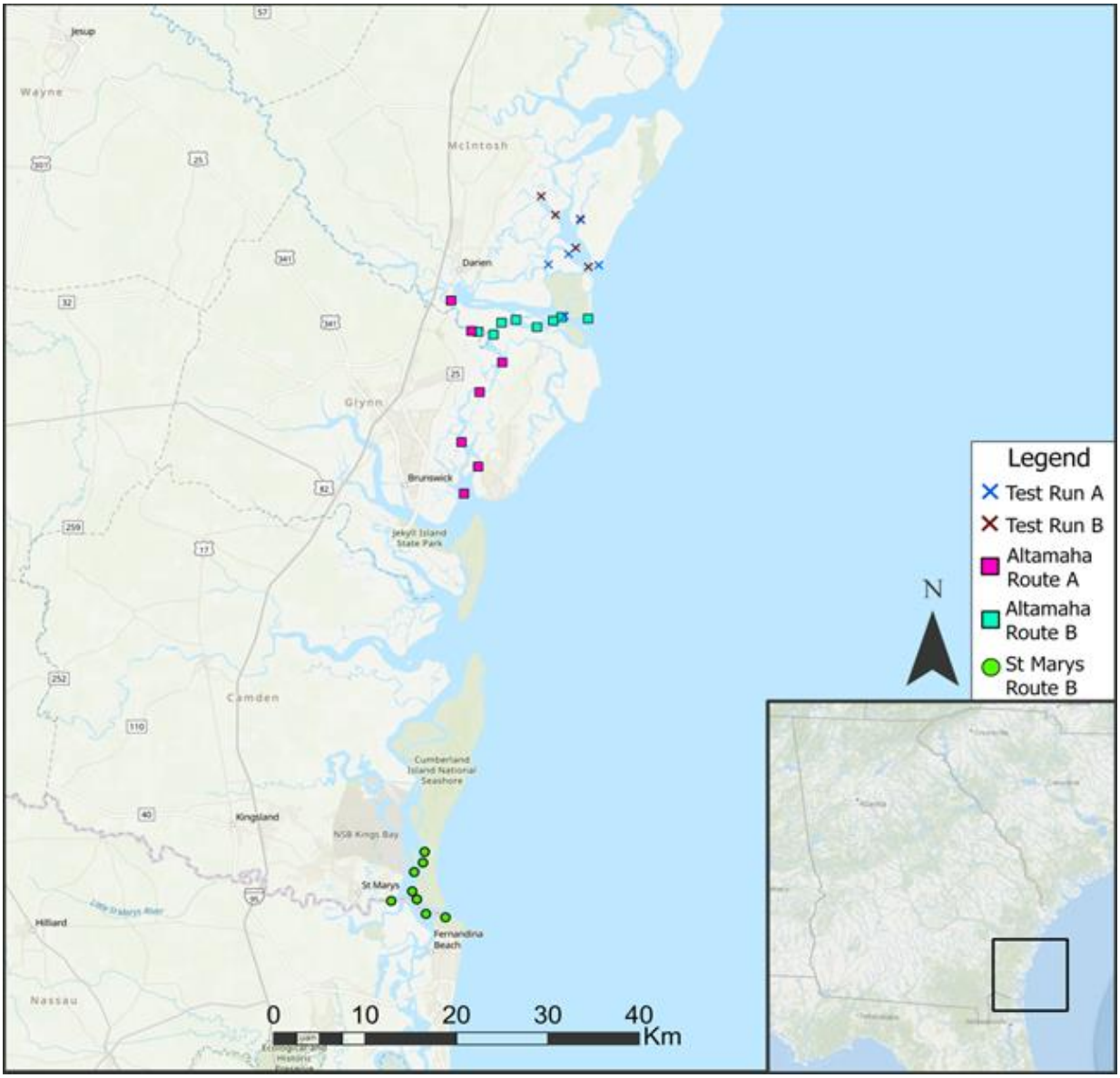

Figure 2.2a: Overview map of the Georgia coastline showing the location of all stations sampled. Crosses denote a Duplin River station. Squares indicate an Altamaha River station, and the circles were stations sampled from St. Marys river.

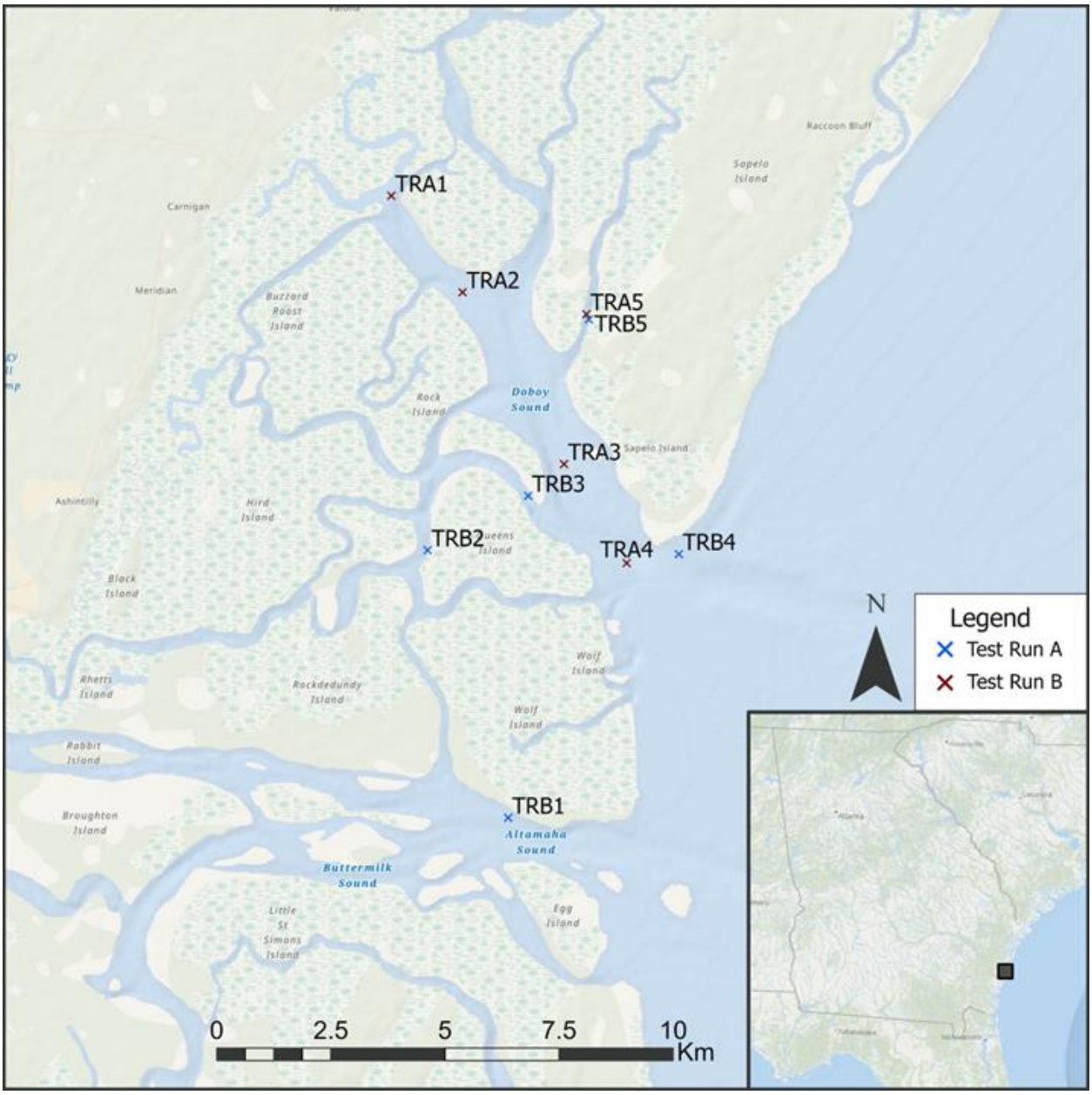

Figure 2.2b: Site map detailing the location of all Duplin River stations. Five TRA stations (red crosses) were sampled on December 4, 2021. Five TRB stations (blue crosses) were sampled on October 30, 2021.

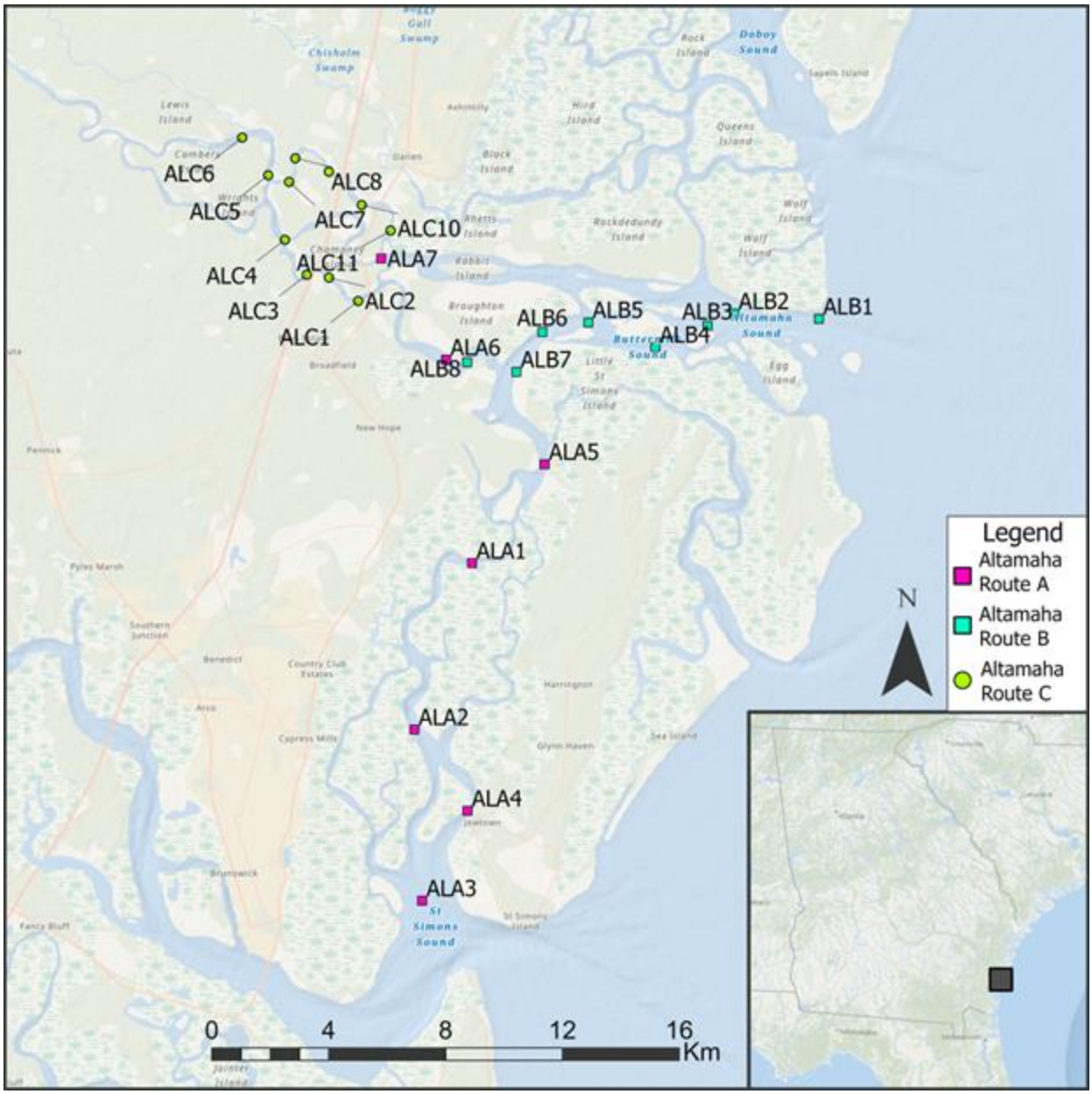

Figure 2.2c: Station map detailing the location of all Altamaha River stations. Seven ALA stations (pink squares) were sampled on January 8, 2022. Eight ALB stations (teal squares) were sampled on January 23, 2022. Eleven ALC stations (green circles) were sampled on April 8, 2022.

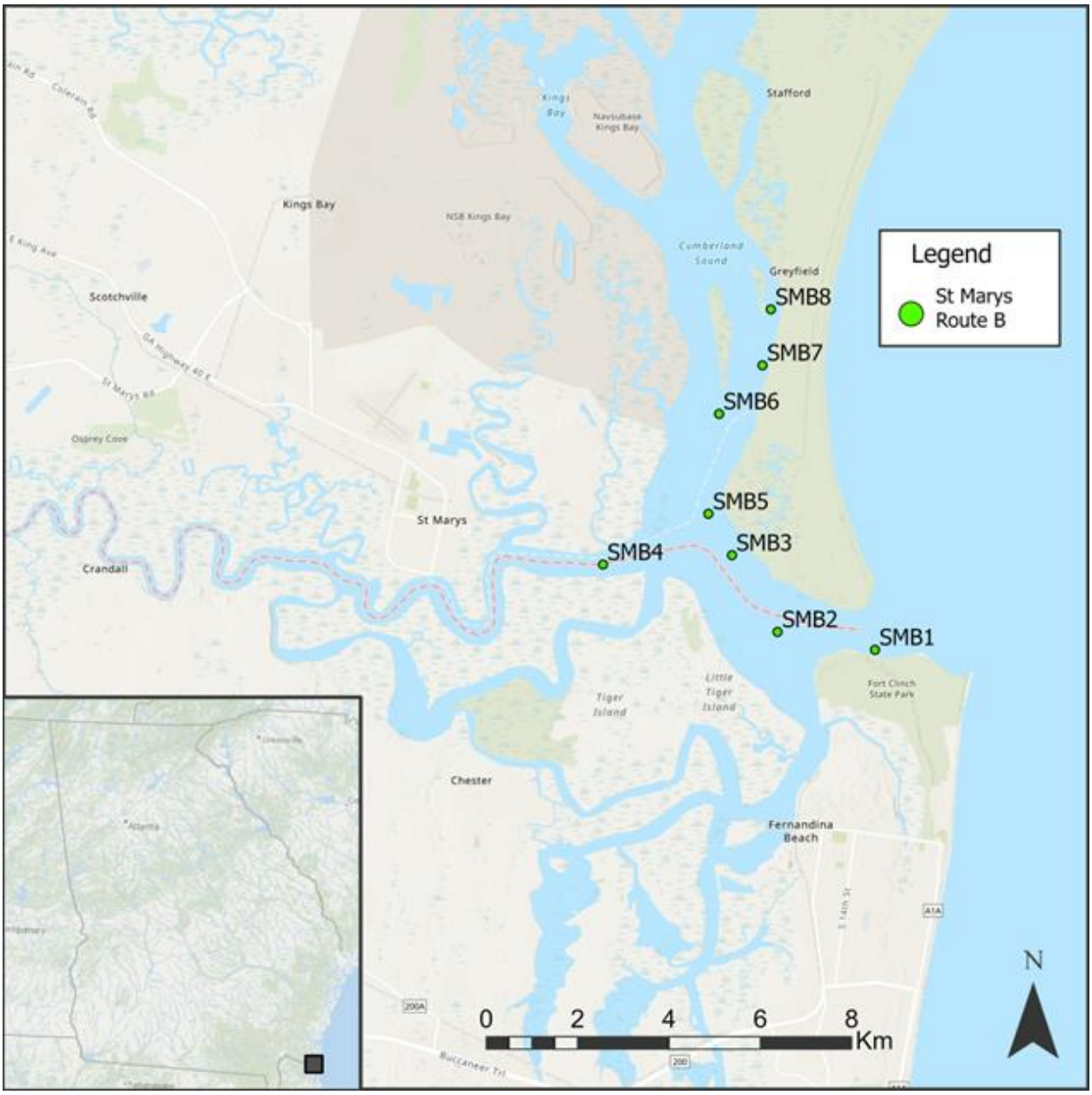

Figure 2.2d: Station map detailing the location of all St. Marys River stations (SMB), where eight stations (green circles) were sampled on April 23, 2022.

Figure 2.3: Collecting a close-range hyperspectral reflectance scan with Ocean Optics USB2000 fiber optics, just below the water's surface.

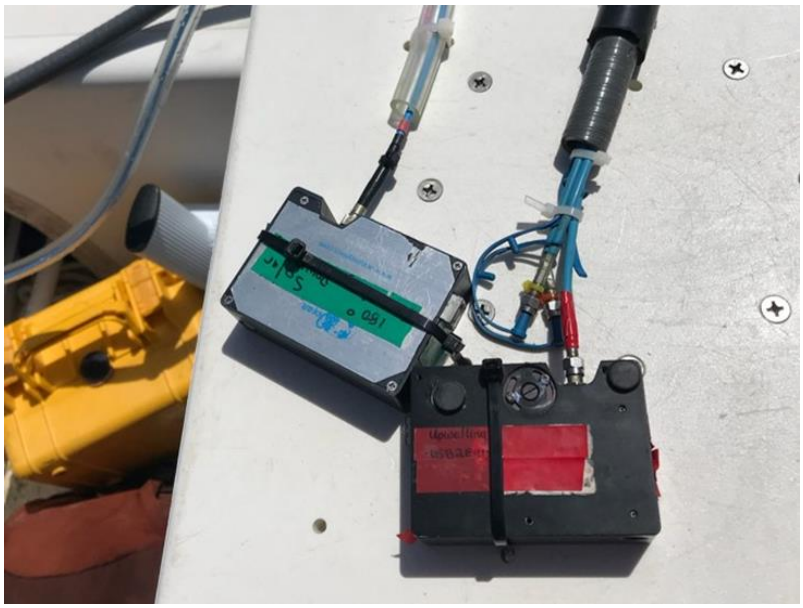

Figure 2.4: Digital converter cards used to receive incoming upwelling and downwelling reflectance.

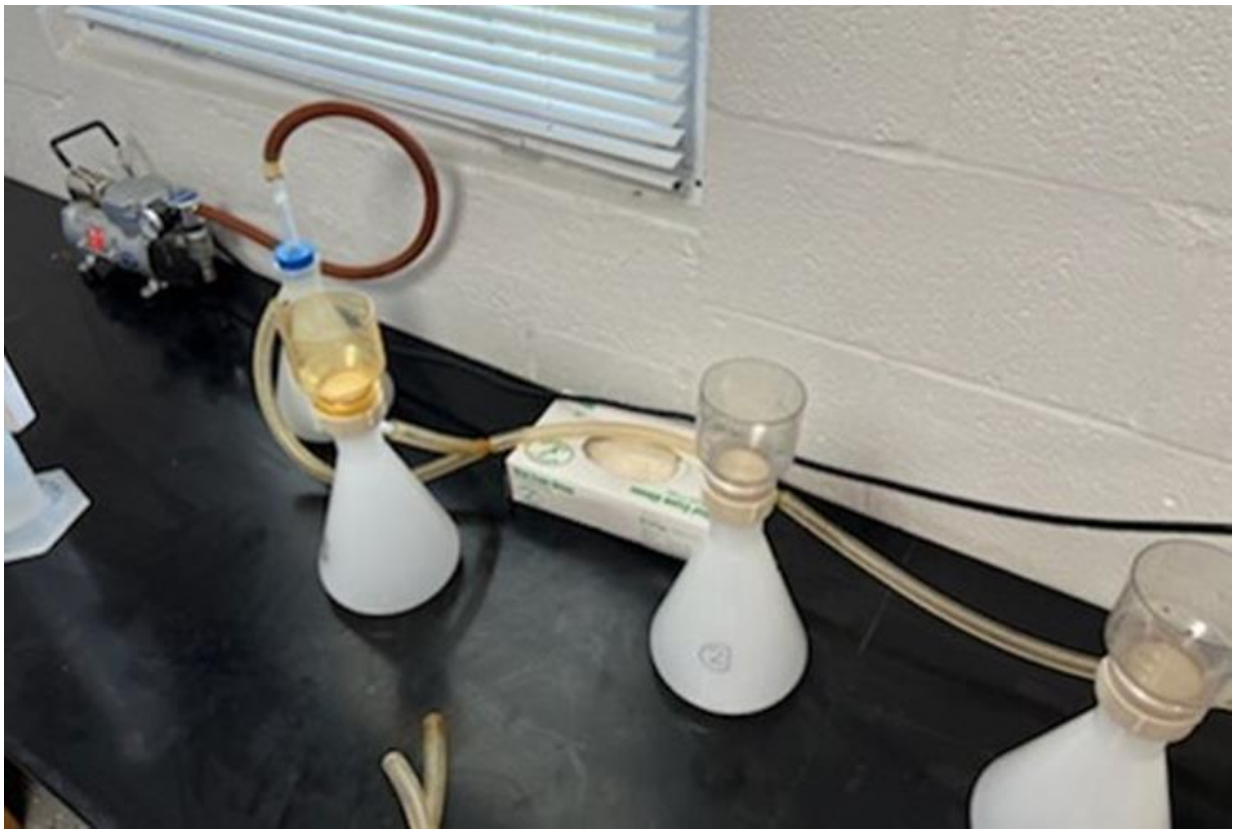

Figure 2.5: Filter system utilized for processing bulk water samples through fiber filters for Chl-a and TSS quantification. Filtrate collected here was used to measure aCDOM absorption in a spectrophotometer.

CHAPTER 3

RESULTS

3.0 Introduction

Over six field sampling days, a total of 44 stations were sampled, with 41 close-range hyperspectral reflectance curves collected, 31 satellite reflectance curves obtained within a 3x3 window around a station, resulting in 28 close-range reflectance curves matching up to its corresponding satellite reflectance. CDOM absorption was collected for all 44 stations, Chl-*a* results were included for 43 stations, and TSS was included from 40 of the stations (Table 3.3).

3.1 In Situ *Data Collection and Analyses*

In situ data was collected from a small vessel with a crew of 3-4 members. Stations were navigated with a handheld Garmin GPS, and an anchor was thrown overboard to secure the boat in place while necessary data was collected. A station could be completed in approximately 20 minutes when navigated with a crew this size.

3.1.1 In Situ *Environmental Data*

Depths varied by station, averaging 6.8 meters at Duplin River stations, 5.2 meters at Altamaha River stations, and 7.9 meters at St. Marys River stations ranging from 10.7 meters at station SMB6 to 1.3 meters at station ALC9 (Table 3.1). Shallow stations included ALC 4, 7, 8, 9, and 10, which were all sampled on the same channel in the Altamaha River (Table 3.1, Figure 2.2c). SMB stations were generally deeper stations in more open waters near the mouth of the St. Marys River, like at station SMB1, with a depth of 9 meters, and through Cumberland Sound, like at the SMB6 stations (Table 3.1, Figure 2.2d).

The St. Marys River, with Secchi depths ranging from 0.7 to 1 meter with an average of 0.8 meters, had deeper Secchi depths than the Altamaha River, which averaged 0.6 meters and ranged from 0.4 to 1 meter, and Duplin River stations, which averaged 0.6 meters and ranged from 0.25 to 1.3 meters (Table 3.2). It is worth mentioning that Secchi depths were not recorded for stations ALB 5, 6, 7, and 8, as the Secchi disk broke while in the field.

3.1.2 In Situ *Bulk Water Samples and Type (Objective 1)*

To conduct station and cluster statistical analysis (Figure 2.1), stations were initially separated by site (Duplin River, Altamaha River, and St. Marys River) (Figure 2.2a-d) and bulk water sample lab results were used to classify each site (Table 3.5). At Duplin River stations, TRA 2, 3, and 4 had TSS values of more than three standard deviations (SD = ±19.14 mg/L) from the overall station mean of 21.605 mg/L and were removed from results and further analysis (Table 3.3, Table 3.5). ALC6 did not have a recorded TSS value due to an error in the lab (Table 3.4). All sites had Chl-*a* concentrations that were largely consistent with the overall station mean of 2.786 μg/L and fell within three standard deviations (SD= ±1.431 μg/L), after removing an outlier at TRB3 of 20.462 μg/L (Table 3.4). No outliers in aCDOM at 440 nm were recorded (Table 3.3).

At Duplin River stations, Chl-*a* ranged from 1.546 μg/L at TRB1 to 6.918 μg/L at TRB4, had a mean of 1.605 μg/L, with a standard deviation of ±0.54 μg/L (Table 3.5). TSS ranged from 17.681 mg/L TRB1 to 65.026 mg/L at TRA1, had a mean of 40.555 mg/L, and a standard deviation of ±23.71 mg/L, and aCDOM ranged from 0.039 m^{-1} at TRA4 to 0.227 m^{-1} at TRB2 and TRB5 at 440 nm had a mean of 0.134 m^{-1}, with a standard deviation of ±0.137 m^{-1}, and this absorption amount decreased with stations closer to offshore (Figure 2.2b, Table 3.5).

At Altamaha River stations, Chl-*a* ranged from 0.978 µg/L at ALB4, to 7.217 µg/L at ALC10, had a mean of 2.257 µg/L, with a standard deviation of ±0.1.249 (Table 3.5). TSS ranged from 0.405 mg/L at ALC8 to 68.396 mg/L at ALA3, had a mean of 13.239 mg/L, and has a standard deviation of ±15.04 mg/L (Table 3.5). aCDOM at 440 nm ranged from 0.019 m^{-1} at ALA3 to 0.369 m^{-1} at ALB8 and had a mean of 0.232 m^{-1} with a standard deviation of ±0.109 m^{-1} (Figure 2.2b, Table 3.5).

At St. Marys River stations, Chl-*a* ranged from 3.023 µg/L at SMB2, to 4.791 µg/L at SMB3, with a site mean of 4.083 µg/L, and a standard deviation of ±0.795 µg/L (Table 3.4, Table 3.5). TSS ranged from 20.552 mg/L at SMB4, located upriver from Cumberland Sound to a high of 45.558 mg/L at SMB5 between the St. Marys River mouth and Cumberland Sound, with a site mean of 31.166 mg/L, and a standard deviation of ±8.336 mg/L (Table 3.4, Table 3.5). CDOM ranged from absorption at 440 nm of 0.125 m^{-1} at SMB2 to a high of 0.479 at SMB4, with a site mean of 0.134 m^{-1}, and a standard deviation of ±0.115 (Table 3.4, Table 3.5).

A Kruskal-Wallis H test was conducted to determine if a site was unique based on the recorded lab observations (Figure 3.1a-c). Chl-*a* content between the St Marys site and the Altamaha site was different (p=0.002, z=3.340), as St. Marys River stations recorded a higher Chl-*a* content across most stations (Table 3.2, Figure 3.1a). TSS was significantly lower for the Altamaha site in comparison to both the Duplin River (p=0.011, z=2.872) and St. Marys River sites (p=0.002, z=3.340) (Figure 3.1b). CDOM content was not significantly separated by any of the sites (Figure 3.1c).

As part of Laboratory water quality analysis (Figure 2.1), the water quality constituent Pearson product-moment correlation matrix (Table 3.6) highlights the relationship between each

OAC and Secchi depth, in addition to whether the correlation was significant. TSS and Chl-*a* were positively correlated (r=0.377, *p*=0.0.16), while TSS and CDOM were strongly negatively correlated (r=-0.706, *p*=<0.001). The only other significant correlation within the constituents was Chl-*a* to Secchi (r=0.449, *p*=0.004) (Table 3.6).

3.1.3 In Situ Bulk Water Sample Hierarchical Clustering

To complete statistical analysis with the bulk water samples (Figure 2.1), hierarchical clustering (Figure 3.2**)** was used to separate the stations by water type (objective 1). Clusters were separated into three major groups, as there was a great distance for any of the clusters to agglomerate, meaning the clusters were distant in their relationship from each other. Lab cluster 1 was home to four Duplin River stations, four Altamaha River stations, and seven St. Marys River stations. Lab cluster 2 included just one Duplin River and one St. Marys River station, along with 13 Altamaha River stations. Lab cluster 3 included one Duplin River station, and eight Altamaha River stations (Figure 3.2). TRA 2, 3, 4, and ALC6 were not included in a lab cluster as these stations did not have results for all OACs (Table 3.3).

When relating the lab clusters to water variables, in lab cluster 1 a significantly higher Chl-*a* content was observed from both cluster 2 (*p*=<0.001, z=3.857) and cluster 3 (*p*=<0.001, z=3.995), with values ranging from 2.38 µg/L at ALA3 to ALC10 at 7.22 µg/L (Figure 3.3a). TSS for cluster 1 had the greatest range when compared to the other clusters (Figure 3.3b). TSS values ranged from 25.033 mg/L at SMB3 to 68.399 mg/L at ALA3, and TSS was significantly separable in cluster 1 from cluster 2 (*p*=<0.001, z=4.480), and from cluster 3 (*p*=0.005, z=-3.160) (Figure 3.3b). Stations with the largest TSS measurements all fell into lab cluster 1 (Table 3.7). Lab cluster 1 was also categorized by lower-than-average aCDOM (Figure 3.3c) ranging

from 0.019 m^{-1} absorption at 440 nm at ALA3 to 0.304 m^{-1} at ALC10. aCDOM in cluster 1 was significantly separable from cluster 2 (p=<0.001, z=4.439), but not cluster 3 (p=0.772, z=0.686) (Figure 3.3c), Overall, cluster 1 is largely characterized by high Chl-*a* content (mean=4.166 µg/L, SD= ±1.399), a wide range of TSS content (mean=39.527 mg/L, SD= ±18.663), and lower CDOM concentration (mean=0.137 m^{-1}, SD= ±0.924 m^{-1}) (Table 3.7, Figure 3.3a-c).

The defining characteristic of lab cluster 2 was high CDOM absorption (Figure 3.3c). Cluster 2 included every station with a value above the mean (0.207 m^{-1}) of all stations, ranging from 0.273 m^{-1} at ALA7 to 0.476 m^{-1} for SMB4, however, cluster two was not separable from cluster 1 based on CDOM absorption (p=0.772, z=0.686), but was separable from lab cluster 2 (p=<0.001, z=3.997) (Table 3.7). Lab cluster 2 Chl-*a* content (mean=4.166 µg/L, SD= ±1.399 µg/L) was not statistically different from lab cluster 3 (p=0.136, z=1.908) (Figure 3.3a, Table 3.7). Lab cluster 2 Chl-*a* content ranged from a low of 1.299 µg/L at ALA7 to 3.833 µg/L at SMB4 (Figure 3.3a). TSS content was lowest in lab cluster 2 (mean= 6.558 mg/L, SD= ±5.904 mg/L), well below a majority of the stations in lab cluster 1 (mean= 39.527 mg/L) and some in lab cluster 3 (mean = 17.183 mg/L) (Figure 3.3b). TSS ranged from 0.405 mg/L at ALC8 to 20.552 mg/L at SMB4.

Lab cluster 3 represented stations primarily sampled from the Altamaha River, and OACs were all generally lower in comparison to lab clusters 1 and 2 (Table 3.7, Figure 3.3a-c). Lab cluster 3 Chl-*a* was comparable to lab cluster 2 and ranged from 0.978 µg/L at ALB4 to 2.212 µg/L at ALB2 with a mean of 1.594 µg/L (SD= ±0.448 µg/L) (Table 3.7). TSS ranged from a low of 3.8 mg/L at ALC2 to a high of 34.031 mg/L at ALA5 with a mean of 17.183 mg/L (Table 3.7). While slightly higher than lab cluster 2, lab cluster 3 still fell below the overall mean TSS of all stations (21.605 mg/L). CDOM absorbance (mean=0.159 m^{-1}, SD= ±0.054 m^{-1}) was

similar to lab cluster 1, however did not include as many low stations (Figure 3.3c). Lab cluster 3 CDOM absorption at 440 nm ranged from 0.102 m^{-1} at ALB3 to 0.208 m^{-1} at ALA5 (Figure 3.3c).

3.1.4 In Situ *Close-range Reflectance Samples and Types*

As part of the water quality analysis (Figure 2.1), close-range hyperspectral reflectance spectra by the site are summarized in Figure 3.6a-c. Close-range reflectance was excluded from ALC1, SMB3, and SMB4, due to errors in field data collection. The Duplin River spectra appear to be heavily influenced by TSS, as reflectance values peak within the red to near-infrared region of the electromagnetic spectrum. A minimal Chl-*a* trough is present in most close-range hyperspectral reflectance curves, however TRB4 has a more substantial Chl-*a* trough at 670 nm and a reflectance peak near 580 nm. Altamaha River spectra are largely consistent with the trends of the Duplin River site. ALA3 has notable Chl-*a* features present, like that found in TRB4's reflectance. Except for SMB8, St. Marys River stations have low reflectance values not exceeding a value of 2%, consistent with absorption from CDOM.

3.2 Satellite Data Collection and Analyses

3.2.1 Close-range Reflectance Data and Satellite Imagery Matchups

For the validation of atmospheric correction performance (Figure 2.1), Resampled close-range reflectance to match Sentinel-2 bandwidths for Sentinel-2's MSI top-of-atmosphere reflectance (L1A), and both Sen2Cor and ACOLITE atmospherically corrected spectra for the significant satellite bands relevant to water quality remote sensing appears per station in the panels for figure 3.7a-d. Satellite imagery for TRA and TRB sampling days was not used due to cloud cover interfering with reflectance (Table 3.3). Satellite reflectance was also not included

from ALA 5, 6, and 7 due to cloud and shadow interference, meaning 28 stations have close-range reflectance and satellite reflectance that match-up (Table 3.3).

In the same way bulk water samples were used to create hierarchical clusters, hyperspectral close-range reflectance between 450 nm and 750 nm was used to create hierarchical clusters (Figure 3.4a). Four Duplin River stations, 15 Altamaha River stations, and five St. Marys River stations are included in hyperspectral cluster 1. In hyperspectral cluster 2, there are two Duplin River stations, six Altamaha River stations, and one St. Marys River station. Hyperspectral cluster 3 includes four Duplin River stations, and four Altamaha River stations (Figure 3.4a). ALC1, and SMB 3 and 4 were not included as these stations contained errors in the close-range reflectance data.

Based on the Kruskal-Wallis H test, the hyperspectral clusters did not have significantly different Chl-*a* (p=0.791), or TSS (p=0.22) concentrations between the clusters. There was however a significant difference within CDOM absorption of the hyperspectral clusters (p=0.008, f=5.448). A Steel-Dwass nonparametric test was run and determined that there is a significant difference in CDOM absorption at 440 nm between hyperspectral cluster 1, and hyperspectral cluster 2 (p=0.012, z=2.851).

A hierarchical cluster analysis was also performed using resampled wavelengths to match the Sentinel-2 MSI sensor's bandwidths for bands 2 (479 nm), 3 (560 nm), 4 (664 nm), 5 (704 nm), and 6 (740 nm) (Table 1.1, Figure 3.4b). Resampled cluster 1 included three Duplin River stations, three Altamaha River stations, and five St. Marys River stations. Resampled cluster 2 consisted of two Duplin River stations, three Altamaha River stations, and four St. Marys River stations. Resampled cluster 3 had four Duplin River stations, nine Altamaha River stations, and

one St. Marys River station (Figure 3.4b). ALC1, and SMB 3 and 4 were not included as these stations contained errors in the close-range reflectance data. From the hyperspectral hierarchical cluster tree to the resampled hierarchical cluster tree (Figure 3.4a-b), stations ALA7, ALB 5, 6, 7, 8, and SMB 8 moved from cluster 2 to cluster 3 in the resampled hierarchical cluster. Clusters for both the hyperspectral and resampled hierarchical trees were separated into three branches, as the clusters formed had a substantial distance to agglomerate.

The resampled clusters did not have significantly different Chl-*a*, TSS, or CDOM based on bulk water sample analysis (Figure 3.5a-c). Chl-*a* (p=0.358, f=1.057) (Figure 3.5a), TSS (p=0.921, f=0.083) (Figure 3.5b), and CDOM (p=0.400, f=0.940) (Figure 3.5c), were not significantly different from one another based on the Kruskal-Wallis H test (Figure 3.5a-c). The lab statistics are summarized for these clusters in Table 3.8.

Grouped reflectance spectra based on resampled close-range reflectance hierarchical clusters (Figure 3.8a-c) show some difference in reflectance, however, this difference largely relates to intensity more than shape. In cluster 1, a low reflectance value can be observed across all wavelengths not exceeding a 3% reflectance value. There is a minimal Chl-*a* trough in cluster 1 at approximately 680 nm when compared to cluster 3 and even some spectra in cluster 2 (Figure 3.8a). Cluster 2 represents an increase in overall reflectance with some spectra exceeding 4%. A distinct peak becomes more visible at 580 nm (Figure 3.8b). Cluster 3 represents spectra with the greatest reflectance intensity with most curves exceeding 4% reflectance at 5,860 nm where most curves show a peak (Figure 3.8c). A reflectance trough can also be seen in most spectra at 680 nm. The main deciding factor in where resampled reflectance curves are clustered appears to be in relation to the intensity of reflectance.

3.2.2 Sentinel-2 MSI Reflectance Samples and Type (Objective 2)

To determine the performance of each atmospheric correction processor, a linear regression analysis by band with resampled close-range reflectance was conducted (Table 3.9). The uncorrected L1C reflectance appears to perform well based on a strong significant correlation value in band 2 (497 nm) (r^2=0.494, p=<0.001), band 3 (560 nm) (r^2=0.624, p=<0.001), band 4 (664 nm) (r^2=0.349, p=<0.001), band 5 (704 nm) (r^2=0.241, p=0.008), and band 6 (740 nm) (r^2=0.145, p=0.046) (Table 3.9). A negative slope, high intercept, and high error values from RMSD and MAPD tell us this correlation is negative and contains a larger amount of variation than seen in both the Sen2Cor and ACOLITE reflectance.

When comparing Sen2Cor and ACOLITE on a band-to-band basis, ACOLITE performs better in all bands. In band 2 (497 nm), Sen2Cor did not demonstrate a significant correlation (p=0.417), while ACOLITE did (r^2=0.33, p=0.001), with slightly higher RMSD (ACOLITE RMSD=0.717, Sen2Cor RMSD=0.7), but lower MAPD (ACOLITE MAPD=138.167, Sen2Cor MAPD=232.47) (Table 3.9). Both Sen2Cor and ACOLITE had significant correlations to resampled close-range reflectance in band 3 (560 nm) (Sen2Cor r^2=0.299, p=0.003; ACOLITE r^2=0.33, p=0.001), band 4 (664 nm) (Sen2Cor r^2=0.192, p=0.02; ACOLITE r^2=0.319, p=0.002), and band 5 (704 nm) (Sen2Cor r^2=0.061, p=<0.001; ACOLITE r^2=0.215, p=0.013), but neither Sen2Cor or ACOLITE had a significant correlation for band 6 (740 nm) (Sen2Cor p=0.101, ACOLITE p=0.813) (Table 3.9). In band 3 (560 nm), ACOLITE had a lower RMSD and MAPD (RMSD=0.807, MAPD=78.097) than Sen2Cor (RMSD=0.857, MAPD=116.485), and this trend continued in band 4 (664 nm) (ACOLITE RMSD=0.888, MAPD=65.092; Sen2Cor RMSD=0.899, MAPD=91.054), band 5 (704 nm) (ACOLITE RMSD=0.825, MAPD=74.882;

Sen2Cor RMSD=0.846, MAPD=99.18.3), as well as band 6 (740 nm) (ACOLITE RMSD=0.782, MAPD=247.744; Sen2Cor RMSD=0.799, MAPD=258.918).

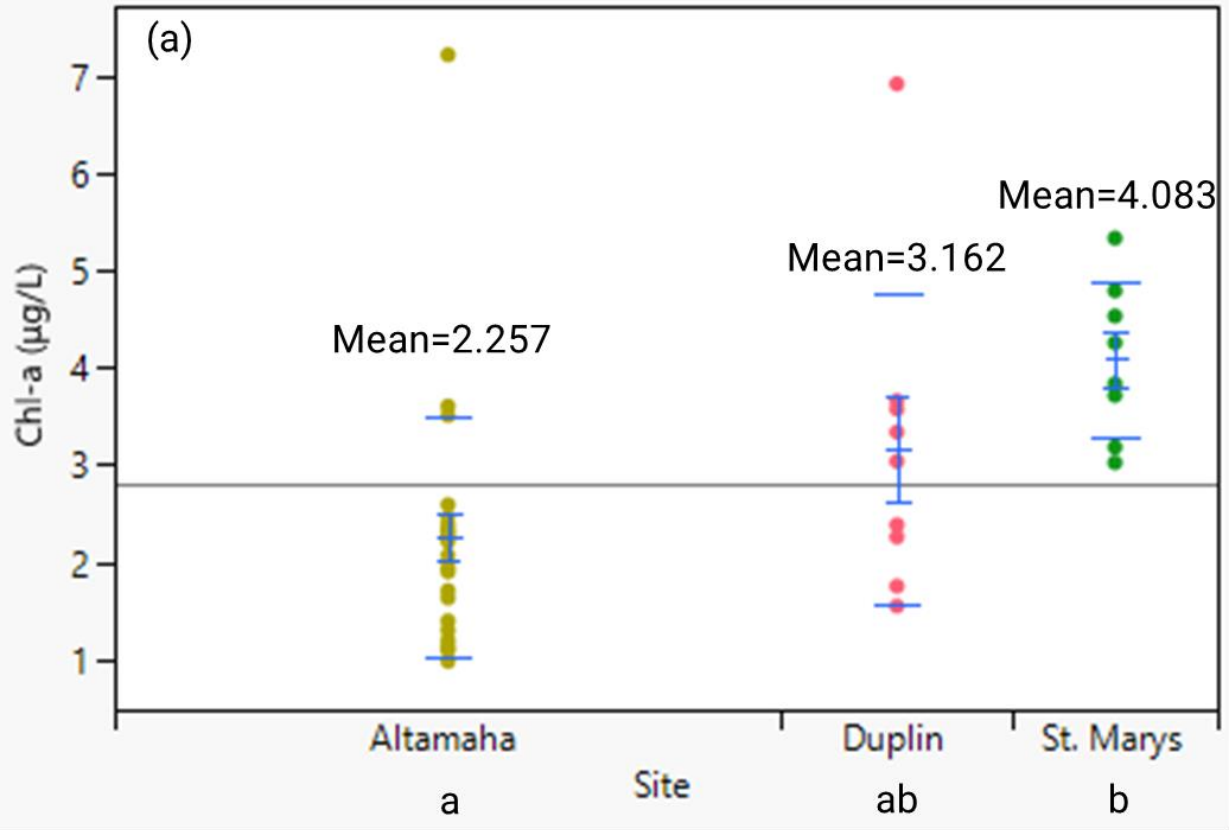
(a)
Chl-a (µg/L)
7
6
5
4
3
2
1
Mean=2.257
Mean=3.162
Mean=4.083
Altamaha
Duplin
St. Marys
Site
a
ab
b

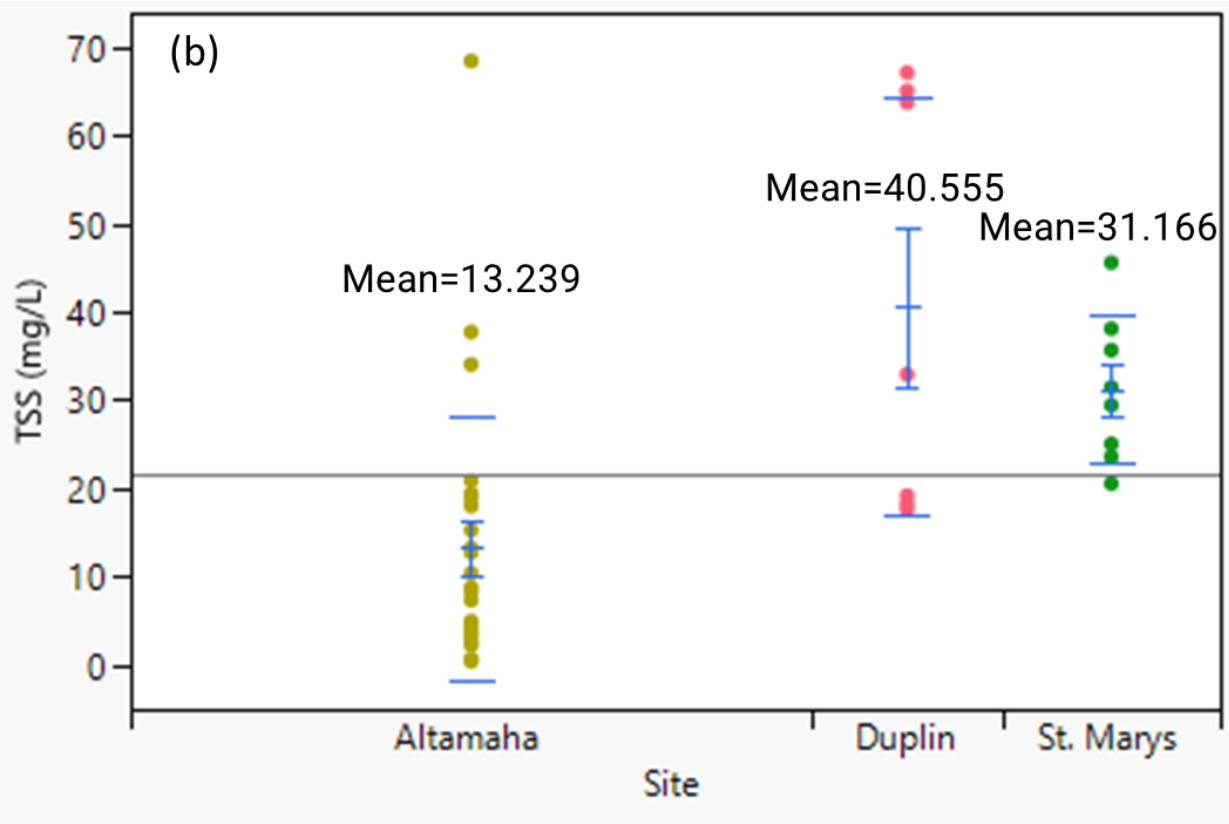
(b)
TSS (mg/L)
70
60
50
40
30
20
10
0
Mean=13.239
Mean=40.555
Mean=31.166
Altamaha
Duplin
St. Marys
Site

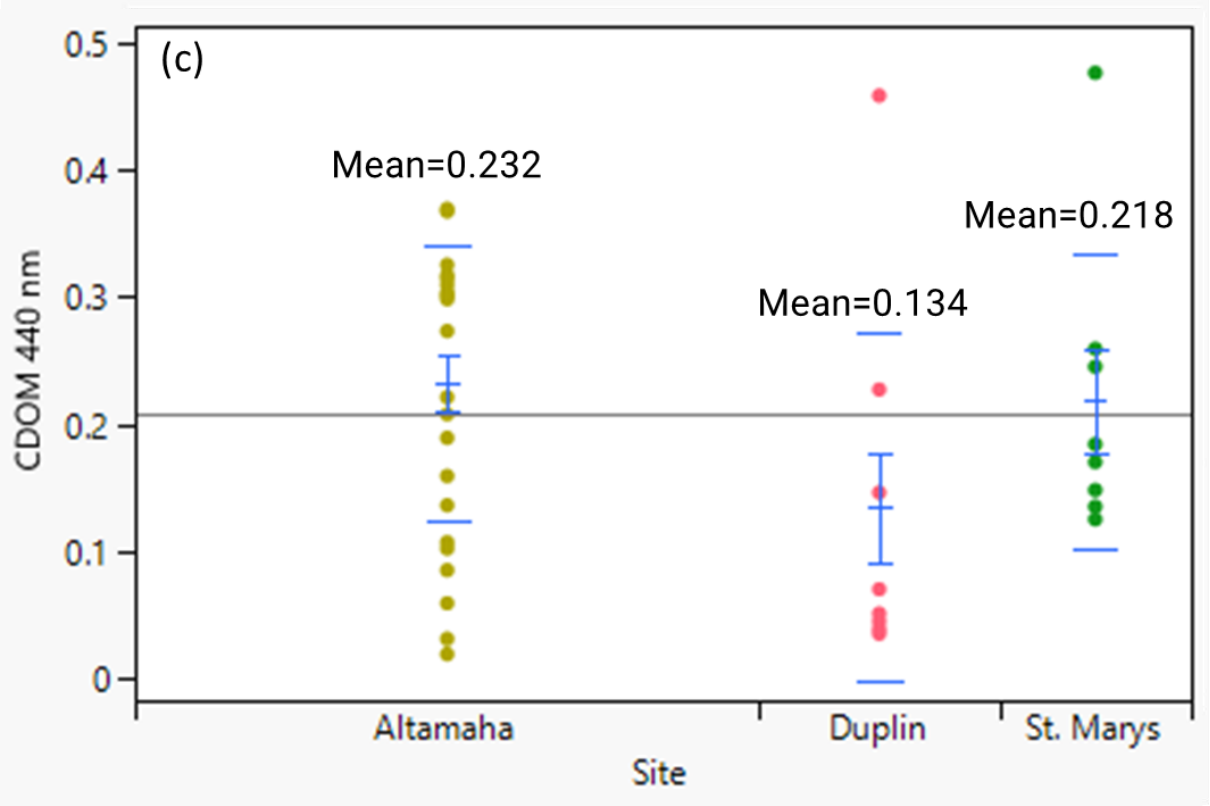

*Figure 3.1a-c: Lab results for Chl-*a *(a), TSS (b), and aCDOM (c) for each site. A Kruskal Wallis H test was conducted to determine if there was site uniqueness before a Steel-Dwass nonparametric test was conducted to determine the specific site uniqueness between study sites. Chl-*a *content (a) between the St Marys site and the Altamaha site was different (*p*=0.008, z=3.634), and TSS content (b) was different between the Altamaha site and the Duplin River site (*p*=0.011, z=2.872), as well as the Altamaha to the St Marys site (*p*=0.002, z=3.340). aCDOM content was not significantly separated by site (*p*=0.056, z=5.783). The* St. *Mary's and Duplin River site lab statistics were not separated based on any parameter.*

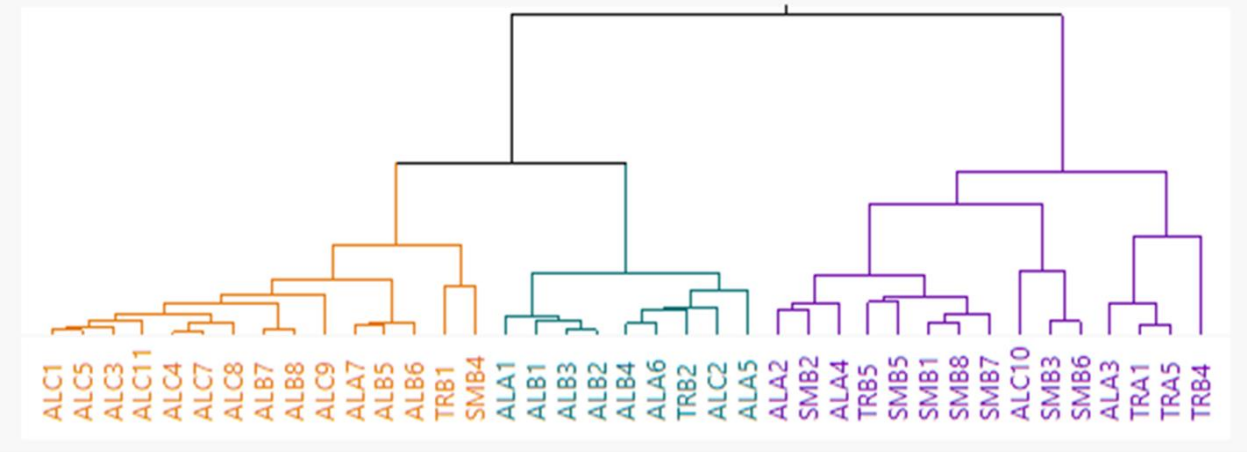

Figure 3.2: Lab Stat Hierarchical Cluster. Hierarchical clusters separating stations by lab characteristics. Chl-a, TSS, and CDOM were all used as variables to determine lab statistic separability. Group colors denote where clusters were separated, with cluster 1 in purple, cluster 2 in orange, and cluster 3 in aqua.

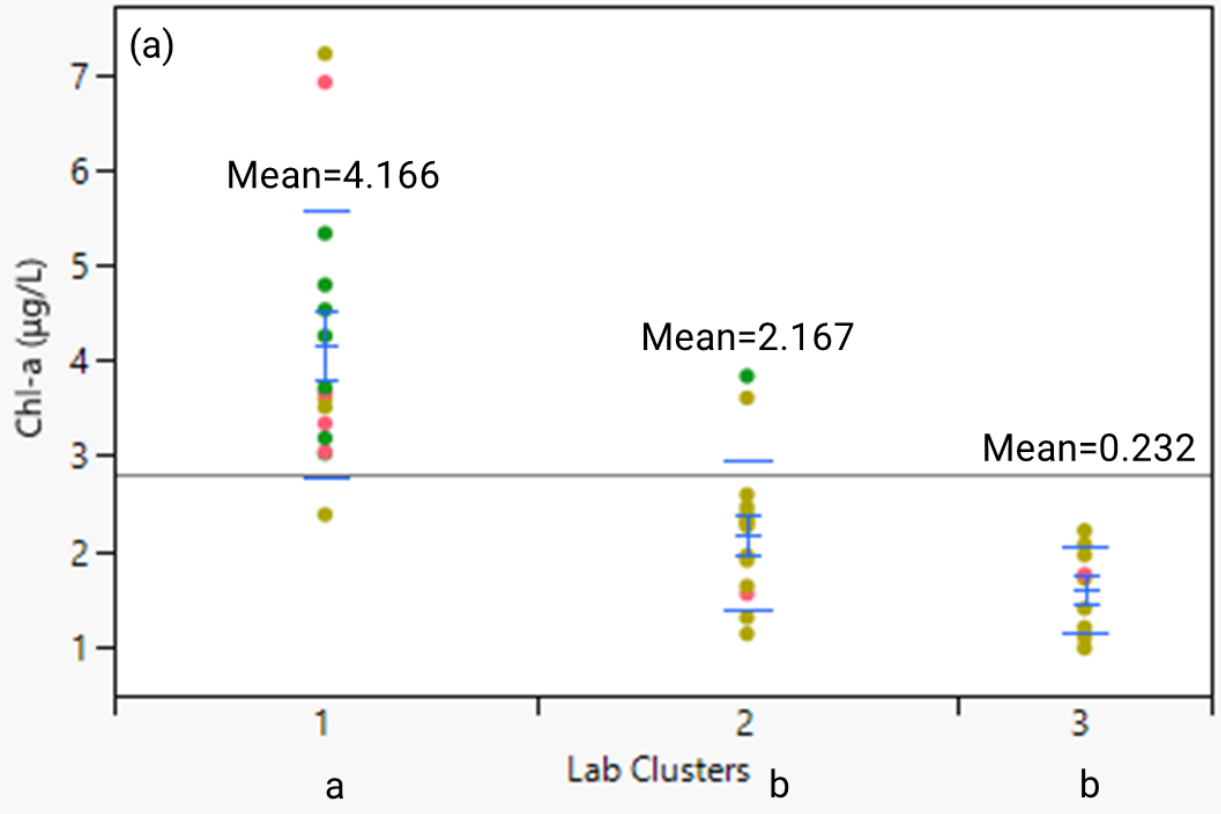
(a)
Chl-a (µg/L)
7
6
5
4
3
2
1
Mean=4.166
Mean=2.167
Mean=0.232
1
2
3
Lab Clusters
a
b
b

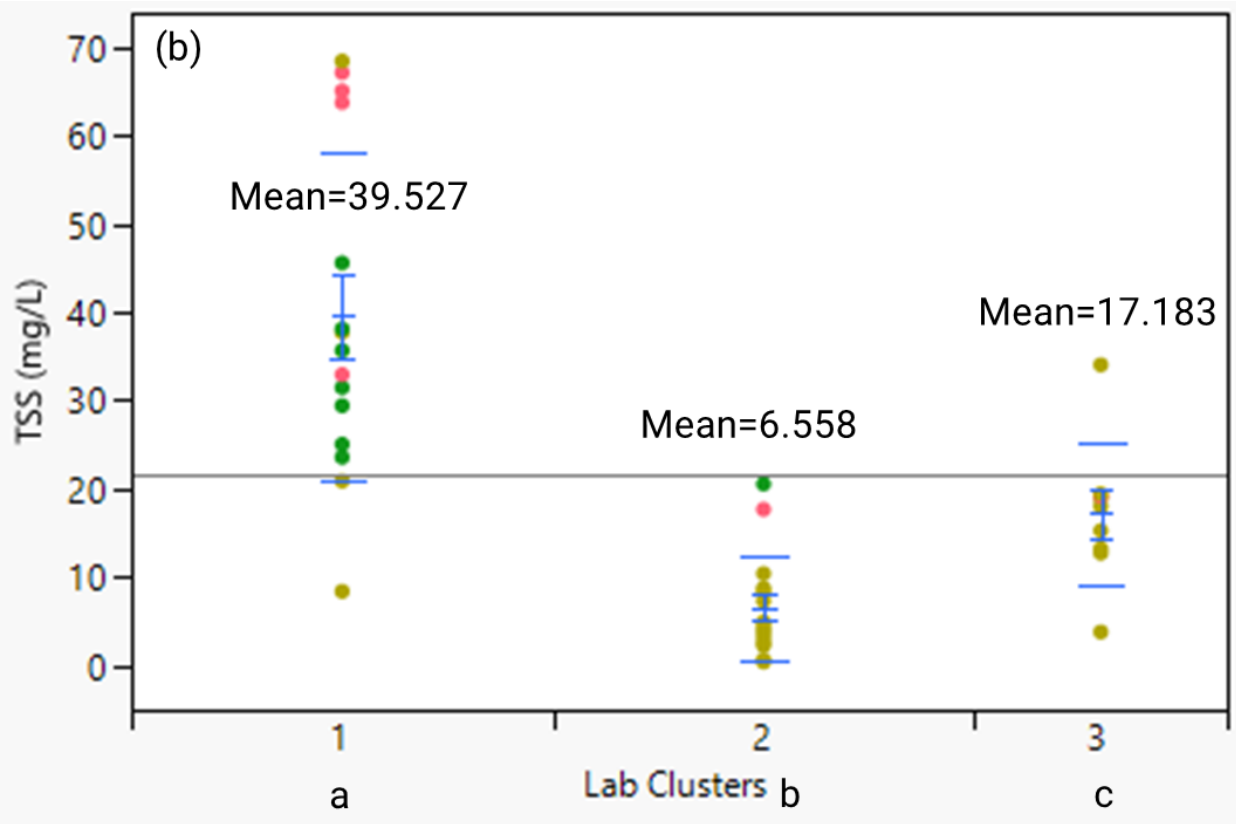
(b)
TSS (mg/L)
70
60
50
40
30
20
10
0
Mean=39.527
Mean=6.558
Mean=17.183
1
2
3
Lab Clusters
a
b
c

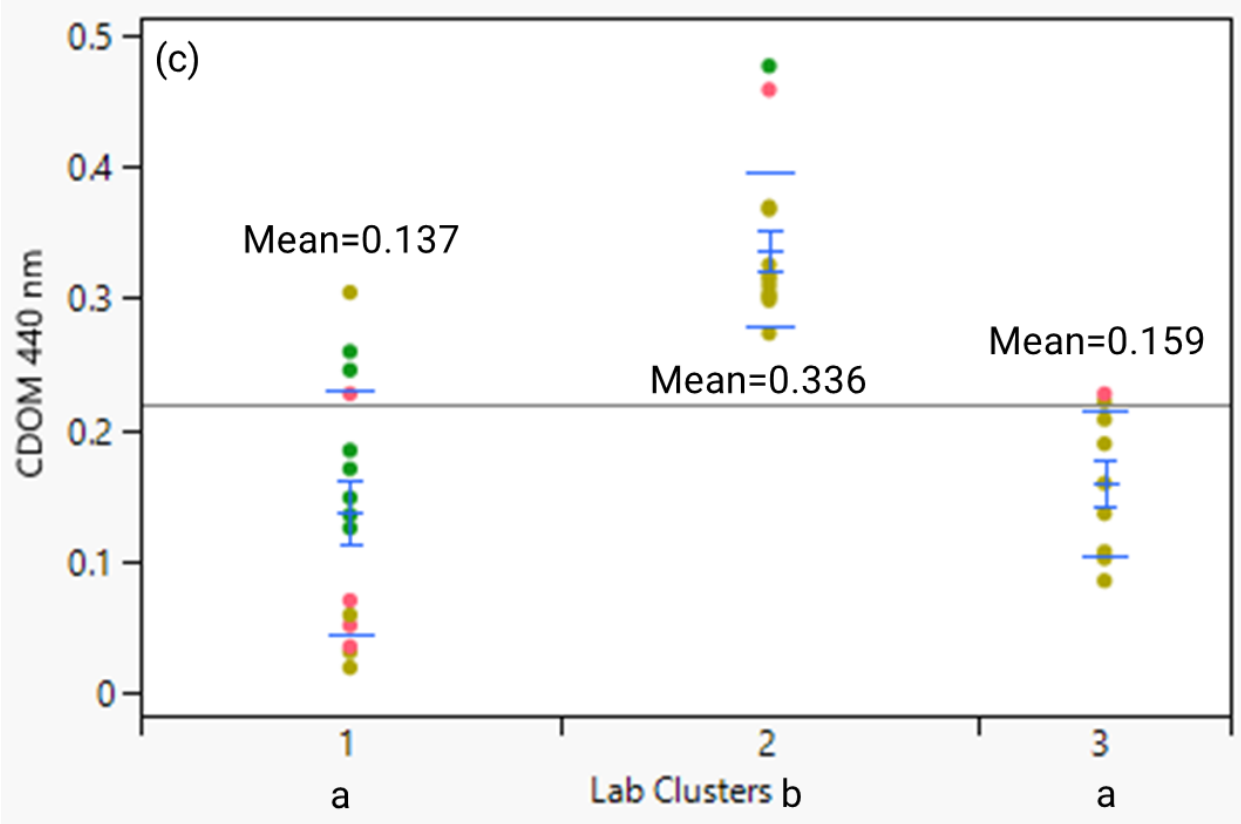

Figure 3.3a-c Lab results for Chl-a (a), TSS (b), and CDOM (c) for each hierarchical cluster as determined by the lab statistics. A Kruskal Wallis test was conducted to determine if there was cluster uniqueness before a Steel-Dwass nonparametric test was conducted to determine the specific cluster uniqueness. Chl-a content (a) was different in cluster 1 from both cluster 2 (p=<0.001, z=3.857) and 3 (p=<0.001, z=3.995), however, no difference was observed between cluster 2 to 3 (p=0.136, z=1.908). TSS was different in all the clusters from each other as follows. Cluster 1 differed from cluster 2 (p=<0.001, z=4.480), cluster 1 differed from cluster 3 (p=0.005, z=-3.160), and cluster 2 from cluster 3 (p=0.012, z=2.862). While CDOM content was not significantly separated from cluster 1 to 3 (p=0.772, z=0.686), CDOM was separable in cluster 1 from 2 (p=<0.001, z=4.439) and cluster 2 from 3 (p=<0.001, z=3.997).

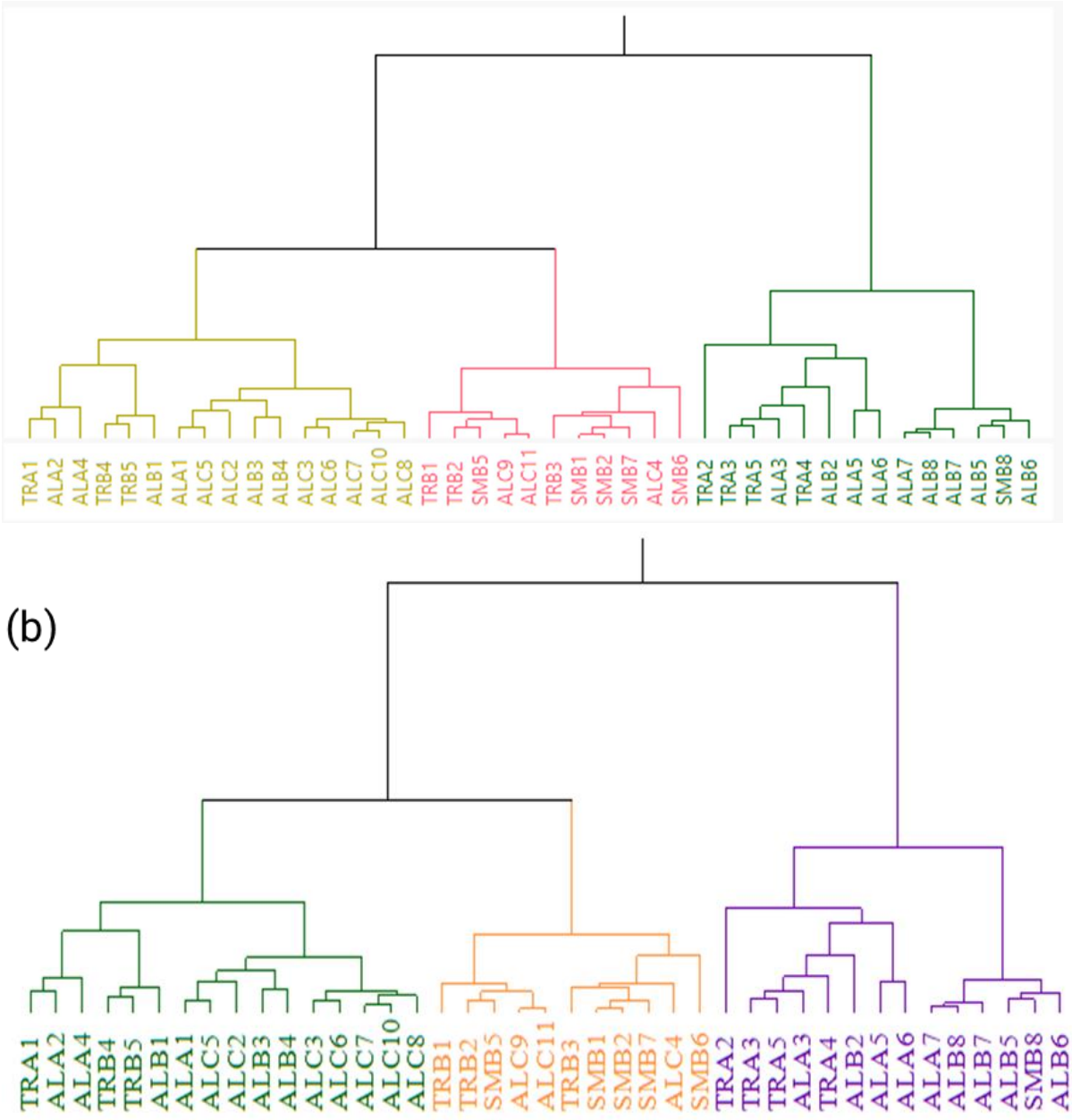

Figure 3.4a Ocean Optics Hierarchical Cluster (above) and Figure 3.4b Resampled Ocean Optics Hierarchical Cluster (below): Hierarchical clusters separating stations by reflectance. Resampled close-range reflectance only utilizing Sentinel-2 satellite bandwidths performed comparable to close-range reflectance including 400-750nm values. Group colors denote where clusters were separated.

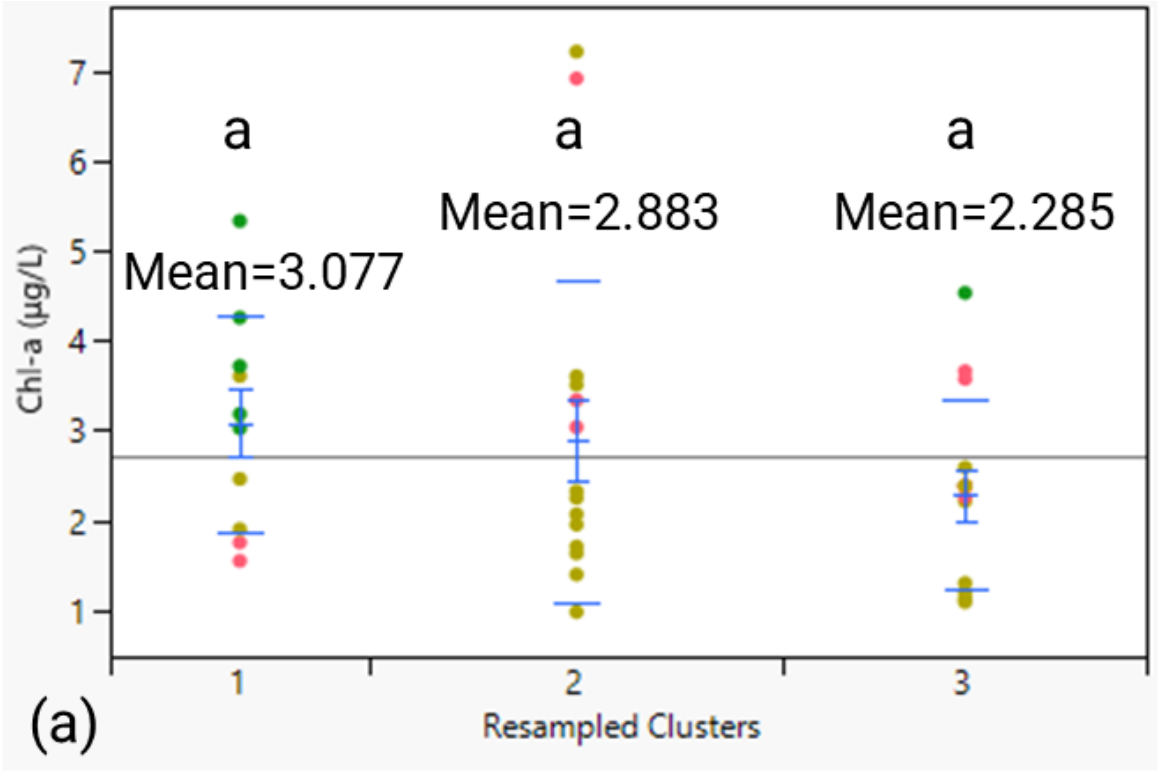
a
a
a
Mean=3.077
Mean=2.883
Mean=2.285
Chl-a (µg/L)
7
6
5
4
3
2
1
1
2
3
Resampled Clusters
(a)

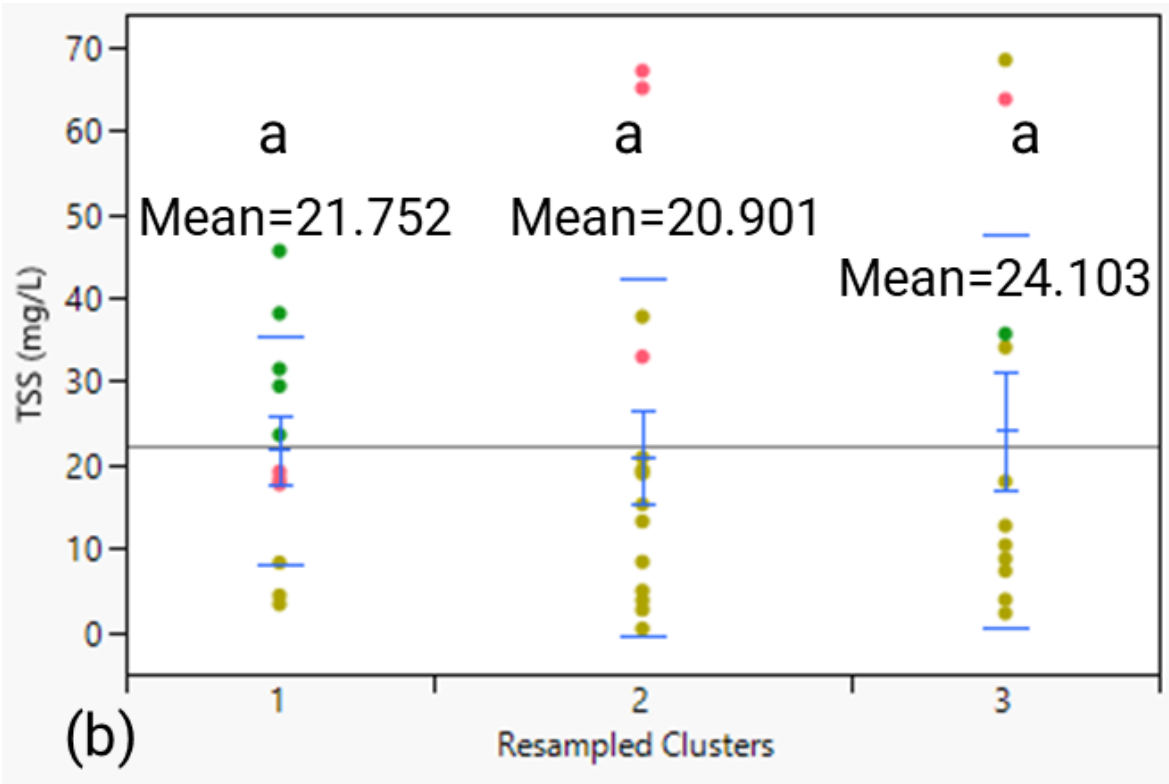
a
a
a
Mean=21.752
Mean=20.901
Mean=24.103
TSS (mg/L)
70
60
50
40
30
20
10
0
1
2
3
Resampled Clusters
(b)

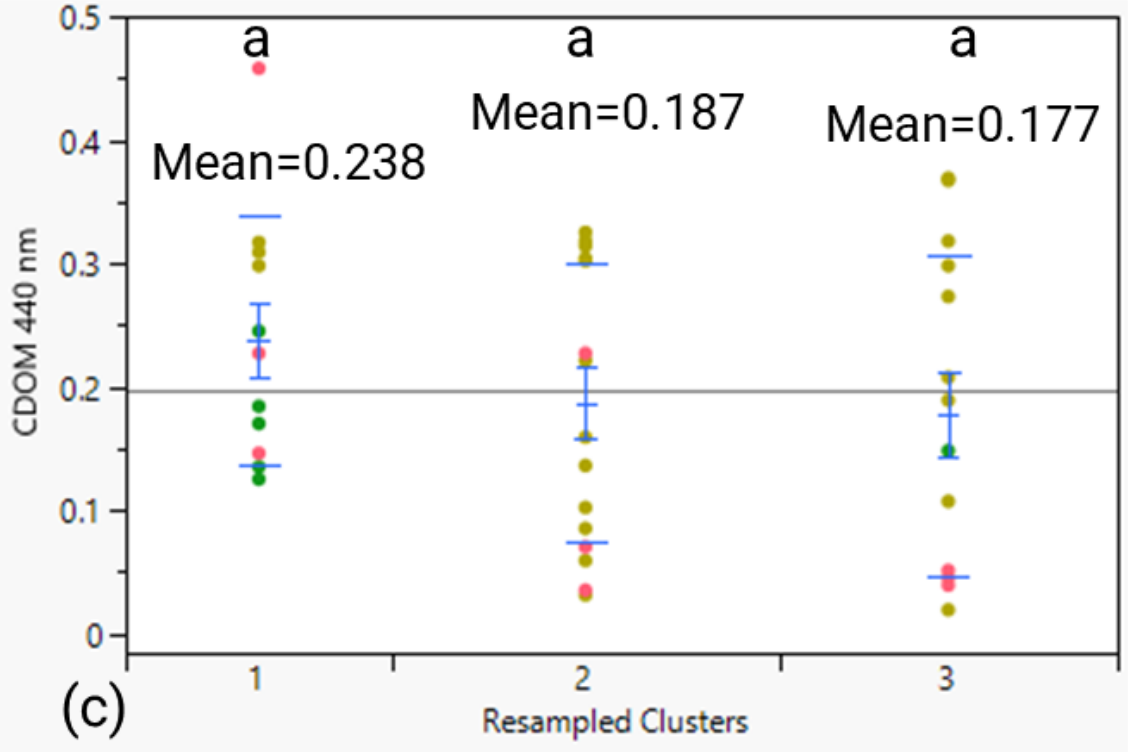

Figure 3.5a-c: Chl-a (a), TSS (b), and CDOM (c) for each hierarchical cluster as determined by resampled close-range reflectance to align with bands utilized by Sentinel-2's MSI. A Kruskal-Wallis test was conducted to determine if there was cluster uniqueness. For all variables, including Chl-a (p=0.358, f=1.057), TSS (p=0.921, f=0.083), and CDOM (p=0.400, f=0.940), there was no uniqueness among the clusters.

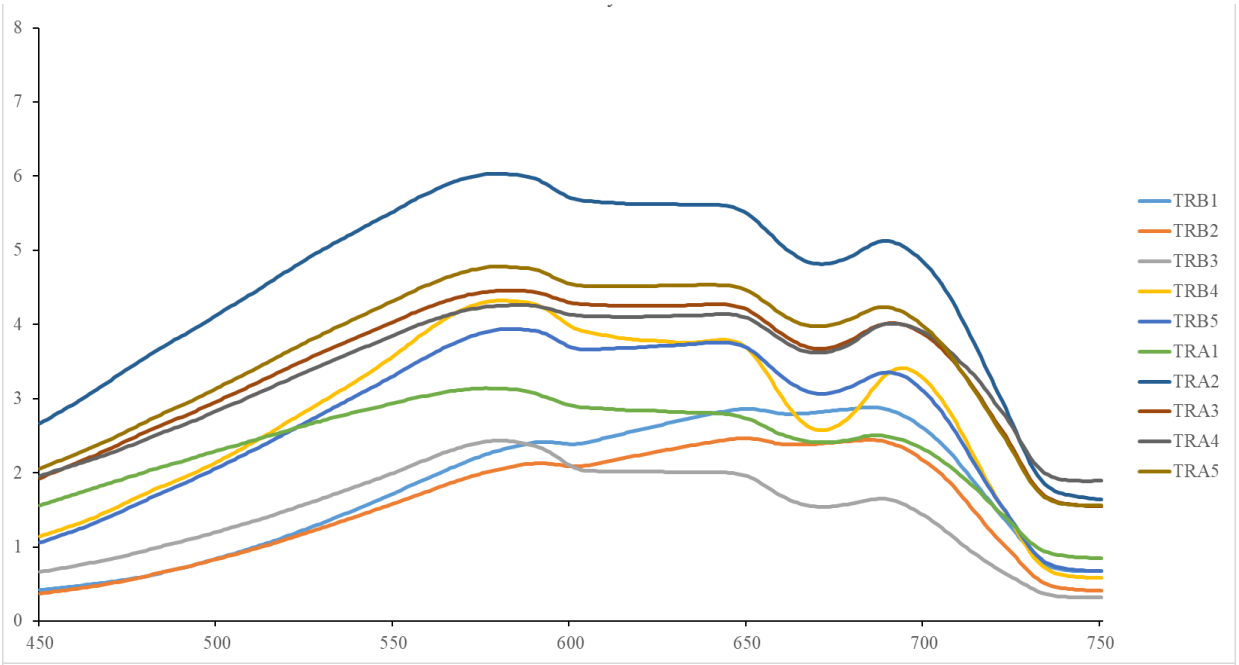
8
7
6
5
4
3
2
1
0
450
500
550
600
650
700
750
TRB1
TRB2
TRB3
TRB4
TRB5
TRA1
TRA2
TRA3
TRA4
TRA5

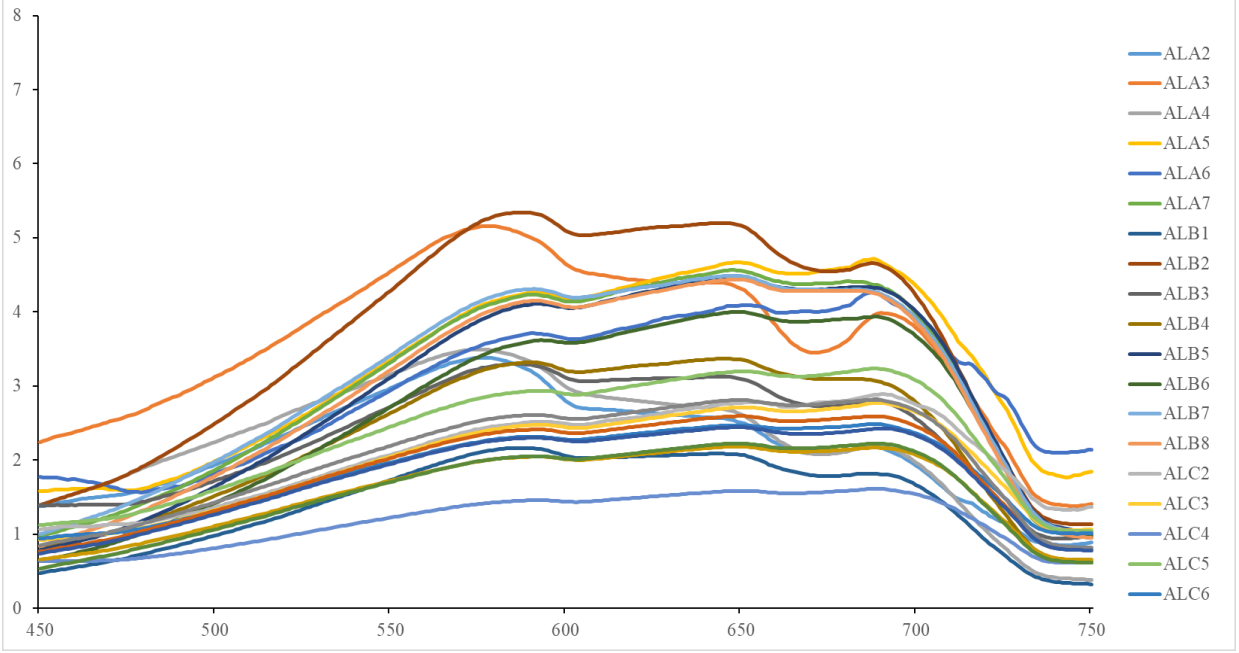
8
7
6
5
4
3
2
1
0
450
500
550
600
650
700
750
ALA2
ALA3
ALA4
ALA5
ALA6
ALA7
ALB1
ALB2
ALB3
ALB4
ALB5
ALB6
ALB7
ALB8
ALC2
ALC3
ALC4
ALC5
ALC6

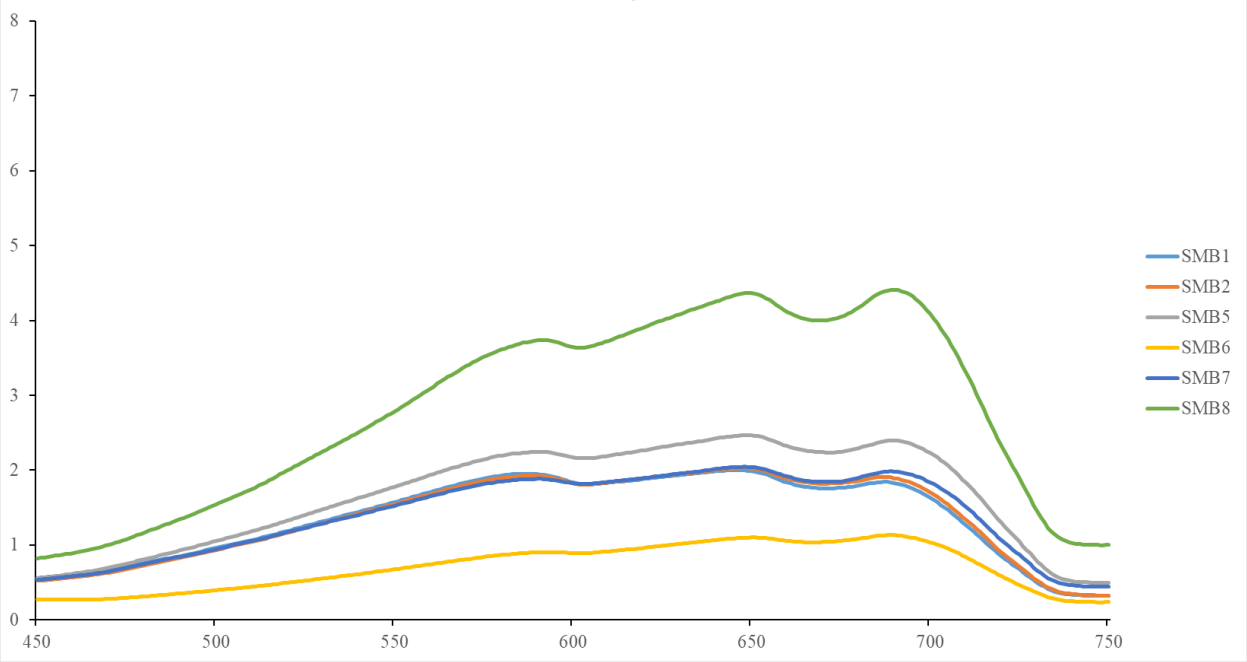

Figure 3.6a-c: Duplin River (a), Altamaha River (b), and St. Marys River (c) close-range hyperspectral reflectance. The y-axis represents reflectance as a percentage, and the x-axis represents wavelength in nanometers (nm).

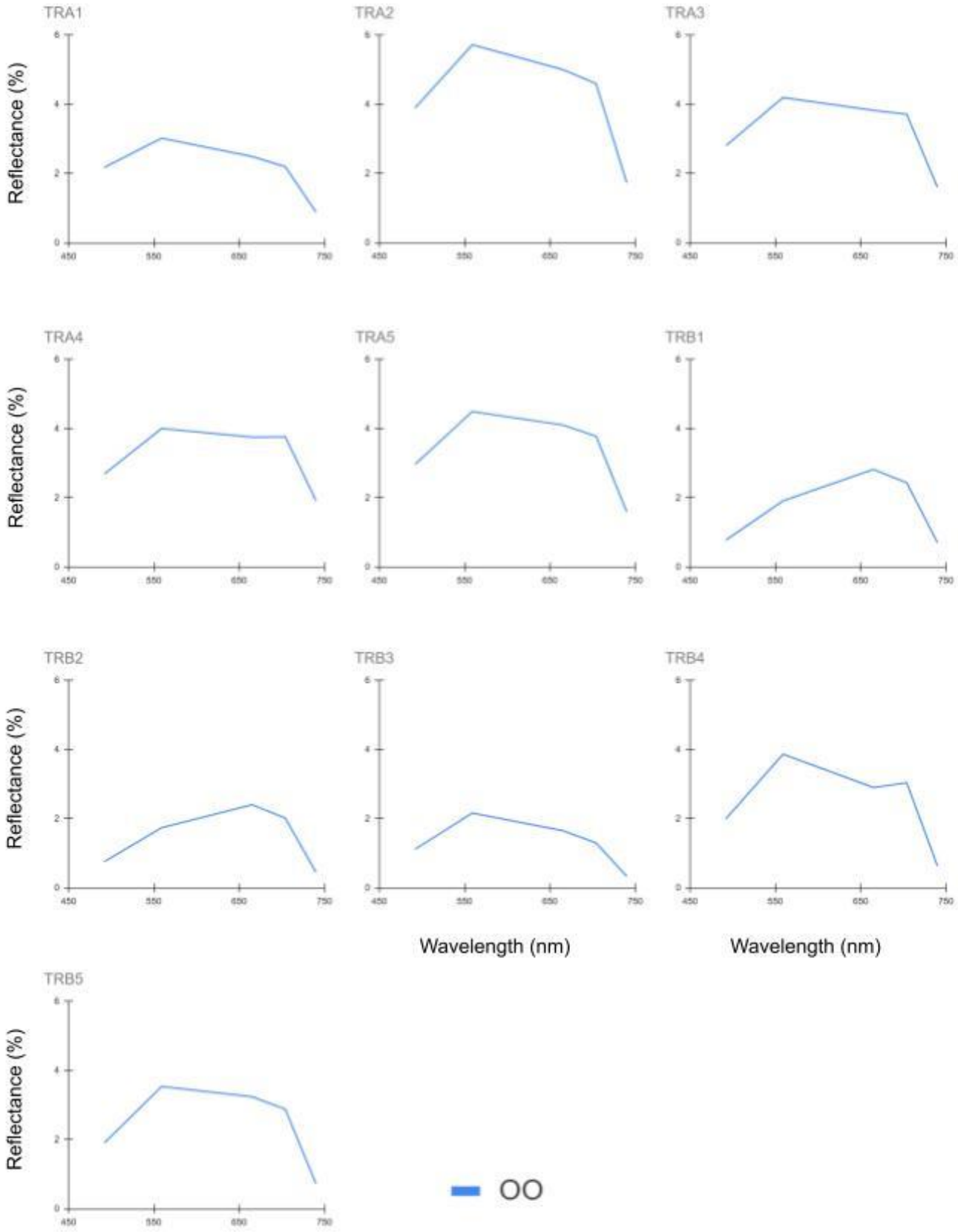

Figure 3.7a: Duplin River stations. Resampled close range reflectance (OO)

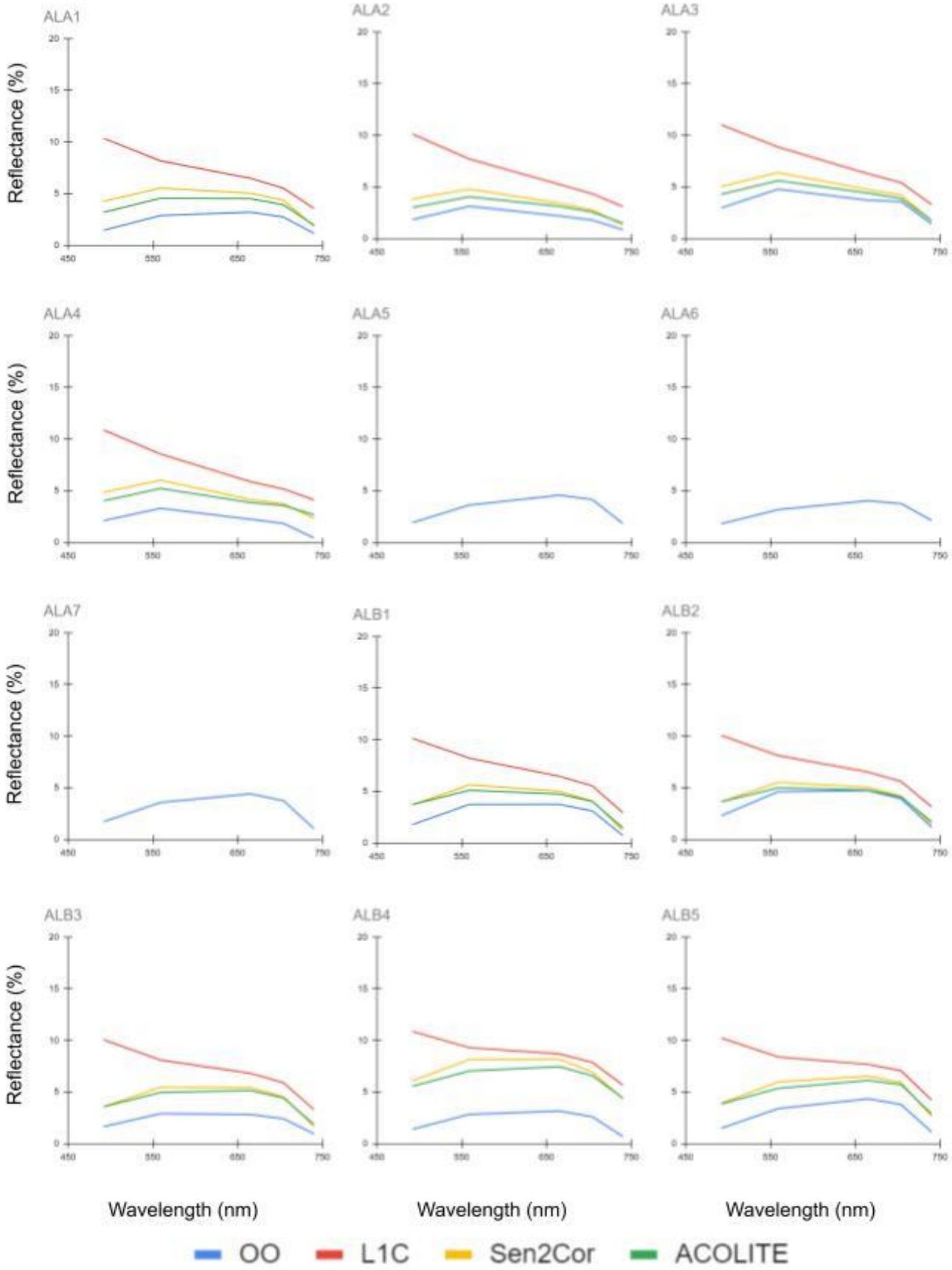

Figure 3.7b: Altamaha River stations. Resampled close range reflectance (OO), atmospherically uncorrected reflectance (L1C), Sen2Cor atmospherically corrected reflectance, and ACOLITE atmospherically corrected reflectance.

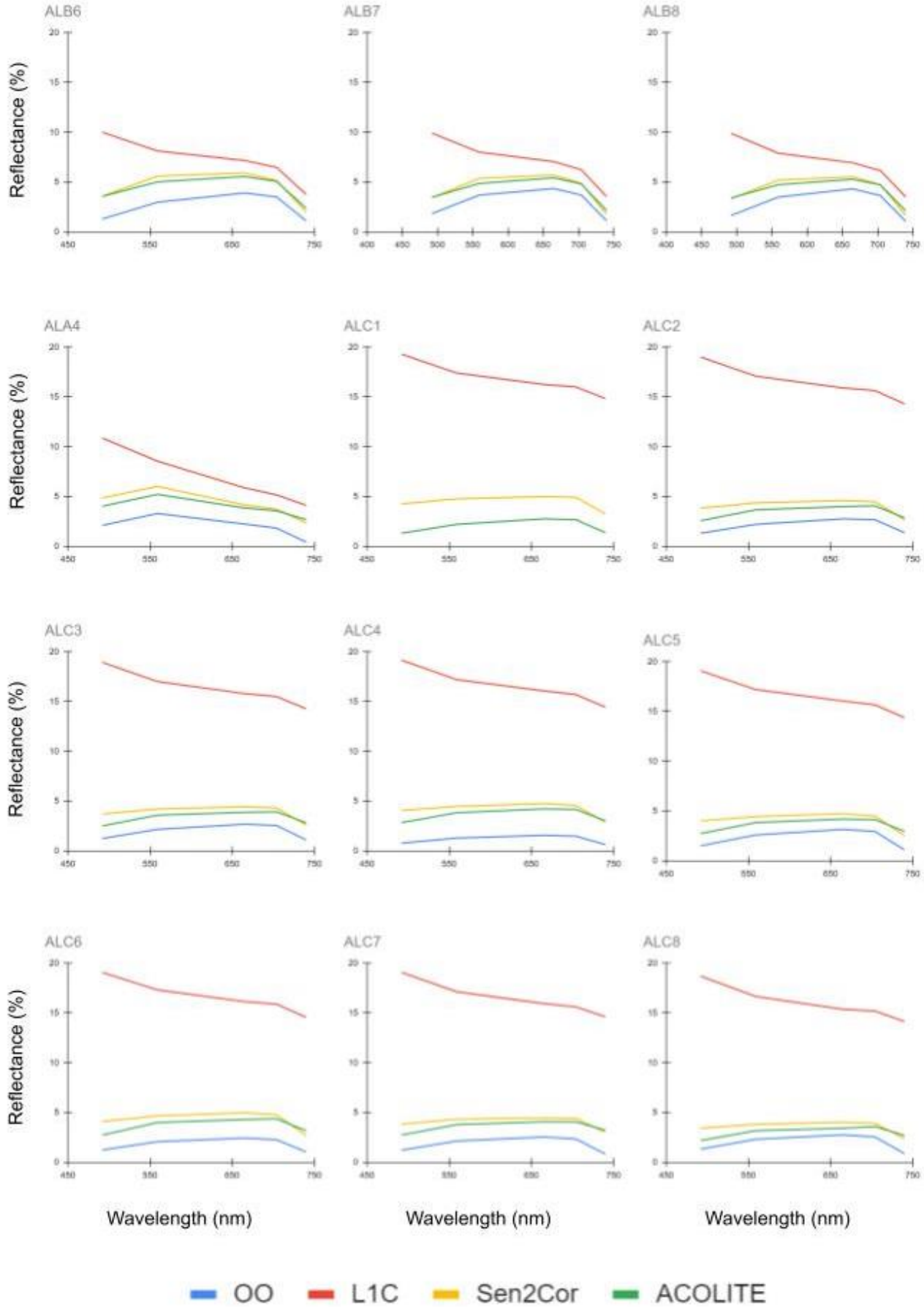

Figure 3.7c: Altamaha River stations. Resampled close range reflectance (OO), atmospherically uncorrected reflectance (L1C), Sen2Cor atmospherically corrected reflectance, and ACOLITE atmospherically corrected reflectance.

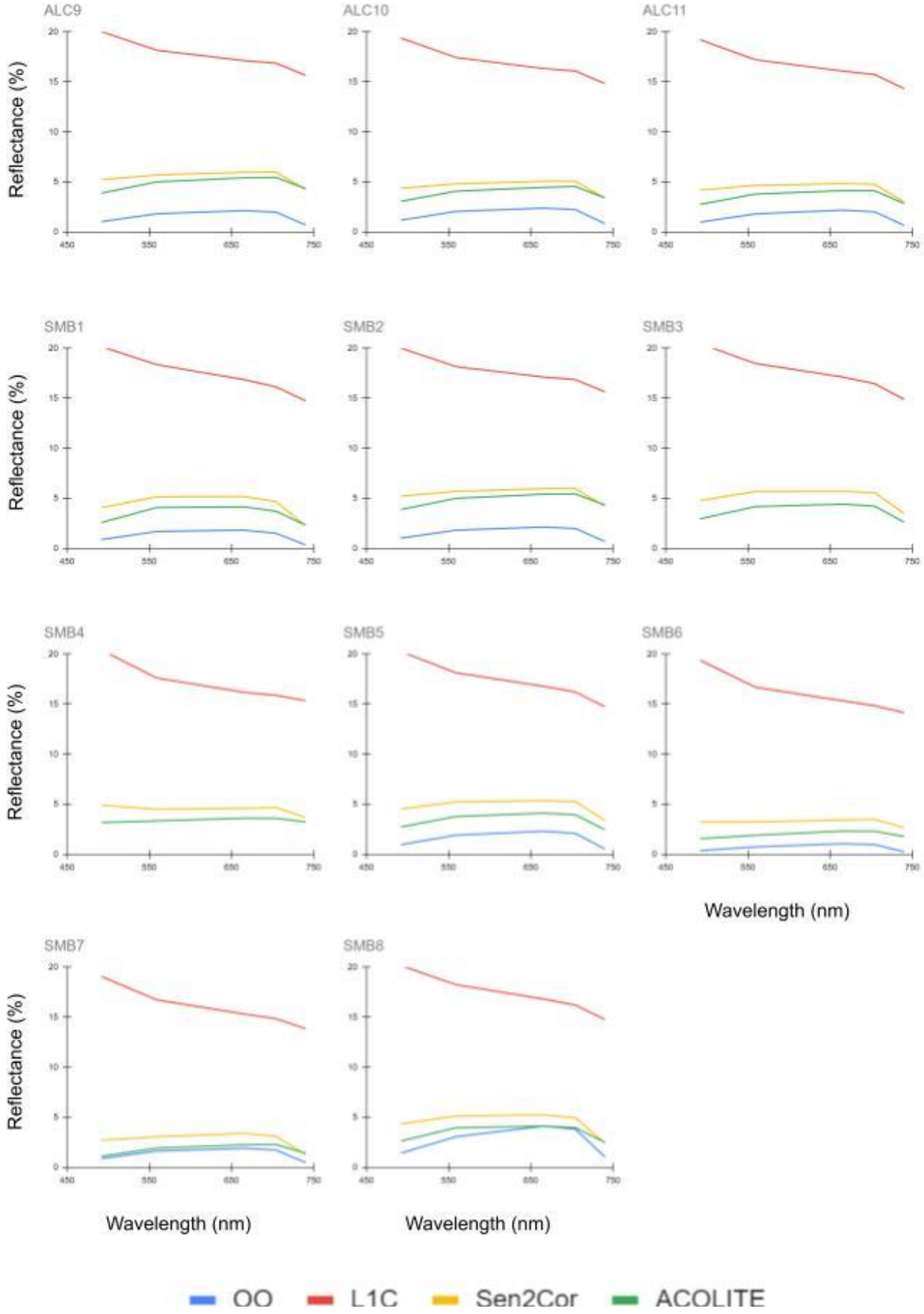

Figure 3.7c: Altamaha and St. Marys River stations. Resampled close range reflectance (OO), atmospherically uncorrected reflectance (L1C), Sen2Cor atmospherically corrected reflectance, and ACOLITE atmospherically corrected reflectance.

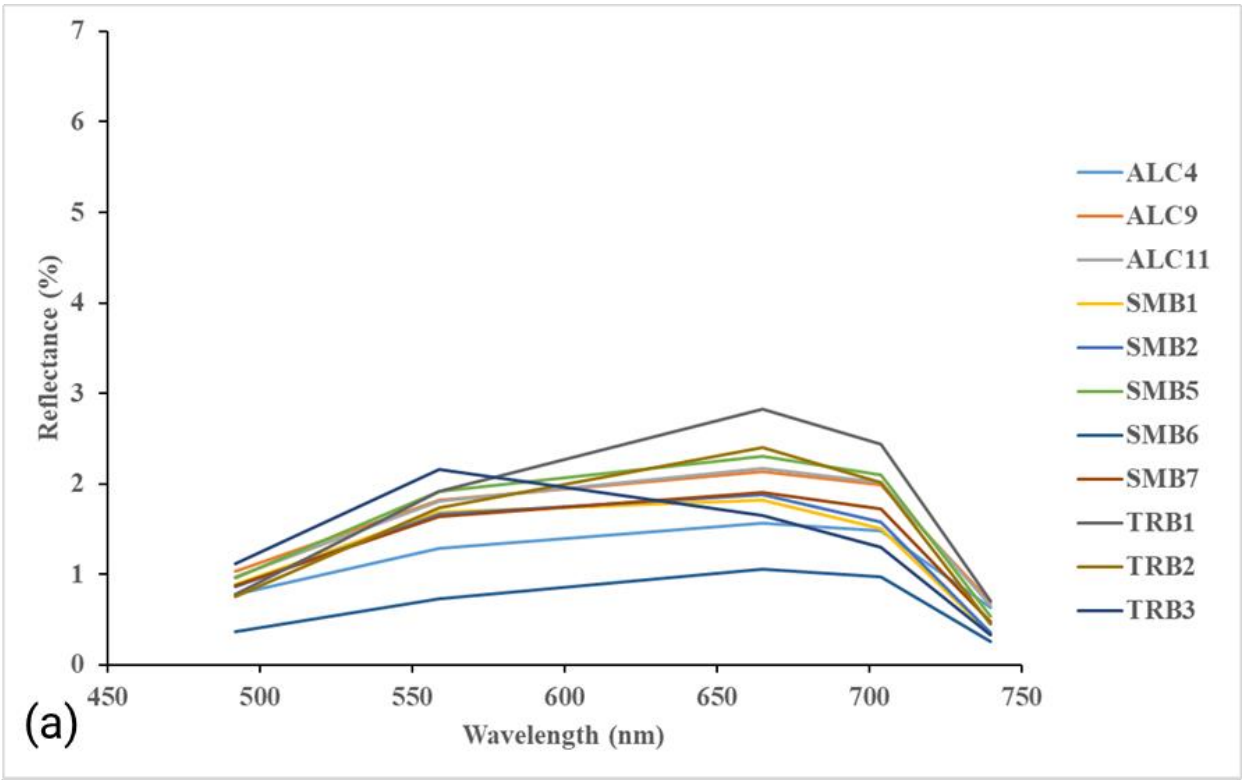
Reflectance (%)
Wavelength (nm)
ALC4
ALC9
ALC11
SMB1
SMB2
SMB5
SMB6
SMB7
TRB1
TRB2
TRB3
(a)

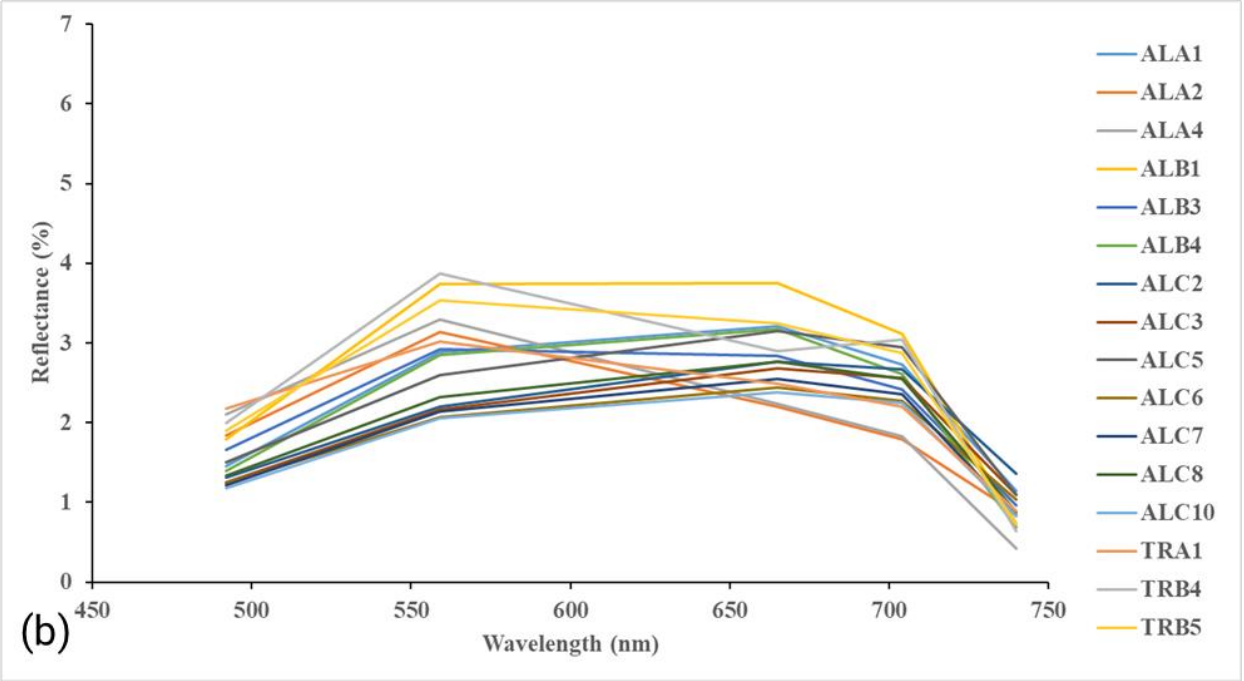
Reflectance (%)
Wavelength (nm)
ALA1
ALA2
ALA4
ALB1
ALB3
ALB4
ALC2
ALC3
ALC5
ALC6
ALC7
ALC8
ALC10
TRA1
TRB4
TRB5
(b)

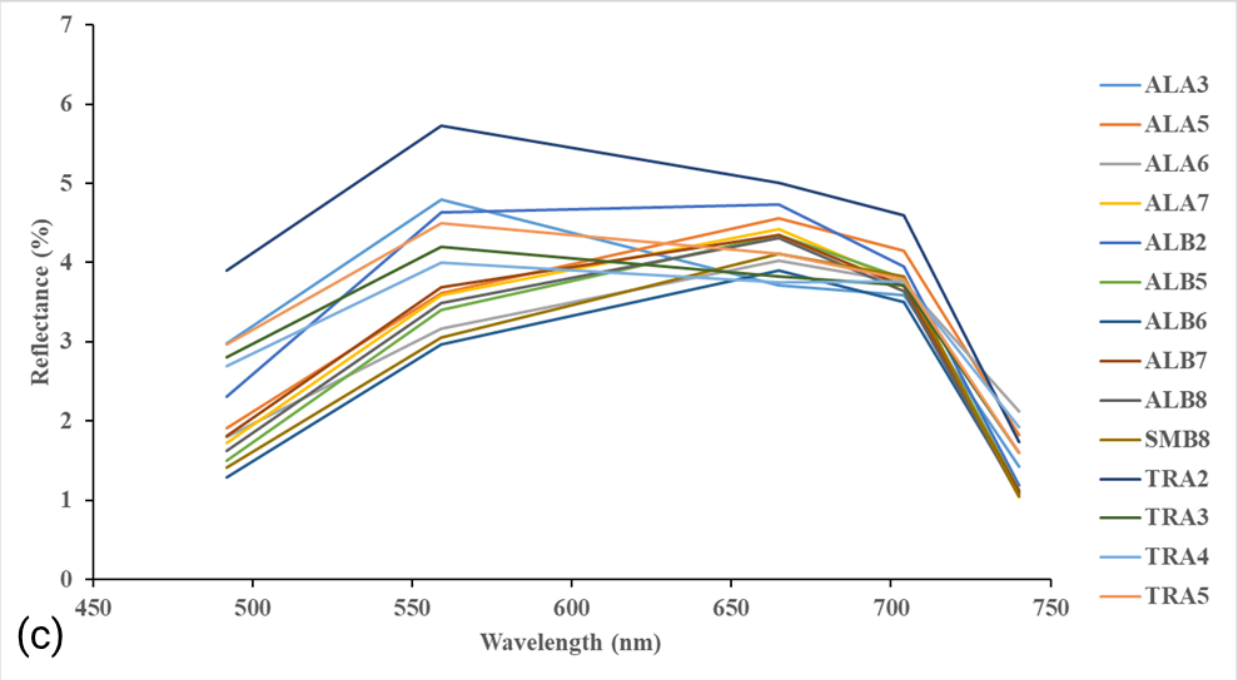

Figure 3.8a-c: Reflectance of Sentinel-2 resampled hierarchical clusters.

Table 3.1: Sampling Conditions. Tidal data was collected from USGS. Precipitation data was collected from the national weather station at the UGA Marine Institute on Sapelo Island for TRA, TRB, ALA, ALB, and ALC, while precipitation was collected from the NOAA weather station located at St. Marys for SMB.

	TRA	**TRB**	**ALA**	**ALB**	**ALC**	**SMB**
Sampling Date	12/4/21	10/30/21	1/8/22	1/23/22	4/8/22	4/23/22
Sampling Time	11:59 am - 1:19 pm	11:35 pm - 2:17 pm	12:05 pm - 3:15 pm	11:30 am - 1:45 pm	10:48 am - 2:27 pm	10:37 am - 1:04 pm
High Tide	**8:48 am (2.07m)** 9:04 pm (1.77m)	**4:55 am (1.46m) 5:15 pm (1.68m)**	1:23 am (1.52m) **1:53 pm (1.55m)**	**11:54 am (1.49m)**	2:47 am (1.49m **3.25 pm (1.28m)**	**7:38 am (1.86m)** 8:02 pm (2.04m)
Low Tide	3:59 am (-0.24m) **4:48 pm (-0.18m)**	12:12 am (0.4m) **12:32 pm (0.34m)**	**8:57 am (0.09 m) 9:29 pm (0.03m)**	**7:21 am (0m) 7:44 pm (0m)**	**10:29 am (0.37m)** 10:41 pm (0.36m)	1:20 am (0.37m) **1:31 pm (0.3m)**
Tidal Effect	Falling tide	Into low tide before rising	Into high tide before falling	High tide into falling	Low tide into rising	Falling into low tide
Mean discharge day before	123.5 m^3 sec^{-1}	249.5 m^3 sec^{-1}	549.3 m^3 sec^{-1}	640 m^3 sec^{-1}	453.1 m^3 sec^{-1}	33.7 m^3 sec^{-1}
Mean Discharge 30 days before	155.2 m^3 sec^{-1}	542.7 m^3 sec^{-1}	267.3 m^3 sec^{-1}	538.6 m^3 sec^{-1}	447.3 m^3 sec^{-1}	39.8 m^3 sec^{-1}
Precipitation previous 30 days	97 mm	80 mm	35 mm	42 mm	223 mm	165 mm
Station count	5	5	7	8	11	8
Satellite Tile	-	-	S2B_T17RMQ	S2A_T17RMQ	S2B_T17RMQ	S2A_T17RMQ

Flyover Time	-	-	11:07 am	11:07 am	11:58 am	11:58 am

Table 3.2: Station location, sampling time and characteristics

Station	Time	Long (DD)	Lat (DD)	Depth (m)	Secchi Depth (m)
TRA1	11:59 AM	81.34033°W	31.44713°N	9.69	0.6
TRA2	12:21 PM	81.32383°W	31.42808°N	8.32	0.57
TRA3	12:39 PM	81.30033°W	31.39416°N	8.96	0.3
TRA4	12:54 PM	81.28583°W	31.37461°N	10.97	0.25
TRA5	1:19 PM	81.29525°W	31.42383°N	4.39	0.55
TRB1	11:35 AM	81.31295°W	31.32418°N	6.86	0.68
TRB2	12:47 PM	81.33171°W	31.37705°N	1.49	0.8
TRB3	1:17 PM	81.30856°W	31.38786°N	5.70	1.3
TRB4	1:43 PM	81.27381°W	31.37641°N	3.96	0.78
TRB5	2:17 PM	81.29470°W	31.42280°N	6.34	0.66

ALA1	12:05 PM	81.41040°W	31.24568°N	5.43	0.65
ALA2	12:26 PM	81.43091°W	31.19421°N	8.90	1
ALA3	12:55 PM	81.42788°W	31.14140°N	8.84	0.7
ALA4	1:28 PM	81.41170°W	31.16920°N	9.02	0.9
ALA5	2:12 PM	81.38445°W	31.27628°N	6.10	0.45
ALA6	2:45 PM	81.42001°W	31.30843°N	3.47	0.5
ALA7	3:15 PM	81.44351°W	31.33961°N	4.05	0.61
ALB1	11:30 AM	81.28596°W	31.32145°N	3.66	0.55
ALB2	11:55 AM	81.31638°W	31.32298°N	5.36	0.65
ALB3	12:17 PM	81.32601°W	31.31923°N	6.10	0.7
ALB4	12:30 PM	81.34473°W	31.31258°N	7.01	0.6
ALB5	12:45 PM	81.36888°W	31.32011°N	5.52	-

ALB6	12:56 PM	81.38541°W	31.31710°N	6.55	-
ALB7	1:31 PM	81.39470°W	31.30476°N	5.64	-
ALB8	1:45 PM	81.41245°W	31.30766°N	9.14	-
ALC1	10:48 AM	81.45171°W	31.32645°N	6.46	0.46
ALC2	11:21 AM	81.46227°W	31.33362°N	6.00	0.49
ALC3	11:29 AM	81.47025°W	31.33448°N	8.32	0.51
ALC4	11:38 AM	81.47823°W	31.34529°N	2.35	0.49
ALC5	11:49 AM	81.48428°W	31.36516°N	5.52	0.46
ALC6	12:02 PM	81.49366°W	31.37678°N	1.19	0.46
ALC7	1:12 PM	81.47675°W	31.36316°N	1.55	0.4
ALC8	1:27 PM	81.47452°W	31.37046°N	1.37	0.57
ALC9	1:48 PM	81.46246°W	31.36633°N	1.28	0.6

ALC10	2:11 PM	81.45057°W	31.35611°N	1.46	0.57
ALC11	2:27 PM	81.44015°W	31.34827°N	4.27	0.43
SMB1	10:37 AM	81.44702°W	30.70586°N	9.02	1.07
SMB2	10:56 AM	81.47980°W	30.72440°N	7.68	1.01
SMB3	11:12 AM	81.50925°W	30.72244°N	8.96	0.91
SMB4	11:50 AM	81.48520°W	30.73257°N	6.07	0.82
SMB5	12:12 PM	81.48288°W	30.75233°N	11.70	0.7
SMB6	12:30 PM	81.47297°W	30.76197°N	10.73	0.82
SMB7	12:51 PM	81.47114°W	30.77302°N	5.79	0.73
SMB8	1:04 PM	81.46929°W	30.70931°N	3.51	0.73

Table 3.3: Matchup Summary Information

Station	Close-range Reflectance	Satellite Reflectance	Matchup	Lab Data
TRA1	Yes	Removed, Cirrus	No	Yes
TRA2	Yes	Removed, Cirrus	No	TSS removed, outlier
TRA3	Yes	Removed, Cirrus	No	TSS removed, outlier
TRA4	Yes	Removed, Cirrus	No	TSS removed, outlier
TRA5	Yes	Removed, Cirrus	No	Yes
TRB1	Yes	Removed, Clouds	No	Yes
TRB2	Yes	Removed, Clouds	No	Yes
TRB3	Yes	Removed, Clouds	No	Chl-a removed, outlier
TRB4	Yes	Removed, Clouds	No	Yes
TRB5	Yes	Removed, Clouds	No	Yes
ALA1	Yes	Yes	Yes	Yes
ALA2	Yes	Yes	Yes	Yes
ALA3	Yes	Yes	Yes	Yes
ALA4	Yes	Yes, Light Cirrus	Yes	Yes

ALA5	Yes	Removed. Shadow	No	Yes
ALA6	Yes	Removed, Cloud	No	TSS removed, lab error
ALA7	Yes	Removed, Shadow	No	Yes
ALB1	Yes	Yes	Yes	Yes
ALB2	Yes	Yes	Yes	Yes
ALB3	Yes	Yes	Yes	Yes
ALB4	Yes	Yes	Yes	Yes
ALB5	Yes	Yes	Yes	Yes
ALB6	Yes	Yes	Yes	Yes
ALB7	Yes	Yes	Yes	Yes
ALB8	Yes	Yes	Yes	Yes
ALC1	Removed, recording error	Yes	No	Yes
ALC2	Yes	Yes	Yes	Yes
ALC3	Yes	Yes	Yes	Yes
ALC4	Yes	Yes	Yes	Yes
ALC5	Yes	Yes	Yes	Yes
ALC6	Yes	Yes	Yes	Yes
ALC7	Yes	Yes	Yes	Yes
ALC8	Yes	Yes	Yes	Yes
ALC9	Yes	Yes	Yes	Yes

ALC10	Yes	Yes	Yes	Chl-a removed, outlier
ALC11	Yes	Yes	Yes	Yes
SMB1	Yes	Yes	Yes	Yes
SMB2	Yes	Yes	Yes	Yes
SMB3	Removed, recording error	Yes	No	Yes
SMB4	Removed, recording error	Yes	No	Yes
SMB5	Yes	Yes	Yes	Yes
SMB6	Yes	Yes	Yes	Yes
SMB7	Yes	Yes	Yes	Yes
SMB8	Yes	Yes	Yes	Yes
Total N Matchups	41/44	31/44	28/44	43/44 Chl-a 40/44 TSS 44/44 CDOM

Table 3.4: Lab measurements

	Chl-a	**TSS**	**CDOM 440**

	(µg/L)	(mg/L)	nm (m-1)
TRA1	3.337	65.026	0.07
TRA2	3.572	89.941*	0.045
TRA3	2.257	107.742*	0.045
TRA4	2.382	97.826*	0.039
TRA5	3.66	63.7	0.051
TRB1	1.546	17.681	0.458
TRB2	1.751	19.194	0.227
TRB3	20.462*	18.279	0.146
TRB4	6.918	67.088	0.035
TRB5	3.036	32.917	0.227
ALA1	1.956	13.24	0.136
ALA2	3.506	20.889	0.059
ALA3	2.38	68.396	0.019
ALA4	3.602	37.71	0.031
ALA5	1.088	34.031	0.208
ALA6	1.195	12.716	0.189
ALA7	1.299	8.765	0.273
ALB1	1.706	19.426	0.085
ALB2	2.212	18.014	0.107
ALB3	2.066	18.958	0.102
ALB4	0.978	15.265	0.159
ALB5	1.128	10.403	0.298

ALB6	1.306	7.322	0.318
ALB7	2.385	2.267	0.367
ALB8	2.589	3.873	0.369
ALC1	2.297	0.686	0.301
ALC2	1.395	3.8	0.221
ALC3	2.323	2.669	0.325
ALC4	1.9	4.381	0.317
ALC5	2.257	2.786	0.303
ALC6	2.246	*	0.302
ALC7	1.951	4.943	0.318
ALC8	1.629	0.405	0.314
ALC9	3.604	3.333	0.309
ALC10	7.217	8.399	0.304
ALC11	2.458	8.309	0.298
SMB1	4.254	31.456	0.17
SMB2	3.023	29.412	0.125
SMB3	4.791	25.033	0.259
SMB4	3.833	20.552	0.479
SMB5	3.182	45.558	0.135
SMB6	5.332	23.577	0.245
SMB7	3.715	38.095	0.184
SMB8	4.53	35.648	0.148

Table 3.5: Lab data summary

Site	**Chl-a (µg/L)**	**SD**	**SE**	**N**	**Group**
Altamaha Rivers	2.257	1.249	0.25	26	a
Duplin River	3.162	1.605	0.54	9	ab
St. **Marys River**	4.083	0.795	0.28	8	b
Overall	2.786	1.431	0.22	43	
	TSS (mg/L)				
Altamaha	13.239	15.04	3.01	25	a
Duplin River	40.555	23.71	8.96	7	b
St. **Marys**	31.166	8.335	2.95	8	b
Overall	21.605	19.14	3.03	40	
	aCDOM 440 nm (m^{-1})				
Altamaha River	0.232	0.109	0.02	26	a
Duplin River	0.1343	0.137	0.04	10	a
St. **Marys River**	0.2178	0.115	0.04	8	a
Overall	0.207	0.018	0.12	44	

*Table 3.6: Constituent Correlation matrix and calculated p-value. An * denotes a significant p-value with either a positive or negative correlation..*

	Chl-*a*	**TSS**	**CDOM (440)**
TSS	0.377* (*p*=0.016)	1	1
CDOM (440)	-0.181 (*p*=0.252)	-0.706* (*p*=<0.001)	1
Secchi (m)	0.449* (*p*=0.004)	0.186 (*p*=0.25)	-0.161 (*p*=0.32)

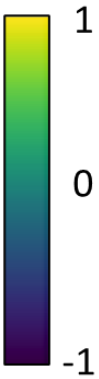

Table 3.7: Lab Cluster data summary (based on Figure 3.1).

Lab Cluster	**Chl-a (µg/L)**	**SD**	**SE**	**N**	**Group**
1	4.166	1.399	0.361	15	a
2	2.167	0.782	0.202	15	b
3	1.594	0.448	0.149	9	b
	TSS (mg/L)				
1	39.527	18.663	4.819	15	a
2	6.558	5.904	1.524	15	b
3	17.183	8.024	2.675	9	c
	aCDOM 440 nm (m^{-1})				
1	0.137	0.924	0.024	15	a
2	0.336	0.059	0.015	15	b
3	0.159	0.054	0.018	9	a

Table 3.8:Close-range reflectance resampled hierarchical cluster data summary.

OO Resampled Hierarchical Cluster	**Chl-a (µg/L)**	**SD**	**SE**	**N**	**Group**
1	3.077	1.204	0.381	10	a
2	2.883	1.798	0.45	16	a
3	2.285	1.06	0.283	14	a
	TSS (g)				
1	21.752	13.59	4.098	11	a
2	20.901	21.36	5.515	15	a
3	24.103	23.493	7.083	11	a
	CDOM (440 nm)				
1	0.238	0.101	0.031	11	a
2	0.187	0.114	0.028	16	a
3	0.177	0.13	0.035	14	a

Table 3.9: Regression analysis of close-range reflectance against Satellite reflectance by band.

Processor	**Band**	**Central Wavelength**	**N**	**R^2**	***p*-value**	**RMSD**	**MAPD (ψ)**	**Slope**	**Intercept**
L1C	Band 2	492	28	**0.494**	<0.001	3.362	1310.386	-6.22	24.197
	Band 3	559	28	**0.624**	<0.001	2.905	567.609	-3.82	23.49
	Band 4	665	28	**0.349**	<0.001	3.953	413.852	-2.94	20.618
	Band 5	704	28	**0.241**	0.008	4.446	443.768	-2.96	19.132
	Band 6	740	28	**0.145**	0.046	5.183	1433.319	-6.64	15.587
Sen2Cor	Band 2	492	28	0.026	0.417	0.7	232.47	0.212	3.77
	Band 3	559	28	**0.299**	0.003	0.857	116.485	0.572	3.606
	Band 4	665	28	**0.192**	0.02	0.899	91.054	0.446	3.748
	Band 5	704	28	**0.061**	<0.001	0.846	99.183	0.255	3.964
	Band 6	740	28	0.1	0.101	0.799	258.918	-0.83	3.181
ACOLITE	Band 2	492	28	**0.33**	0.001	0.717	138.167	0.941	1.801
	Band 3	559	28	**0.428**	<0.001	0.807	78.097	0.713	2.438
	Band 4	665	28	**0.319**	0.002	0.888	65.092	0.619	2.647

	Band 5	704	28	**0.215**	0.013	0.825	74.882	0.51	2.847
	Band 6	740	28	0.002	0.813	0.782	247.744	-0.11	2.638

CHAPTER 4

DISCUSSION

4.0 Introduction

This project had two main objectives: to characterize three study sites and individual stations along the Georgia coast into optical water types based on bulk water sample analysis of Chl-*a*, TSS, and CDOM and close-range remote sensing hyperspectral data (objective 1) and perform an analysis of the accuracy of Sen2Cor and ACOLITE atmospheric correction processors compared to *in situ* data was conducted through statistical analysis (objective 2). To accomplish these, the relationship between water quality OACs, close-range hyperspectral data, and atmospheric correction methods for satellite remote sensing imagery were examined. Field sampling was conducted in three coastal Georgia rivers (Figure 2.2a) where *in situ* bulk water samples (Table 3.4) and close-range hyperspectral reflectance were collected to coincide with Sentinel-2 MSI satellite flyover times (Figure 3.6a-c, figure 3.7a-d). Bulk water samples were then processed for Chl-*a*, TSS, and CDOM absorption through laboratory-based techniques for statistical analysis. Sentinel-2 MSI imagery was downloaded and atmospherically corrected utilizing Sen2Cor and ACOLITE atmospheric correction packages. Statistical analysis techniques were implemented for the classification of optical water type for each station and site, and atmospheric correction performance was determined (Figure 1).

The main findings of this project are: bulk water samples were effective at separating stations by optical water type, and more studies could use this method to explore the performance of retrieval algorithms by hierarchical cluster instead of by site; using close-range hyperspectral reflectance to determine optical water type was inconclusive, and more emphasis

should be placed in retrieval algorithms and band ratios to separate stations by cluster; the performance of both ACOLITE and Sen2Cor was comparable along the Georgia coastline. Future work could focus on using hyperspectral close-range reflectance, and satellite reflectance to predict OACs, and reflectance may have shown more of a correlation to predictive algorithms than reflectance itself.

4.1 Lab Results

Chl-*a* ranges for all sites were low, ranging from 0.987 μg/L at ALB4 to 7.217 μg/L at ALC10 (Table 3.4, Figure 3.1a). None of these sites typically have high Chl-*a* content (Schalles, 2006). Hladik (2004) reported that Chl-*a* ranged from 0.51 μg/L to 29.65 μg/L and averaged 9.71 μg/L at Duplin River and Altamaha River stations in August. In January, Hladik (2004) found that Chl-*a* ranged from 0.15 to 8 μg/L and averaged 2.68 μg/L at Duplin River and Altamaha River stations. These January results are mostly consistent with my Chl-*a* measurements for these study sites (Table 3.5). In this study, Chl-*a* had a mean of 2.257 μg/L (SD= ±1.249 μg/L) at Altamaha River stations, and a mean of 3.162 μg/L (SD= ±1.605 μg/L) at Duplin River stations (Table 3.5). Chl-*a* content of St. Marys River stations was significantly higher than at Altamaha River stations. Hladik (2004), noted an increase in both TSS and Chl-*a* in the lower region of the St. Marys River, where St. Marys River stations were concentrated within this study. St. Marys is not usually characterized by Chl-*a* values greater than the Altamaha River (Schalles 2006), however this is most likely a function of seasonality, as St. Marys River was sampled in April, while Altamaha River stations were collected in January and April (Table 3.1).

TSS measurements showed a much greater variation in concentration within stations and sites compared to Chl-*a* and CDOM (Figure 3.1b), ranging from 0.405 mg/L at ALC8 to 68.396 mg/L at ALA3 (Table 3.4). The greatest TSS concentrations were measured at Duplin River

stations (mean=40.555 mg/L, SD= ±23.71 mg/L, Table 3.5). Discharge from the Altamaha leading up to sampling TRA was low the day prior to sampling, and the low 30 days leading up to sampling, and sampling was conducted on a substantial falling time (Table 3.1). It is important to note that TRA stations were sampled on a spring tide, where tidal influence was greatest. Discharge the day prior to sampling TRB was also lower, however in the 30 days leading up to sampling, significant discharge occurred (Table 3.1). Significant discharge from the Altamaha River is known to influence the Duplin River and could explain the TSS values observed in TRB (Cai and Wang, 1998). Tidal output may explain high TSS values recorded in TRA stations, while high discharge the 30 days prior to sampling may account for the high concentrations of TSS recorded at TRB stations. St. Marys River stations sampled in April on a falling tide also had a moderate TSS concentration (mean=31.166 mg/L, SD= ±8.335 mg/L, Table 3.5). This TSS concentration falls within the range sampled by Hladik (2004) in the St. Marys River for January of 2.52-79.10 mg/L, and the range for August of 3.48-39.49 mg/L. The lowest TSS concentration was recorded at Altamaha River stations (mean=13.239 mg/L, SD= ±15.04 mg/L, Table 3.5), sampled in January and April. TSS in the Altamaha River stations was significantly lower than the Duplin and St. Marys Rivers stations (Table 3.5, Figure 3.1b). In Hladik (2004), average TSS measurements for the combined Altamaha River and Duplin River stations was 22.28 mg/L in August, and 18.12 mg/L in January, both lower than the combined average of the Altamaha and Duplin Rivers TSS concentrations measured in this study (mean=35.8605 mg/L). When looking at the Altamaha River, Hladik (2004) found that TSS content from stations sampled in January ranged from 6.2 mg/L to 9.05 mg/L, but stations in August from the Hladik (2004) study ranged from 6.04 mg/L to 14.96 mg/L. The same seasonal trend was also present within Duplin River

stations, with January's TSS content ranging from 5.6 mg/L to 10.42 mg/L, and August's TSS content ranging from 34.18 mg/L to 38.48 mg/L (Hladik, 2004).

Even though the Altamaha River is known to contribute a large amount of sediment discharge to the Atlantic Ocean (Cai and Wang, 1998), seasonality plays a large role in TSS concentration within both the Altamaha River and Duplin River sites, as periods of high discharge from the Altamaha River are known to influence the both the Altamaha River and Duplin River sites in terms of freshwater output into the Atlantic Ocean, as well as TSS and nutrient content (Hladik, 2004; Takagi et al., 2017). During sampling of the Altamaha River and Duplin River, discharge was at times substantial (Table 3.1). Discharge from the Altamaha River averages around 400 m^3 sec^{-1}, with maximal discharge in spring, and minimum discharge in late summer and fall (Weston et al., 2009). Discharge the day prior to sampling exceeded this average the day before in all Altamaha River sampling days (Table 3.2). Another factor to consider in these lab results is TSS and Chl-*a* amounts were only tested once for each station and may not have been representative or correctly quantified during lab testing. ALC6 recorded 0.0 mg/L of TSS and was excluded from results (Table 3.4), as sediment evident on the filter paper. The initial recorded weight of this filter paper and others may have been improperly recorded, giving some evidence that at times TSS was underestimating (or overestimating). Conducting multiple tests for each of these OACs and deriving a mean from multiple tests would have resulted in a more accurate measure of their values.

The absorption of CDOM observed at all three sites was relatively low when compared to measurements acquired by Hladik (2004) and Schalles (2006), and little variability was found between the CDOM of the sites (Tables 6, Figure 3.1c). For the St. Marys River stations where CDOM absorption was expected to be substantial, we measured an average aCDOM at 440 nm

of 0.218 m^{-1}, comparable to both the Altamaha and Duplin stations (Table 3.5, Figure 3.1c). The lower CDOM values may be a result of stations being located within the Cumberland Sound, and near the river mouth (Figure 2.2d), allowing for tidal mixing, and less influence from CDOM-rich Okefenokee Swamp output. It is highly likely greater CDOM absorption and the resulting influence on the reflectance curve would have been greater within stations located further upstream for all stations. There was a general trend that CDOM was greatest at up-river stations (Figure 2.2b-d, Table 3.4). This CDOM absorption trend is best observed in the ALB stations, with ALB1, a station at the mouth of the Altamaha River (Figure 2.2c), recording a CDOM absorption of 0.085 m^{-1} at 440 nm, while the furthest station upstream, ALB8, recorded a CDOM absorption of 0.369 m^{-1} at 440 nm. Hladik (2004) and Schalles (2006) both made note of this trend within their research, supporting the notion that aCDOM may have been observed upriver.

4.2 Intersite OAC Relationships: Pearson Product-moment Correlation Matrix

The Pearson product-moment correlation matrix (Table 3.6) provides insight into the relationship between the OACs for the sites within the study. It is important to note that the correlation analysis was not controlled for seasonal variation and instead utilizes all the bulk water samples sampled across all the sites. TSS and Chl-*a* were positively correlated (r=0.377, p=0.016) (Table 3.6), which is most likely connected to the fact that phytoplankton are a part of TSS content, and to a lesser extent, the transportation of nutrients is also linked to TSS (Dekker and Peters, 1993; He et al., 2017**)**. Secchi and Chl-*a* were also positively correlated (r=0.449, p=0.004) (Table 3.6), which is contrary to existing literature for eutrophic lakes (Budd et al., 2001). Budd et al. (2001), determined that as a measure of clarity, Secchi indicates a decrease in Chl-*a*. A possible explanation for the inverse relationship here is that due to Chl-*a* concentration in this study being so low (Table 3.4), and the positive relationship between Secchi and Chl-*a* is

more a function of other environmental factors, to explain this is other words, Secchi is more influenced by other constituents within the water than the presence of phytoplankton. CDOM and TSS were strongly negatively correlated (r=-0.706, p=<0.001). This relationship is not seen in Schalles and Hladik (2012) and could be a function of external environmental factors. One potential alternative explanation is salinity, which is known to be negatively correlated with CDOM. High TSS concentrations in the Duplin River paired with lower CDOM measurements because of salinity may have a strong enough effect on these two OACs to create a negative correlation. It is also important to mention that within this study, there was limited variability within CDOM (overall mean=0.207, SD= ±0.018), and high variability within TSS (overall mean=21.605 mg/L, SD= ±19.14) (Table 3.5). More stations with variability in CDOM may have influenced this correlation. It is interesting to note that Secchi and TSS were not negatively related (p=0.25) (Table 3.6), as TSS is usually assumed to be correlated to turbidity. This relationship is evident in Schalles (1998), and while not as significant, still present in Schalles and Hladik (2012), where variables in estuaries along the US coast were tested through the same approach. One potential explanation for a lack of relationship here could be errors in the lab testing underestimating TSS. This explanation is explored more in the limitations section (section 4.6)

With a larger sample size, seasonality could be controlled for, and the correlation between constituents could be explored under different environmental conditions. More stations would have also allowed for an intrasite comparison of OACs. It would also have been interesting to explore the potential relationship between other variables, such as flow, salinity, temperature, or even precipitation.

4.3 Hierarchical Clusters

Hierarchical clustering was completed using the bulk water sample lab results (Figure 3.1), close-range hyperspectral reflectance between 400-750 nm (Figure 3.4a), and Resampled close-range reflectance to align with wavelengths used by the MSI on board Sentinel-2 satellite systems (Figure 3.4b). It is important to recognize that sites were not evenly sampled, with more stations present in the Altamaha River site than in the Duplin River and St. Marys River combined (Table 3.1). This sampling bias may explain the dominance of Altamaha River stations in the clustering analyses.

4.3.1 Lab Clusters

Results from the lab clusters showed some interesting trends, and each cluster can be summarized by the lab statistics effectively. Lab cluster 1 contains most of the non-Altamaha River stations and is characterized by high TSS and high Chl-*a,* but also has high OAC variability (Table 3.7, Figure 3.3a-c). Lab cluster 2 contains mostly Altamaha River stations and is characterized by low TSS and high aCDOM (Table 3.7, Figure 3.3b-c). Lab cluster 3 also contained predominantly Altamaha River stations and was characterized by low OACs (Table 3.7, Figure 3.3a-c). No one site composed most of the stations present in this cluster (Table 3.7, Figure 3.3a-c). This variability suggests that it can be difficult to assume that water quality within a given system is consistent, and that other variables and environmental conditions need to be considered.

Spyrakos et al. (2017), provides the most comprehensive classification of optical water type for inland and coastal waters, with 4,045 hyperspectral water reflectance curves. A k-mean approach was deployed, and spectra scaling was another key difference between Spyrakos et al.

(2017) and the clustering completed in this study. This spectra scaling was in response to variation attributed to amplitude (Schalles, 2006), which was a visible limitation in the clusters of this study. Spyrakos et al. (2017) was able to separate spectra into 13 unique optical water types (cluster) and define all the characteristics of each cluster. A larger sample size and scaling spectra for amplitude would allow for greater performance in hyperspectral clustering. A k-means approach could also be implemented.

4.3.2 Hyperspectral Close-range Reflectance Clusters

The hyperspectral close-range reflectance clusters did not separate the sites well based on OACs. In the statistical analysis of the hyperspectral clusters, only absorption of CDOM at 440 nm was significantly separable between any of the clusters, specifically between hyperspectral cluster 1 and hyperspectral cluster 2 (p=0.012, z=2.851). Hyperspectral close-range reflectance did not correlate well with OACs and there are a couple suggestions to be made in response. First, more sampling might have captured a greater diversity in optical water types, allowing for stations to be more readily separated in response to hyperspectral reflectance. Lab error may be an explanation for some of the homogenous nature of the clusters. Another approach would be to implement band indices to classify stations by optical water type instead of hyperspectral close-range reflectance This would allow for a relationship between the distance between the reflectance peaks and troughs to explain the OACs rather than the reflectance of the curve itself.

4.3.3 Resampled Close-range Reflectance Clusters

Like close-range reflectance clusters, the resampled close-range reflectance clusters separated sites poorly based on OACs. No OAC was separable based on reflectance resampled clusters using the Kruskal-Wallis H test (Figure 3.5a-c). When looking at the group reflectance

spectra based on the resampled close-range reflectance clusters (Figure 3.8a-c), curves are categorized by a function of overall magnitude, which supports the suggestion of implementing band indices to use the relationship of spectral features to explain OACs rather than the entire spectral curve.

4.4 Atmospheric Correction Performance

The second major objective of this project was to quantify atmospheric correction product performance. To accomplish this, a band-to-band regression analysis between resampled close-range reflectance, to L1C, Sen2Cor, and ACOLITE imagery was performed for bands 2 through 6 of Sentinel-2 MSI (Table 1.1, Table 3.9). The majority of the resampled close-range reflectance bands followed the overall shape of the satellite reflectance bands (figure 3.7). Atmospherically uncorrected data (L1C) was negatively correlated with resampled close-range reflectance in all bands (Table 3.9). The L1C bands have significantly higher RMSD and MAPD values than the RMSD and MAPD values of the Sen2Cor and ACOLITE processed images (Table 3.9). All the L1C bands also have a negative slope indicating that as resampled close-range reflectance increased, satellite reflectance decreased (Table 3.9). There is a large intercept value for all the bands, meaning that even if close-range reflectance was zero, the uncorrected satellite imagery would still have a significant reflectance value across each band (Table 3.9). Together, this shows the need for atmospheric correction in the remote sensing of water, with a more significant need in shorter wavelengths where the intercept was higher, and the slope was more intense. This is supported by the concept that top-of-atmosphere signals in shorter wavelengths are more susceptible to atmospheric effects at the sensor level (Frouin et al., 2019; Lillesand et al., 2015).

A comparison of Sen2Cor and ACOLITE can be made (Table 3.9). Sen2Cor Bands 3, 4, and 5 were weakly correlated with *in situ* resampled reflectance, while ACOLITE performed slightly better than Sen2Cor in these bands and had a significant correlation in band 2 (Table 3.9). ACOLITE had lower RMSD and MAPD, showing that resampled reflectance values on average were closer to ACOLITE corrected reflectance than Sen2Cor corrected reflectance. The slope for ACOLITE was closer to one in every band, which demonstrates that an increase in resampled reflectance had a proportional increase in ACOLITE reflectance. Intercept values for ACOLITE were also closer to zero, meaning the predicted reflectance of ACOLITE when *in situ* reflectance is zero was closer than the reflectance predicted by Sen2Cor.

Martins et al. (2017) performed a similar statistical analysis between Sen2Cor and ACOLITE, finding that the two atmospheric correction models performed similarly in dark lakes, and Sen2Cor performed fractionally better over brighter lakes with a higher reflectance value. It is important to note that the ACOLITE-SWIR approach used in this study has since been made obsolete by the dark spectrum fitting approach, which is more robust in calculating aerosol depth (Vanhellemont and Ruddick, 2018). *In situ* measurements were taken from above water, and RMSE values were far smaller than RMSD values in this study, not exceeding 0.025.

Mograne et al. (2019) performed an evaluation of five atmospheric correction algorithms for Sentinel-3 in optically complex waters in France. This comparison did not include Sen2Cor or ACOLITE as Sentinel-3 contains more bands and spectral information than Sentinel-2 and uses different algorithms for atmospheric correction. Bias, relative error, and RMSE were used to determine atmospheric correction performance along with slope and intercept of the regression line. Beyond the study here, Mograne et al. (2019), were able to incorporate a robust spectral analysis, including a spectral angle mean equation to calculate angular differences between

hyperspectral close-range above water reflectance, and incorporated a scoring system for each statistical variable to then be incorporated into one comprehensive scoring equation. RMSE for this study did not exceed 0.02 (Mograne et al., 2019).

Kuhn et al. (2019) provide another approach to atmospheric correction validation that could be used in future work from this study with the use of RMSD and median absolute percent difference. In this study, atmospheric correction performance was a function of OACs, specifically Chl-*a* and turbidity sensitivity to a given model. This study also combined Landsat-8 and Sentinel-2 imagery to increase revisit time and sampling days possible, and above-water close-range hyperspectral reflectance was utilized.

In comparison to this study, all these studies successfully integrated close-range reflectance to satellite reflectance with less deviation. This may be a function of utilizing below-water reflectance instead of above-water reflectance. Lehmann et al. (2023) provide a comprehensive overview of 17 different approaches to collecting close-range hyperspectral reflectance. Included in this literature review is the approach utilized in this study of below-water reflectance from a pole connected to a spectrometer. It is worth mentioning that below water-reflectance and above-water reflectance are not the same, and below-water reflectance should undergo conversion to water-leaving reflectance for an accurate match-up (Lehmann et al., 2023). This conversion is explained in Chipman et al. (2009) and includes accounting for the water-to-air transmittance, the refractive index of water to air, and spectral immersion. This was not completed within this study, which may explain some of the differences between atmospherically corrected satellite imagery, and the resampled close-range reflectance (figure 3.7). Future analysis should include the use of this calculation.

4.5 Limitations

There are several limitations within the workflow of this project (Figure 1), most of which are related to field sampling. Field sampling days must not only coincide with the 5-day revisit time of the Sentinel-2 A/B satellites, but there is also a specific flyover time in which water samples and close-range reflectance must be collected (±3-hour) to minimize dispersion (Bailey and Werdell, 2006). Next, field sampling can only be conducted on days that are free or limited in the amount of cloud cover, which can be unpredictable in coastal systems. Further, a crew of at least 3 is needed for stations to be completed within approximately 15 minutes time, which limits the number of stations that can be sampled within the satellite flyover window. Accounting for all these field sampling logistics was challenging, and an additional day of sampling on the St. Marys River was canceled. This left us with only stations through the Cumberland Sound and towards the St. Marys River mouth at this site meant stations further upstream St. Marys were not collected that potentially would have shown higher CDOM absorption like those found in Schalles (2006) and Hladik (2004). For a more complete analysis of the southeastern US, more stations would need to be collected.

There are a lot of variable conditions at play. More samples would also allow for the collection of stations on similar tidal flow and recent discharge rates for each site. This would have yielded more insights into tidal effects and discharge on the OACs for each site. With only 6 full days of sampling, *in situ* conditions play a large role in the characterization of sites that were observed.

For both the validation of atmospheric correction performance and station and cluster statistical analysis (objective 1, objective 2) (Figure 1), variability between satellite reflectance

and close-range hyperspectral reflectance was also an issue. In the resampled spectral curves (figure 3.7), the close-range reflectance curves are all lower in reflectance than what was observed by the satellite. This is a common result seen when comparing below-water reflectance to satellite reflectance and is potentially a function of adjacency effects, and also the difficulty with converting below-water reflectance to water-leaving radiance (Lehmann et al., 2023). Future studies should try to best account for this by accurately converting below-water reflectance to above-water reflectance. Spectral information is lost when converting *in situ* close-range reflectance to match a multispectral satellite instrument, which is evident when comparing the resampled spectral curves (figure 3.7), and the close-range reflectance curves for each site (Figure 3.6a-c). The difference between atmospheric correction products on a band-to-band comparison does not consider the shape of the reflectance curve. It is this shape that holds a lot of information about the OACs, and it is this reason band indices are utilized to determine the concentration within the upper water column.

CHAPTER 5

CONCLUSION

The objectives of this project were to first characterize three study sites and individual stations along the Georgia coast based on optical water type and bulk water lab sample analysis. After doing this, the next objective was to perform an analysis of the accuracy of Sen2Cor and ACOLITE atmospheric correction processors by using *in situ* data as a ground truth through statistical analysis.

The first objective was successful, in that bulk water samples were effective at separating stations by optical water type using hierarchical clustering, and more studies could use this approach to generally characterize each station, and further, the performance of a retrieval algorithm by cluster. Despite success using the bulk water samples, close-range hyperspectral reflectance was not effective at defining a station's optical water type, and results were inconclusive. More emphasis should be placed in retrieval algorithms and band ratios to separate stations by cluster.

Based on the results from objective 2, it is difficult to quantitatively say one atmospheric correction product is better than the other. According to the band-to-band comparison between the atmospheric correction processors, the performance of both ACOLITE and Sen2Cor was comparable. RMSD and MAPD results were also rather high. Further exploration into this might help with providing a more definitive result. Future work could also focus on using hyperspectral close-range reflectance, and satellite reflectance to predict OACs, and reflectance may have shown more of a correlation to predictive algorithms than reflectance itself. Through this research, 44 estuarine stations were obtained over six days of field sampling with coinciding

Sentinel-2 imagery within a narrow time window. Very few stations like this have been collected along the Georgia coastline, and further work may provide insights into more advanced remote sensing approaches to monitoring southeastern estuaries on the Georgia coastline.

REFERENCES

American Public Health Association. Standard Methods for the Examination of Water and Wastewater. Washington D.C.: American Public Health Association, 1989.

Anderson, D. M. (2009). Approaches to monitoring, control and management of harmful algal blooms (HABs). Ocean & coastal management, 52(7), 342-347.

Bailey, S. W., & Werdell, P. J. (2006). A multi-sensor approach for the on-orbit validation of ocean color satellite data products. Remote Sensing of Environment, 102(1-2), 12–23. https://doi.org/10.1016/j.rse.2006.01.015

Brezonik, P., Menken, K. D., & Bauer, M. (2005). Landsat-based remote sensing of lake water quality characteristics, including chlorophyll and colored dissolved organic matter (CDOM). Lake and Reservoir Management, 21(4), 373-382.

Brezonik, Patrick L., et al. "Factors affecting the measurement of CDOM by remote sensing of optically complex inland waters." Remote Sensing of Environment 157 (2015): 199-215.

Budd, J.W., Drummer, T.D., Nalepa, T.F., and Fahnenstiel, G.L. (2001). Remote sensing of biotic effects: Zebra mussels (Dreissena polymorpha) influence on water clarity in Saginaw bay, Lake Huron. Limnology and Oceanography. 46(2), 213-223.

Caballero, I., Fernández, R., Escalante, O. M., Mamán, L., & Navarro, G. (2020). New capabilities of Sentinel-2A/B satellites combined with in situ data for monitoring small harmful algal blooms in complex coastal waters. Scientific reports, 10(1), 8743.

Cai, W. J., & Wang, Y. (1998). The chemistry, fluxes, and sources of carbon dioxide in the estuarine waters of the Satilla and Altamaha Rivers, Georgia. Limnology and Oceanography, 43(4), 657-668.

Carle, M. V., Halpin, P. N., & Stow, C. A. (2005). Patterns of watershed urbanization and impacts on water quality. JAWRA Journal of the American Water Resources Association, 41(3), 693-708.

Chawla, I., Karthikeyan, L., & Mishra, A. K. (2020). A review of remote sensing applications for water security: Quantity, quality, and extremes. Journal of Hydrology, 585, 124826.

Chipman, J. W., Olmanson, L. G. & Gitelson, A. A. Remote sensing methods for lake management: a guide for resource managers and decision-makers. (North American Lake Management Society, 2009).

Chislock, M. (2013). Eutrophication: Causes, consequences, and controls in aquatic ecosystems. Nature. https://www.nature.com/scitable/knowledge/library/eutrophication-causes-consequences-and-controls-in-aquatic-102364466/

CRD. (2022). Coastal Georgia Ecosystem Report Card 2021. Georgia DNR Coastal Resources Division. https://coastalgadnr.org/sites/default/files/crd/pdf/220411%20Report%20Card%202021.pdf

CNES. (2015, April 24). *Venus*. Venμs. https://venus.cnes.fr/en/VENUS/index.htm

Dall'Olmo, G., Gitelson, A. A., Rundquist, D. C., Leavitt, B., Barrow, T., & Holz, J. C. (2005). Assessing the potential of SeaWiFS and MODIS for estimating chlorophyll concentration in turbid productive waters using red and near-infrared bands. Remote Sensing of Environment, 96(2), 176-187.

Dick, A., Raynaud, J.-L., Rolland, A., Pelou, S., Coustance, S., Gérard Dedieu, Olivier Hagolle, Jean-Pascal Burochin, Binet, R., & Moreau, A. (2022). VENμS: Mission Characteristics, Final Evaluation of the First Phase and Data Production. Remote Sensing, 14(14), 3281–3281. https://doi.org/10.3390/rs14143281

Dekker, A. G., & Peters, S. W. M. (1993). The use of the Thematic Mapper for the analysis of eutrophic lakes: a case study in the Netherlands. International Journal of Remote Sensing, 14(5), 799–821. https://doi.org/10.1080/01431169308904379

Drusch, M., Del Bello, U., Carlier, S., Colin, O., Fernandez, V., Gascon, F., Hoersch, B., Isola, C., Laberinti, P., Martimort, P., Meygret, A., Spoto, F., Sy, O., Marchese, F., & Bargellini, P. (2012). Sentinel-2: ESA's Optical High-Resolution Mission for GMES Operational Services. Remote Sensing of Environment, 120, 25–36. https://doi.org/10.1016/j.rse.2011.11.026

EPD. (2014). St. Marys Watershed Management Plan. https://epd.georgia.gov/document/document/st-marys-river/download

ESA (2019). Copernicus open access hub. Copernicus.eu. https://scihub.copernicus.eu/

ESAa. "Collection 1 Level-1C." Sentinel Online, sentinel.esa.int/web/sentinel/sentinel-data-access/sentinel-products/sentinel-2-data-products/collection-1-level-1c.

ESAb. “Collection 1 Level-2A - Sentinel Online.” Sentinel Online, sentinel.esa.int/web/sentinel/sentinel-data-access/sentinel-products/sentinel-2-data-products/collection-1-level-2a.

ESAc. SNAP – STEP. ESA. Retrieved November 3, 2023, from http://step.esa.int/main/toolboxes/snap

Frouin, R., Franz, B. A., Amir, Knobelspiesse, K., Ahmad, Z., Cairns, B., Chowdhary, J., Dierssen, H. M., Tan, J., Dubovik, O., Huang, X., Davis, A., Kalashnikova, O. V., Thompson, D. R., Remer, L. A., Boss, E., Coddington, O., Deschamps, P.-Y., Gao, B.-C., & Gross, L. (2019). Atmospheric Correction of Satellite Ocean-Color Imagery During the PACE Era. Frontiers in Earth Science, 7. https://doi.org/10.3389/feart.2019.00145

Gao, B.-C., Montes, M. J., Davis, C. O., & Goetz, A. F. H. (2009). Atmospheric correction algorithms for hyperspectral remote sensing data of land and ocean. Remote Sensing of Environment, 113, S17–S24. https://doi.org/10.1016/j.rse.2007.12.015

Gates, Keith and Katy Smith. Assessment of the St. Marys River Biological Water Quality, Primary Productivity, and Pollutant Load - Phase I Monitoring. Brunswick, GA: GDNR, 2008.

GCE LTER. (2023). Georgia Coastal Ecosystems LTER. Gce-Lter.marsci.uga.edu. https://gce-lter.marsci.uga.edu/public/app/conditions.asp

Georgia DNR. (2021). Total Maximum Daily Load Evaluation for Twenty-Eight Stream Segments in the Altamaha River Basin for Dissolved Oxygen. https://epd.georgia.gov/document/document/epdfinalrevisedaltamahadotmdloctober2021approved/download

Georgia Rules & Regulations. (n.d.). GA - GAC. Rules.sos.ga.gov. Retrieved November 18, 2023, from https://rules.sos.ga.gov/gac/391-2-3

Giardino, C., Brando, V. E., Gege, P., Pinnel, N., Hochberg, E., Knaeps, E., Reusen, I., Doerffer, R., Bresciani, M., Braga, F., Foerster, S., Champollion, N., & Dekker, A. (2018). Imaging Spectrometry of Inland and Coastal Waters: State of the Art, Achievements and Perspectives. Surveys in Geophysics, 40(3), 401–429. https://doi.org/10.1007/s10712-018-9476-0

Gilerson, A.A., Gitelson, A.A., Zhou, J., Gurlin, D., Moses, W., Ioannou, I., Ahmed, S.A., 2010. Algorithms for remote estimation of chlorophyll-a in coastal and inland waters using red and near infrared bands. Opt. Express 18, 24109–24125

Gitelson, A. (1992). The peak near 700 nm on radiance spectra of algae and water: relationships of its magnitude and position with chlorophyll concentration. International Journal of Remote Sensing, 13(17), 3367–3373. https://doi.org/10.1080/01431169208904125

Gitelson, A. A., Dall'Olmo, G., Moses, W., Rundquist, D. C., Barrow, T., Fisher, T. R., Gurlin, D., & Holz, J. (2008). A simple semi-analytical model for remote estimation of chlorophyll-a in turbid waters: Validation. Remote Sensing of Environment, 112(9), 3582–3593. https://doi.org/10.1016/j.rse.2008.04.015

Gitelson, A. A., G. Garbuzov, Szilagyi, F., Mittenzwey, K. H., Arnon Karnieli, & Kaiser, A. M. (1993). Quantitative remote sensing methods for real-time monitoring of inland waters quality. International Journal of Remote Sensing, 14(7), 1269–1295. https://doi.org/10.1080/01431169308953956

Gobler, C.J., Doherty, O.M., Hattenrath-Lehmann, T.K., Griffith, A.W., Kang, Y., and Litaker, W. 2017. Ocean warming since 1982 has expanded the niche of toxic algal blooms in the North Atlantic and North Pacific oceans. PNAS. 114 (19): 4975-4980.

Gons, H. J. (1999). Optical Teledetection of Chlorophyll a in Turbid Inland Waters. Environmental Science and Technology, 33(7), 1127–1132. https://doi.org/10.1021/es9809657

Gordon, H. R. (1978). Removal of atmospheric effects from satellite imagery of the oceans. Applied Optics, 17(10), 1631-1636.

Gurlin, D., Gitelson, A. A., & Moses, W. J. (2011). Remote estimation of chl-a concentration in turbid productive waters — Return to a simple two-band NIR-red model? Remote Sensing of Environment, 115(12), 3479–3490. https://doi.org/10.1016/j.rse.2011.08.011

He, Q., Qiu, Y., Liu, H., Sun, X., Kang, L., Cao, L., Li, H., & Ai, H. (2017). New insights into the impacts of suspended particulate matter on phytoplankton density in a tributary of the Three Gorges Reservoir, China. Scientific Reports, 7(1). https://doi.org/10.1038/s41598-017-13235-0

Heisler, J., Glibert, P. M., Burkholder, J. M., Anderson, D. M., Cochlan, W., Dennison, W. C., Dortch, Q., Gobler, C. J., Heil, C. A., Humphries, E., Lewitus, A., Magnien, R., Marshall, H. G., Sellner, K., Stockwell, D. A., Stoecker, D. K., & Suddleson, M. (2008). Eutrophication and harmful algal blooms: A scientific consensus. Harmful Algae, 8(1), 3–13. https://doi.org/10.1016/j.hal.2008.08.006

Herrmann, I., Pimstein, A., Karnieli, A., Cohen, Y., Alchanatis, V., & Bonfil, J. D. (2010). Utilizing the venus red-edge bands for assessing LAI in crop fields. Core Spatial Databases-Updating, Maintenance and Services-from Theory to Practice.

Hladik, C. M. (2004). Close-Range, Hyperspectral Remote Sensing of Southeastern Estuaries and an Evaluation of Phytoplankton Chlorophyll-a Predictive Algorithms. Creighton University, Omaha, NE, USA.

Hoagland, P., Anderson, D. M., Kaoru, Y., & White, A. W. (2002). The economic effects of harmful algal blooms in the United States: Estimates, assessment issues, and information needs. Estuaries, 25(4), 819–837. https://doi.org/10.1007/bf02804908

IOCCG (2010). Atmospheric correction for remotely-sensed ocean-colour products. In M.Wang (Ed.), Reports of the International Ocean-Colour Coordinating Group, No. 10. Dartmouth, Canada: IOCCG.

IOCCG. Evaluation of Atmospheric Correction Algorithms over Turbid Waters. Dartmouth, NS, Canada, 2019.

Kaufman, Y. J., & Sendra, C. (1988). Algorithm for automatic atmospheric corrections to visible and near-IR satellite imagery. International Journal of Remote Sensing, 9(8), 1357–1381. https://doi.org/10.1080/01431168808954942

Kothari, V., Vij, S., Sharma, S., & Gupta, N. (2021). Correlation of various water quality parameters and water quality index of districts of Uttarakhand. Environmental and Sustainability Indicators, 9(Environmental and Sustainability Indicators), 100093. https://doi.org/10.1016/j.indic.2020.100093

Koutroulis, A.G., Papadimitriou, L.V., Grillakis, M.G., Tsanis, I.K., and Betts, R.A. 2019. Global water availability under high-end climate change: A vulnerability based assessment. Global and Planetary Change. 175: 52-63. https://doi.org/10.1016/j.gloplacha.2019.01.013

Kuhn, C., Aline, Ward, N. S., Loken, L. C., Sawakuchi, H. O., Kampel, M., Richey, J. E., Stadler, P., John Robertson Crawford, Striegl, R. G., Vermote, E., Nima Pahlevan, & Butman, D. (2019). Performance of Landsat-8 and Sentinel-2 surface reflectance products for river remote sensing retrievals of chlorophyll-a and turbidity. Remote Sensing of Environment, 224, 104–118. https://doi.org/10.1016/j.rse.2019.01.023

Kummu, M., de Moel, H., Ward, P. J., & Varis, O. (2011). How Close Do We Live to Water? A Global Analysis of Population Distance to Freshwater Bodies. PLoS ONE, 6(6), e20578. https://doi.org/10.1371/journal.pone.0020578

Kutser, T. (2004). Quantitative detection of chlorophyll in cyanobacterial blooms by satellite remote sensing. Limnology and Oceanography, 49(6), 2179–2189. https://doi.org/10.4319/lo.2004.49.6.2179

Kutser, T., Pierson, D. C., Kallio, K. Y., Reinart, A., & Sobek, S. (2005). Mapping lake CDOM by satellite remote sensing. Remote Sensing of Environment, 94(4), 535–540. https://doi.org/10.1016/j.rse.2004.11.009

Lacaux, J. P., Tourre, Y. M., Vignolles, C., Ndione, J. A., & Lafaye, M. (2007). Classification of ponds from high-spatial resolution remote sensing: Application to Rift Valley Fever epidemics in Senegal. Remote Sensing of Environment, 106(1), 66–74. https://doi.org/10.1016/j.rse.2006.07.012

Lang, S. E., Luis, K. M., Doney, S. C., Cronin-Golomb, O., & Castorani, M. C. (2023). Modeling Coastal Water Clarity Using Landsat-8 and Sentinel-2. Earth and Space Science, 10(7), e2022EA002579.

Lehmann, M. K., Gurlin, D., Pahlevan, N., Alikas, K., Anstee, J., Balasubramanian, S. V., Barbosa, C. C. F., Binding, C., Bracher, A., Bresciani, M., Burtner, A., Cao, Z., Dekker, A. G., Di Vittorio, C., Drayson, N., Errera, R. M., Fernandez, V., Ficek, D., Fichot, C. G., & Gege, P. (2023). GLORIA - A globally representative hyperspectral in situ dataset for optical sensing of water quality. Scientific Data, 10(1), 100. https://doi.org/10.1038/s41597-023-01973-y

Li, R., & Li, J. (2004). Satellite remote sensing technology for lake water clarity monitoring: an overview. Environmental Informatics Archives, 2, 893-901.

Lillesand, T. M., Kiefer, R. W., & Chipman, J. W. (2015). Remote sensing and image interpretation (7th ed.). John Wiley & Sons, Inc.

McKnight, C. J. (2016). A modeling study of horizontal transport and residence time in the Duplin River estuary, Sapelo Island GA (Doctoral dissertation, University of Georgia).

Vassiliki Markogianni, Dimitriou, E., & Tzortziou, M. (2013). Monitoring of chlorophyll-a and turbidity in Evros River (Greece) using Landsat imagery. Proceedings of SPIE. https://doi.org/10.1117/12.2027047

Daniel Andrade Maciel, Nima Pahlevan, Faria, C., de, L., Paulino, R. S., Vitor Souza Martins, Eric, V., & Crawford, C. (2023). Validity of the Landsat surface reflectance archive for aquatic science: Implications for cloud-based analysis. Limnology and Oceanography Letters, 8(6), 850–858. https://doi.org/10.1002/lol2.10344

Martins, V., Barbosa, C., de Carvalho, L., Jorge, D., Lobo, F., & Novo, E. (2017). Assessment of Atmospheric Correction Methods for Sentinel-2 MSI Images Applied to Amazon Floodplain Lakes. Remote Sensing, 9(4), 322. https://doi.org/10.3390/rs9040322

Mishra, A. K., & Coulibaly, P. (2009a). Developments in hydrometric network design: A review. Reviews of Geophysics, 47(2). https://doi.org/10.1029/2007rg000243

Mishra, S., & Mishra, D. R. (2012). Normalized difference chlorophyll index: A novel model for remote estimation of chlorophyll-a concentration in turbid productive waters. Remote Sensing of Environment, 117, 394–406. https://doi.org/10.1016/j.rse.2011.10.016

Mograne, M., Jamet, C., Loisel, H., Vantrepotte, V., Mériaux, X., & Cauvin, A. (2019). Evaluation of Five Atmospheric Correction Algorithms over French Optically-Complex Waters for the Sentinel-3A OLCI Ocean Color Sensor. Remote Sensing, 11(6), 668. https://doi.org/10.3390/rs11060668

Morel, A., & Prieur, L. (1977). Analysis of variations in ocean color. Limnology and oceanography, 22(4), 709-722.

Moses, W. J., Gitelson, A. A., Berdnikov, S., & Povazhnyy, V. (2009). Estimation of chlorophyll-a concentration in case II waters using MODIS and MERIS data—successes and challenges. Environmental Research Letters, 4(4), 045005. https://doi.org/10.1088/1748-9326/4/4/045005

Mouw, C. B., Greb, S., Aurin, D., DiGiacomo, P. M., Lee, Z., Twardowski, M., Binding, C., Hu, C., Ma, R., Moore, T., Moses, W., & Craig, S. E. (2015). Aquatic color radiometry remote sensing of coastal and inland waters: Challenges and recommendations for future satellite missions. Remote Sensing of Environment, 160, 15–30. https://doi.org/10.1016/j.rse.2015.02.001

Nazari-Sharabian, M., Ahmad, S., & Karakouzian, M. (2018). Climate change and eutrophication: a short review. Engineering, Technology and Applied Science Research, 8(6), 3668.

Nechad, B., Ruddick, K. G., & Park, Y. (2010). Calibration and validation of a generic multisensor algorithm for mapping of total suspended matter in turbid waters. Remote Sensing of Environment, 114(4), 854–866. https://doi.org/10.1016/j.rse.2009.11.022

Nielsen, F., & Nielsen, F. (2016). Hierarchical clustering. Introduction to HPC with MPI for Data Science, 195-211.

NOAA. (2018). National Weather Service. Weather.gov. https://www.weather.gov/

NOAA. (2023). Tide Predictions - NOAA Tides & Currents. Www.tidesandcurrents.noaa.gov. https://www.tidesandcurrents.noaa.gov/noaatidepredictions.html?id=8670870

NOAA. (2023). NOAA: Quick Report Tool for Socioeconomic Data. Coast.noaa.gov. https://coast.noaa.gov/quickreport/#/index.html

Osburn, C. L., & Stedmon, C. A. (2011). Linking the chemical and optical properties of dissolved organic matter in the Baltic–North Sea transition zone to differentiate three allochthonous inputs. Marine Chemistry, 126(1-4), 281–294. https://doi.org/10.1016/j.marchem.2011.06.007

Paerl, H. W., & Huisman, J. (2008). Blooms like it hot. Science, 320(5872), 57-58.

Page, B. P., Olmanson, L. G., & Mishra, D. R. (2019). A harmonized image processing workflow using Sentinel-2/MSI and Landsat-8/OLI for mapping water clarity in optically variable lake systems. Remote Sensing of Environment, 231, 111284. https://doi.org/10.1016/j.rse.2019.111284

Pahlevan, N., Sarkar, S., Franz, B. A., Balasubramanian, S. V., & He, J. (2017). Sentinel-2 MultiSpectral Instrument (MSI) data processing for aquatic science applications: Demonstrations and validations. Remote Sensing of Environment, 201, 47–56. https://doi.org/10.1016/j.rse.2017.08.033

Pahlevan, N., Mangin, A., Balasubramanian, S. V., Smith, B., Alikas, K., Arai, K., Barbosa, C., Bélanger, S., Binding, C., Bresciani, M., Giardino, C., Gurlin, D., Fan, Y., Harmel, T., Hunter, P., Ishikaza, J., Kratzer, S., Lehmann, M. K., Ligi, M., & Ma, R. (2021). ACIX-Aqua: A global assessment of atmospheric correction methods for Landsat-8 and Sentinel-2 over lakes, rivers, and coastal waters. Remote Sensing of Environment, 258, 112366. https://doi.org/10.1016/j.rse.2021.112366

Palmer, S. C. J., Kutser, T., & Hunter, P. D. (2015). Remote sensing of inland waters: Challenges, progress and future directions. Remote Sensing of Environment, 157, 1–8. https://doi.org/10.1016/j.rse.2014.09.021

Parlett, C. (2019). Lithium Authentication Redirect. Ews.sas.com. https://community.jmp.com/t5/JMP-Blog/Hierarchical-clustering/ba-p/192425

RBINS. (2023). ACOLITE. ACOLITE. https://odnature.naturalsciences.be/remsem/software-and-data/acolite

Reader, H., Miller, W. (2014) Application of hyperspectral remote sensing reflectance data to photochemical rate calculations in the Duplin River, a tidal river on the coast of Georgia, USA, GIScience & Remote Sensing, 51:2, 199-211, DOI: 10.1080/15481603.2014.895583

Richardson, L. L. (1996). Remote sensing of algal bloom dynamics. BioScience, 46(7), 492-501.

Richter R., Louis J., Müller-Wilm Uwe. (2012) Sentinel-2 MSI – Level 2A Products Algorithm Theoretical Basis Document.

Rodgers, E. M. (2021). Adding climate change to the mix: Responses of aquatic ectotherms to the combined effects of eutrophication and warming. Biology Letters, 17(10), 20210442.

Sagan, V., Peterson, K. T., Maimaitijiang, M., Sidike, P., Sloan, J., Greeling, B. A., Maalouf, S., & Adams, C. (2020). Monitoring inland water quality using remote sensing: potential and limitations of spectral indices, bio-optical simulations, machine learning, and cloud computing. Earth-Science Reviews, 205, 103187.

Sanford, L. P., Boicourt, W. C., & Rives, S. R. (1992). Model for Estimating Tidal Flushing of Small Embayments. Journal of Waterway, Port, Coastal, and Ocean Engineering, 118(6), 635–654. https://doi.org/10.1061/(asce)0733-950x(1992)118:6(635)

Schaefer, S.C., and M. Alber. 2007. Temporal and spatial trends in nitrogen and phosphorus inputs to the watershed of the Altamaha River, Georgia, USA. Biogeochemistry 86: 231–249. https://doi.org/10.1007/s10533-007-9155-6.

Schalles, J. F., Gitelson, A. A., Yacobi, Y. Z., & Kroenke, A. E. (1998). Estimation of chlorophyll a from time series measurements of high spectral resolution reflectance in an eutrophic lake. Journal of Phycology, 34(2), 383–390. https://doi.org/10.1046/j.1529-8817.1998.340383.x

Schalles, John & Rundquist, Donald & Schiebe, F.R.. (2001). The influence of suspended clays on phytoplankton reflectance signatures and the remote estimation of chlorophyll. Verh Internat Verein Limnol. 27. 3619-3625. 10.1080/03680770.1998.11902502.

Schalles, J. F. (2006). Optical remote sensing techniques to estimate phytoplankton chlorophyll a concentrations in coastal waters with varying suspended matter and CDOM concentrations. In Remote sensing of aquatic coastal ecosystem processes (pp. 27-79). Dordrecht: Springer Netherlands.

Schalles, J., Hladik, C., Lynes, A., & Pennings, S. (2013). Landscape Estimates of Habitat Types, Plant Biomass, and Invertebrate Densities in a Georgia Salt Marsh. Oceanography, 26(3), 88–97. https://doi.org/10.5670/oceanog.2013.50

Schaefer, S. C., & Alber, M. (2007). Temporal and spatial trends in nitrogen and phosphorus inputs to the watershed of the Altamaha River, Georgia, USA. Biogeochemistry, 86, 231-249.

Schroeder, T., Behnert, I., Schaale, M., Fischer, J., and Doerffer, R. (2007). Atmospheric correction algorithm for MERIS above Case-2 waters. Int. J. Remote Sens. 28, 1469–1486. doi: 10.1080/01431160600962574

Sheldon, J. E., & Alber, M. (2002). A comparison of residence time calculations using simple compartment models of the Altamaha River Estuary, Georgia. Estuaries, 25, 1304-1317.

Smith, M. E., Lain, L. R., & Bernard, S. (2018). An optimized chlorophyll a switching algorithm for MERIS and OLCI in phytoplankton-dominated waters. Remote Sensing of Environment, 215, 217-227.

Spyrakos, E., O'Donnell, R., Hunter, P. D., Miller, C., Scott, M., Simis, S. G. H., Neil, C., Barbosa, C. C. F., Binding, C. E., Bradt, S., Bresciani, M., Dall'Olmo, G., Giardino, C., Gitelson, A. A., Kutser, T., Li, L., Matsushita, B., Martinez-Vicente, V., Matthews, M. W., & Ogashawara, I. (2017). Optical types of inland and coastal waters. Limnology and Oceanography, 63(2), 846–870. https://doi.org/10.1002/lno.10674

St. Marys River Management Committee., 2003, St. Marys River Management Plan. https://www.sjrwmd.com/waterways/st-marys-river/

Sun, D., Hu, C., Qiu, Z., Cannizzaro, J. P., & Barnes, B. B. (2014). Influence of a red band-based water classification approach on chlorophyll algorithms for optically complex estuaries. Remote Sensing of Environment, 155, 289–302. https://doi.org/10.1016/j.rse.2014.08.035

United Nations. (2023, May 21). UN 2023 SDG Summit. United Nations Sustainable Development. https://www.un.org/sustainabledevelopment/blog/2023/05/un-2023-sdg-summit/

Takagi, K. K., Hunter, K. S., Cai, W. J., & Joye, S. B. (2017). Agents of change and temporal nutrient dynamics in the Altamaha River Watershed. Ecosphere, 8(1), e01519.

United Nations. (2015). Transforming our world : the 2030 Agenda for Sustainable Development. https://www.refworld.org/docid/57b6e3e44.html

USGS. (2021). USGS Surface Water data for USA: USGS Surface-Water Annual Statistics. Waterdata.usgs.gov. https://waterdata.usgs.gov/nwis/annual

USGS. (2023). Landsat 4 | U.S. Geological Survey. www.usgs.gov. https://www.usgs.gov/landsat-missions/landsat-4

USGS. (2023b). Landsat 5 | U.S. Geological Survey. Www.usgs.gov. https://www.usgs.gov/landsat-missions/landsat-5

USGS. (2023c). Landsat 7 | U.S. Geological Survey. www.usgs.gov. https://usgs.gov/landsat-missions/landsat-7

USGS. (2023d). Landsat 8 | U.S. Geological Survey. www.usgs.gov. https://www.usgs.gov/landsat-missions/landsat-8

USGS. (2023e). Landsat 9 | U.S. Geological Survey. www.usgs.gov. https://www.usgs.gov/landsat-missions/landsat-9

USGS. (2023f). Landsat Provisional Aquatic Reflectance | U.S. Geological Survey. www.usgs.gov. https://www.usgs.gov/landsat-missions/landsat-provisional-aquatic-reflectance

USGS. (2023g). USGS Water Data for the Nation. Nwis.waterdata.usgs.gov. https://nwis.waterdata.usgs.gov/nwis

Valdivieso-Ros, C., Alonso-Sarría, F., & Gomariz-Castillo, F. (2021a). Effect of Different Atmospheric Correction Algorithms on Sentinel-2 Imagery Classification Accuracy in a Semiarid Mediterranean Area. Remote Sensing, 13(9), 1770–1770. https://doi.org/10.3390/rs13091770

Vanhellmont, Q., & Ruddick, K. (2016). Acolite for Sentinel-2: Aquatic Applications of MSI Imagery. Living Planet Symposium, 740, 55.

Vanhellemont, Q., & Ruddick, K. (2018). Atmospheric correction of metre-scale optical satellite data for inland and coastal water applications. Remote Sensing of Environment, 216, 586–597. https://doi.org/10.1016/j.rse.2018.07.015

Vanhellemont, Q. (2019). Adaptation of the dark spectrum fitting atmospheric correction for aquatic applications of the Landsat and Sentinel-2 archives. Remote Sensing of Environment, 225, 175–192. https://doi.org/10.1016/j.rse.2019.03.010

Wang, L., Lyons, J., Kanehl, P., & Bannerman, R. (2001). Impacts of urbanization on stream habitat and fish across multiple spatial scales. Environmental management, 28, 255-266.

Warren, M. E., Stefan, Martinez-Vicente, V., Poser, K., Bresciani, M., Alikas, K., Evangelos Spyrakos, Giardino, C., & Ave Ansper. (2019). Assessment of atmospheric correction algorithms for the Sentinel-2A MultiSpectral Imager over coastal and inland waters. Remote Sensing of Environment, 225, 267–289. https://doi.org/10.1016/j.rse.2019.03.018

Weston, N. B., Hollibaugh, J. T., & Joye, S. B. (2009). Population growth away from the coastal zone: Thirty years of land use change and nutrient export in the Altamaha River, GA. Science of the total environment, 407(10), 3347-3356.

Whitehead, P. G., Wilby, R. L., Battarbee, R. W., Kernan, M., & Wade, A. J. (2009). A review of the potential impacts of climate change on surface water quality. Hydrological sciences journal, 54(1), 101-123.

WHO. (2019). 1 in 3 people globally do not have access to safe drinking water – UNICEF, WHO. Www.who.int. http://www.who.int/news/item/18-06-2019-1-in-3-people-globally-do-not-have-access-to-safe-drinking-water-unicef-who

Widory, D., Petelet-Giraud, E., Négrel, P., & Ladouche, B. (2004). Tracking the Sources of Nitrate in Groundwater Using Coupled Nitrogen and Boron Isotopes: A Synthesis. Environmental Science & Technology, 39(2), 539–548. https://doi.org/10.1021/es0493897

YSI. (2023). Continuous, unattended multiparameter water quality instrument | YSI | EXO2 | ysi.com. Www.ysi.com. https://www.ysi.com/exo2